THE EFFECTS OF GRAIN SIZE HETEROGENEITY

ON SEDIMENT TRANSPORT MODELING

By

ROSS STEVEN WICKHAM

A thesis submitted in partial fulfillment of
the requirements for the degree of

MASTER OF SCIENCE IN ENVIRONMENTAL ENGINEERING

WASHINGTON STATE UNIVERSITY
Department of Civil and Environmental Engineering

MAY 2015

To the Faculty of Washington State University:

The members of the Committee appointed to examine the thesis of ROSS STEVEN WICKHAM find it satisfactory and recommend that it be accepted.

____
John Petrie, Ph.D., Chair

____
Jennifer Adam, Ph.D.

____
Yonas Demissie, Ph.D.

ACKNOWLEDGEMENT

The author gratefully acknowledges the financial support provided by the Northwest Advanced Renewables Alliance (NARA) project. Much of the methodology and content was produce in collaboration with John Petrie. Eric Sorensen provided assistance with field work that would have otherwise been impossible to conduct alone.

THE EFFECTS OF GRAIN SIZE HETEROGENEITY

ON SEDIMENT TRANSPORT MODELING

Abstract

by Ross Steven Wickham, M.S.
Washington State University
May 2015

Chair: John Petrie

Sediment is a major pollutant of U.S. waterways, affecting both people and the environment in numerous ways. Increases or decreases in the sediment supply of a waterway may damage infrastructure or degrade habitat quality, so it is important to accurately predict sediment transport. Computational modeling of sediment transport has become increasingly more advanced in recent decades. However, numerical model predictions are only valid if the natural environment is appropriately represented. The heterogeneous surface of gravel bedded streams presents a source of uncertainty in numerical model representation, and is the focus of this thesis. The analyses presented in this study may be divided into three main components: statistical analysis, hydraulic modeling, and disturbance predictions. First, various statistical tests are applied to grain size samples to establish statistically similar groups. A multi-sample, non-parametric statistical test is identified as most appropriate with respect to grain size analysis. Properties of the test established grain size groups that are translated to roughness values with the least amount of redundancy. In the second analysis component, the heterogeneity of both roughness and grain size are analyzed with a hydraulic model capable of simulating sediment transport. Findings show that roughness heterogeneity alone does not produce a difference in sediment transport predictions, but is important when considering flow properties such as velocity. The effects of grain size heterogeneity have significant impacts on bedload transport predictions. Lastly, impacts to sediment yield and bedload transport due to biomass removal following timber harvesting in forested watersheds are assessed. Hillslope predictions show an increase in sediment yield of between 6 to 65%, which would result in a subsequent bedload transport increase of 1 to 6%. Mean bed material diameter is also predicted to decrease by up to 4 mm. Results of the study highlight the importance of appropriate representation of grain size heterogeneity in computational models. Simulations of uniform and heterogeneous surface types showed significant differences in predicted flow and sediment transport properties. The uncertainty associated with sediment transport models will be reduced if the heterogeneity of the stream surface is considered, providing better estimates for flood control, habitat quality, and other purposes.

TABLE OF CONTENTS

LIST OF TABLES

LIST OF FIGURES

Dedication

This thesis is dedicated to my parents for their continuous support and encouragement throughout my life.

CHAPTER 1: INTRODUCTION

In a recent report released by the U.S. Environmental Protection Agency (EPA), 43% of the nationwide sediment monitoring stations were identified as locations where sediment is likely having an adverse effect on human and environmental health (EPA, 2004). Sediment in rivers impacts flood protection, navigation, drinking water quality, and recreation. In the Pacific Northwest, one of the more heavily cited biological consequences of sedimentation is impacts to salmon habitat (Riebe et al., 2014). However, sediment alterations to rivers affect all aquatic organisms by reducing dissolved oxygen and changing the composition of the bed material. Projects concerned with sedimentation require accurate predictions of sediment transport to properly evaluate design alternatives for their potential to improve current sediment problems. In recent decades, computational modeling of sediment transport has become a powerful tool for projects concerned with sediment issues (Wu, 2008). The resistance of the stream surface, and grain size available for sediment transport are important factors controlling sediment transport (Julien, 2010). The research presented in this thesis focuses on the uncertainty in hydraulic model prediction that is associated with roughness and grain size representation. Particularly, the uncertainty associated with spatial heterogeneity of a stream surface. The uncertainty in hydraulic model predictions is evaluated in the context of anthropogenic and environmental concerns. Motivation for this project is due to recent interest in the downstream impacts to streams from residual woody biomass removal after a timber harvest; a component of the Northwest Advanced Renewables Alliance (NARA) project (www.nararenewables.org). Accurate representation of the stream bed surface is required to elucidate and predict any impacts of biomass removal on bed material and sediment transport. Three primary research questions are defined to examine the role of spatial heterogeneity in gravel bedded streams and NARA project impacts:

1. What is the most appropriate statistical test for grain size measurements?
2. Is grain size heterogeneity important for sediment transport modeling purposes?
3. What are the sediment transport impacts from the removing residual woody biomass from a hillslope?

Chapter 3 addresses the first research question by applying statistical tests to grain size distributions, which are treated as cumulative distribution functions. Many previous studies have focused on accurate sampling (Fripp and Diplas, 1993) and mapping (Crowder and Diplas, 1997) of grain size distributions on a stream bed. New technologies are continuously being developed to measure bed material (Graham et al., 2005) and the physical stream surface (Smart et al., 2004; Bertin and Friedrich, 2014). However, if grain size measurements are collected with the intent of developing a hydraulic model, the analysis of the samples should be evaluated and conducted in that context. It is common to assume that the entire surface of a stream bed is spatially uniform, primarily due to a lack of data to accurately characterize the surface (i.e., a uniform Manning's *n* value). This assumption implies that the bed material is homogenous enough that representation by a single roughness value and grain size distribution is sufficient. In heterogeneous gravel beds, a uniform representation may not be appropriate. If there are distinct populations of bed material throughout the surface, the variations in roughness and grain size may produce regions that respond differently with respect to flow and sediment transport. In Chapter 3 Thiessen polygons are used to represent spatial heterogeneity, and the simulated hydraulic performance of the polygon surfaces are compared to a uniform surface.

Chapter 4 further addresses the second research question, and focuses on hydraulic simulation of various surface types. Hydraulic performance is compared between the Thiessen polygon surface type from Chapter 3, a smoothed (kriged) surface, and a uniform surface. The geostatistical approach of kriging has been shown to accurately predict heterogeneity of the natural environment in many scientific fields (Chappel, 2003; Kitanidis, 1996). The extension of Monte Carlo methods to kriging is also explored through the use of multiple realizations of a kriged surface. This technique produces multiple different configurations of the same surface, with the hope that the true surface will accurately be represented. Differences in the kriged-Monte Carlo realizations are examined through hydraulic simulation. Chapter 4 also addresses the sensitivity of the established hydraulic model to computational grid resolution and flow rate.

In Chapter 5, a methodology is demonstrated to predict the impact that removal of residual woody biomass from a hillslope will have on streams. A hillslope model is evaluated to approximate sediment yields in a watershed. The response of streams to changes in sediment supply is evaluated by a hydraulic model, initialized with surfaces developed in Chapters 3 and 4. The sensitivity of the hillslope model to climate and vegetative cover is also explored.

1.1. Chapter Layout

The following are brief descriptions of the chapters contained within this document and their relations to one another:

1.1.1. Chapter 1: Introduction

This chapter.

1.1.2. Chapter 2: Literature Review

Brief overview of key concepts and methods used in the report.

1.1.3. Chapter 3: Statistical Approaches to Mapping Heterogeneous, Gravel Bedded Stream

A statistical analysis of grain size distribution samples and the subsequent surface mapping resulting from those statistical groupings. The developed maps are used to initialize hydraulic models simulating both deformable and non-deformable stream surfaces. This chapter was written as a stand-alone journal submission.

1.1.4. Chapter 4: Sediment Transport Modeling of a Heterogeneous Gravel Bedded Stream

Hydraulic model development and initialization. Sediment transport predictions are made with hydraulic models using the surfaces developed in Chapter 3, in addition to surfaces developed with a geostatistical approach. This chapter was written as a stand-alone journal submission. Some sections are repeated from Chapter 3.

1.1.5. Chapter 5: Hillslope and Stream Impacts of Residual Woody Biomass Removal in a Harvested Watershed

A methodology proposed to predict sediment delivery and transport alterations due to the Northwest Advanced Renewables Alliance (NARA) project. This chapter extends the use of the hydraulic models developed in Chapters 3 and 4 to predictions for bedload transport rate changes from the NARA project.

1.1.6. Chapter 6: Final Discussion and Thesis Summary

The overall results from Chapters 3, 4, and 5 are briefly overviewed. The purpose and implications of each chapter are reviewed and final concluding remarks are made about analyses performed in Chapters 3, 4, and 5.

CHAPTER 2: LITERATURE REVIEW

This chapter provides more detailed descriptions of the methods and concepts used in this thesis. Topics include timber harvest impacts to watersheds, grain size measurement, geostatistics, and hypothesis testing.

2.1. Timber Harvesting Impacts to Watersheds and Streams

Removing trees, constructing roads, and compacting soil with heavy machinery is an obvious disturbance in a watershed. Quantifying the effects these disturbances have on watersheds and streams has shown to be exceeding difficult. The main shortcoming in understanding the linkage between forestry and channel morphology is the lack of data. Study sites are small and very few have been used long-term (Dunne, 2001). Many studies use a paired watershed approach, where one watershed is used for as a control, and the other for treatment. The multitude of site-specific, influential variables limits the application of data from one site to another. A recent study demonstrated that area of influence alone is a very poor predictor of watershed response to timber harvesting (Bathurst and Iroume, 2014). When the combined factors of proportion of water shed logged, antecedent moisture conditions, and time since timber harvest are combined, they are able to predict impacts on individual watersheds reasonably well (Lewis et al., 2001).

There are also many factors that confound results. For example, with reduced transpiration directly after harvesting, groundwater tables rise and there is more water available for overland flow. This can convert intermittent streams to perennial and increases hydrologic connectivity of the basin. An important consideration is whether sediment yield is increased by more discharge and thus more transport capacity, or if sediment supply is actually increased by lumber harvesting, or a combination of the two factors (Gomi et al., 2005). To add additional constraint on previously collected data, timber harvesting techniques have changed over the past decades to decrease environmental impact. Forest road design has improved subsequent to the discovery that up to 90% of sediment may be delivered from roads (Grant and Wolff, 1991). Harvesting methods that do not compact the soil have demonstrated no significant change in storm peak flow (Robinson and Dubeyrant, 2005). A buffer strip, or undisturbed area, surrounding streams 50 meters on either side has become a common practice to reduce sediment delivery to streams. However, buffer strips are not a guarantee that sediment impacts will be prevented (Heede, 1991).

The size of a stream will also determine the important variables. In small headwater streams, mass movement, bank collapse, and wood accumulation dominate channel morphology. The presence of wood becomes less influential as the size of woody debris relative to the channel width decreases (Hassan et al., 2005b). Smaller order streams appear to be more sensitive to timber harvesting (Ryan and Grant, 1991). However, this may also be due to decreased regulation in small watersheds; some small watersheds are completely clearcut, while regulations prevent 100% clearcutting in large watersheds (Lewis et al., 2001).

In small streams, a phenomena known as hysteresis occurs, which relates the timing of sediment transport to the timing of peak discharge. If bed material is quickly mobilized with a flood flow, the peak sediment transport rate will occur prior to the peak discharge (clockwise hysteresis). However, if bed material is armored, peak discharge may be necessary to remove the armoring layer and initialize bedload transport. Then, peak sediment transport rate would occur closer to peak discharge (counter-clockwise hysteresis), (Hassan et al., 2005a).

The rate of recovery in a watershed depends upon the type of disturbance. There is a primary disturbance from the actual event, but an additional disturbance from mass movement along the hillslope (Gomi et al., 2005). It seems very difficult to relate the processes involved with sediment transport to actual sediment yield when there are so many unpredictable and difficult to measure factors. The armoring and entrainment of protuberances in the channel plays a large role in determining the frequency of sediment yields and energy required to mobilize sediment that may be "stuck" behind nearly immovable obstructions. A probabilistic model seems most appropriate, but there is very likely not enough data to characterize the extremely rare events that have the capacity to move many times the average annual sediment yield (Grant and Wolff, 1991).

2.1.1. Anticipated Impacts to Streams from NARA Project

The area of disturbance of the NARA project relative to the initial timber harvest is expected to be very small. Due to economic constraints, collecting biomass too far from a forest road will not be economical. The optimal distance of biomass harvest from forest roads has yet to be determined because Life Cycle Assessment (LCA) of the project has not been completed as of the April, 2015. Speculation has been made that, with current forest management practices, there would be no additional sediment delivery from the NARA project (Bilby, 2014).

2.2. Field Techniques in Grain Size Measurement

There are many factors that influence the statistical analysis of grain size distributions. First, the collection method may introduce bias into the estimate by artificially increasing the number of large or small particles sampled (Bunte and Abt, 2001b). The Wolman walk method has traditionally been used to select particles from a stream bed. However, this method introduces a large amount of selection bias (Bunte and Abt, 2001b). Most studies only consider the diameter measurement of bed material, which requires deriving one length measurement from a three-dimensional bed particle. Bed material has three axes, labelled *a* (short), *b* (intermediate), and *c* (long). For a spherical particle, the *a*, *b*, and *c* axes are equal. Instead of measuring all three axes to characterize bed material, it has become common practice to measure only the *b*-axis, and assume it is sufficient. Additionally, measuring the *b*-axis with a tape measure or ruler is very time-intensive. A device termed a “gravelometer” has been developed to assist in efficient grain size measurement (Figure 1). Particles are inserted into the square sieves, and the particle’s *b*-axis is assumed to correspond to the largest non-passing sieve. However, particle measurement with the gravelometer is actually a combined measure of both the *b* and *c* axis (Figure 2), (Church et al., 1986).

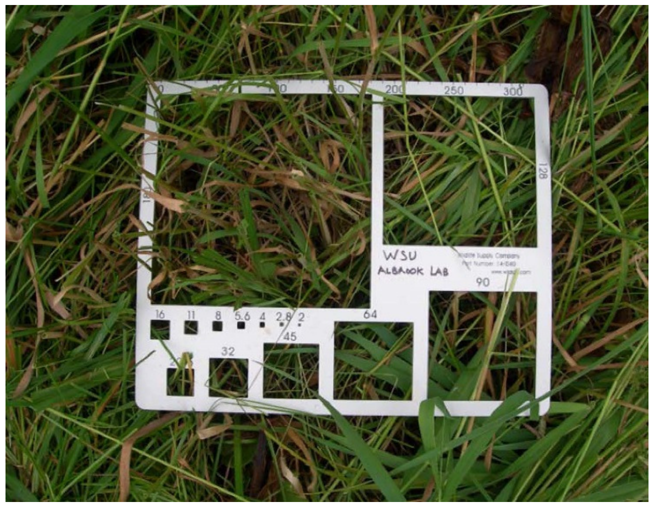

Figure 1. Gravelometer

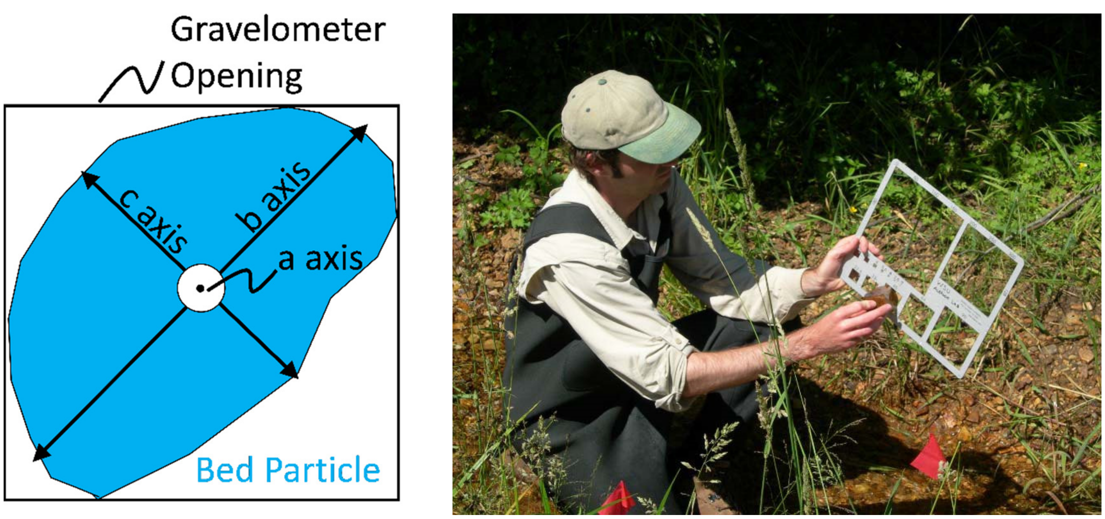

Figure 2. Bed particle axes in relation to gravelometer opening (left), and demonstration of gravelometer use (right)

Issues also arise in selection of bed material from the stream surface. When collecting bed material, users typically tend to prefer larger size materials, which are easier to pick up (Bunte and Abt, 2001b). This biases the grain size distribution towards the coarse bed particles. One solution to selection bias is to use a grid to assist in picking up grains (Bunte and Abt, 2001a).

2.3. Kriging

Kriging is a geostatistical method used to characterize a surface where point measurements are not available. The applications of kriging have been extensive, and include subsurface hydrology, mining, ecology, remote sensing, rainfall, and elevation modeling (Curriero and Lele, 1999). Geostatistics has only recently been applied to fluvial geomorphology (Chappell et al., 2003). The primary advantage of kriging is that it produces an unbiased estimate of a parameter, while also preserving the variance of the estimate. Kriging has been shown to outperform a maximum likelihood approach, and approximate measured values within a 95% confidence interval (Kitanidis, 1996).

2.3.1. Semi-variance

The first step in kriging is to assess the semi-variance of the data set. Semi-variance is the spatial autocorrelation of point values and is calculated as:

$$\boldsymbol{\gamma\left(h_{i,j}\right) = \frac{1}{2}\left[Z(u_i) - Z(u_i)\right]^2} \qquad (2.1)$$

where,

$\gamma\left(h_{i,j}\right)$ = semi-variance between points u_i and u_j

$h_{i,j}$ = Euclidian distance separating points u_i and u_j, also known as lag

$Z(\cdot)$ = observed parameter values at a point

Equation 2.1 is then applied to each possible spatial pairing of points for a data set, excluding pairings of the same location. When semi-variance ($\gamma(h)$) is plotted against lag (h) for all spatial pairings, it is termed a semi-variogram cloud (Figure 3). An empirical semi-variogram is the resulting mean trend of the semi-variogram cloud, where data is binned at certain lag intervals. The selection of a semi-variogram for a data set is shown in Appendix D.

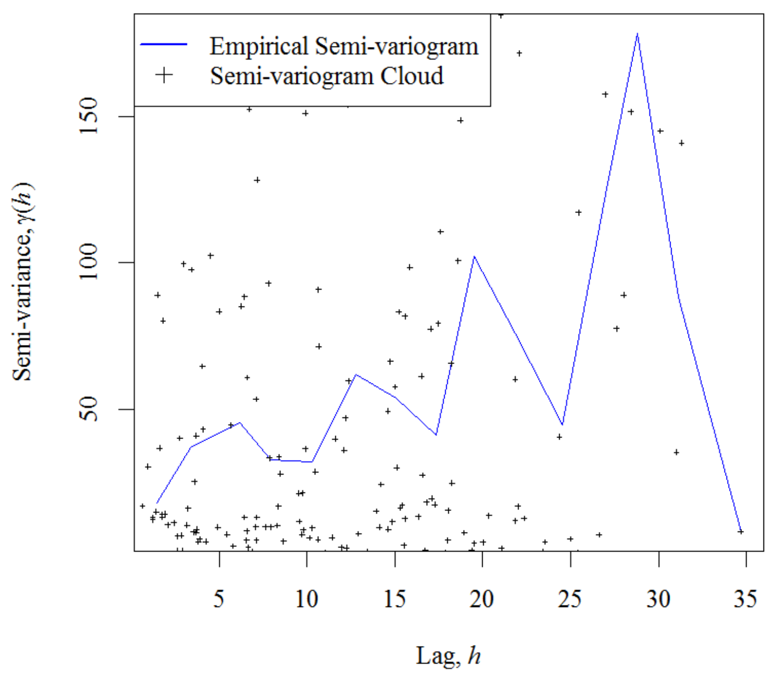

Figure 3. Example semi-variogram cloud and empirical semi-variogram

2.3.2. Anisotropy

Anisotropy is a direction trend in a data set. Accounting for anisotropy when applying the kriging method requires additional analysis. Examples of anisotropic data sets are contaminant concentrations in a groundwater plume, and elevation measurements in a stream channel. In either case, semi-variance in the longitudinal (downstream) direction will be more spatially correlated than the transverse (cross-gradient) direction. One test for anisotropy is to check for a linear trend in the polar data set. Directionality will be observed if there is a statistically significant slope to the polar data set (i.e., the data trends are increasing or decreasing with angle). Anisotropy is examined for a data set in Appendix D.

2.3.3. Predictions using Kriging

The spatial relationship established by semi-variograms is used to make kriging predictions. To predict the mean and variance of a point value, weights are assigned to each known point's value, and the unknown point is calculated using a weighted sum:

$$\boldsymbol{\check{Z}(u)} = \sum_{i=1}^{n} \boldsymbol{W(u_i) Z(u_i)} \tag{2.2}$$

Where,

$\check{Z}(u)$ = mean estimate of unknown point

$W(u_i)$ = weight assigned to observation point u_i

$Z(u_i)$ = observed parameter value for point u_i

n = number of observation points used to estimate the unknown point

The weights, $W(u_i)$, sum to one. In ordinary kriging, which assumes a changing mean across the surface, the weights are determined by a constrained optimization:

$$\boldsymbol{\Phi(W, \lambda)} = \boldsymbol{\sigma_e^2 + 2\lambda(u)\left[1 - \sum_{i=1}^{n} W(u_i)\right]} \tag{2.3}$$

$$\boldsymbol{\frac{1}{2}\frac{\partial \Phi}{\partial \lambda} = 1 - \sum_{i=1}^{n} W(u_i) = 0} \tag{2.4}$$

Where,

σ_e^2 = variance of data set

$\lambda(u)$ = Lagrange parameter

The corresponding weights are solved using the following matrix relationship:

$$\mathbf{KW} = \mathbf{k} \quad (2.5)$$

Where,

K	= covariance matrix for relationships between each point
W	= vector of weights
k	= vector of covariance between observed points and unknown points

From the established semi-variogram, the assumption is made that the covariance of the data set is known. So, Equation 5 becomes:

$$\begin{bmatrix} \gamma(h_{1,1}) & \cdots & \gamma(h_{1,1}) & 1 \\ \vdots & \ddots & \vdots & \vdots \\ \gamma(h_{1,1}) & \cdots & \gamma(h_{1,1}) & 1 \\ 1 & \cdots & 1 & 0 \end{bmatrix} \begin{bmatrix} W_1 \\ \vdots \\ W_n \\ \lambda \end{bmatrix} = \begin{bmatrix} \gamma(h_{1,0}) \\ \vdots \\ \gamma(h_{n,0}) \\ \lambda \end{bmatrix} \quad (2.6)$$

The weights, W_i, are solved by inverting the covariance matrix:

$$\mathbf{W} = \mathbf{K}^{-1}\mathbf{k} \quad (2.7)$$

Equation 2 may then be used to solve for the mean of the predictions and the variance may be solved for as:

$$\sigma_z^2(u) = C(0) - \boldsymbol{Wk} - \lambda \quad (2.8)$$

Where,

$\sigma_z^2(u)$	= variance of prediction at unknown point u
C(0)	= sill of semi-variogram

2.4. Monte Carlo Realizations of Kriged Data

The Monte Carlo methodology randomly samples from a distribution to achieve a representations of multiple possible outcomes. The creation of a realization from a kriged surface is fairly straightforward. From kriging, a mean and standard deviation are predicted for points on a surface. The combination of mean and standard deviation established a normal probability distribution at each point, or a probability surface. Using the Monte Carlo methodology, a realization is generated by randomly sampling from each point on the kriged surface (Figure 4). There are an infinite possible of realizations, all described by the predicted mean and standard deviation values derived from kriging.

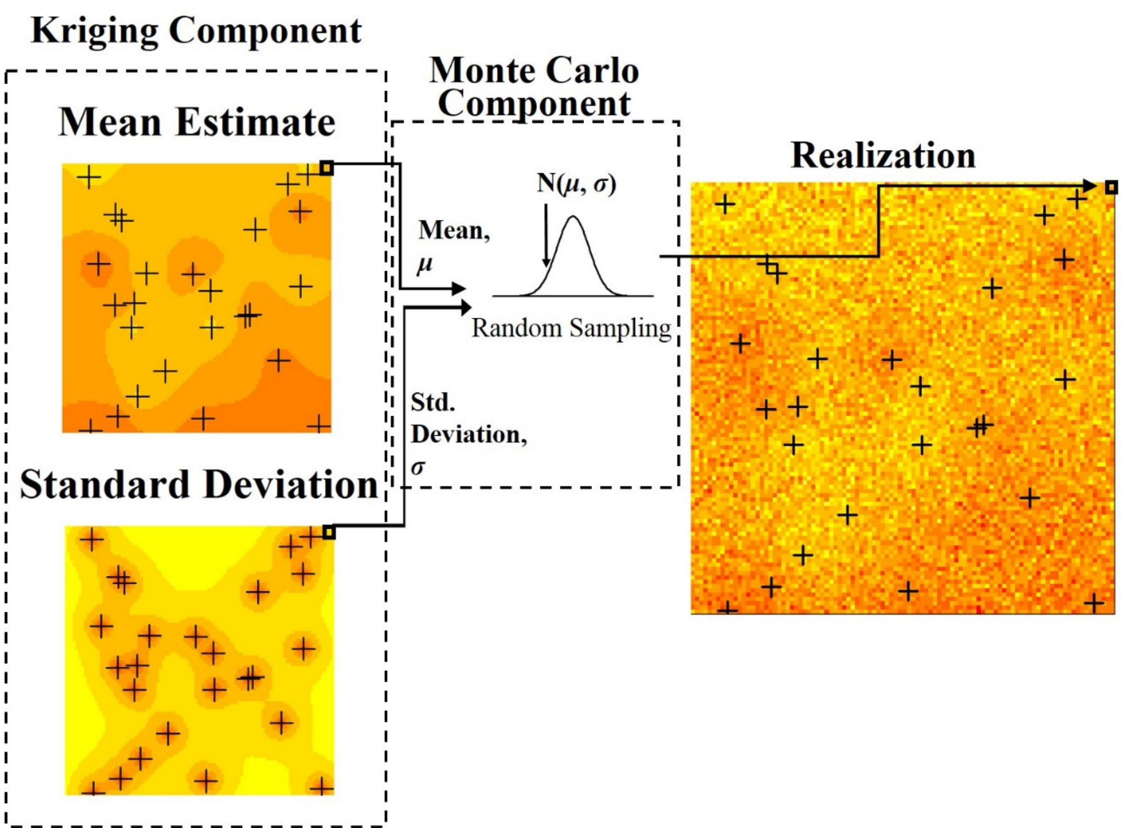

Figure 4. Overview of methodology for generating kriging-Monte Carlo roughness surfaces

2.5. Hypothesis Testing

This section provides some of the rationale for the different tests being used. The selection of statistical tests was based on the premise of comparing as many different types of tests as possible. There are other appropriate tests not used in this study (e.g., Pearson's Chi Square or Cramer von Mises) that were excluded due to their similarity to other tests already being used.

2.5.1. Non-parametric vs. Parametric Tests

Perhaps one of the greatest advantages of the nonparametric test is that there is no need to define a distribution (e.g., normal or gamma). The distributions are relative, and thus do not need to be defined. Parametric tests tend to be more conservative because they use the information provided by the value of each sample point. Non-parametric tests only use the rank of data, which is less informative than the actual value. This may also be a disadvantage of the non-parametric test because outliers are not addressed.

2.5.2. Multi-sample Tests vs. Two-sample Tests

The primary advantage of multi-sample tests is that the probability of Type I error, or familywise error rate, is reduced. A Type I error is a false rejection of the null hypothesis; the samples being compared are similar, but the test indicates they are different. A Type II error is an acceptance of a false null hypothesis; the samples being compared are different, but the test indicates they are the same. When considering the application of the tests to grain size data, with the goal of grouping as many samples as possible, the occurrence of a Type I error is less desirable.

When applying a multi-sample test to a number of samples, a single test is used. When applying two-sample tests to greater than two samples, one test is required for every non-repeating combination of samples. The increased probability of Type I error with the number of tests can be estimated conservatively by:

$$\boldsymbol{P_{Type\ I} = 1 - (1 - \propto)^{n_{test}}} \qquad (2.9)$$

where, $P_{Type\ I}$ is the probability of a Type I error, α is the significance value or acceptable probability of Type I error, n_{test} is number of two-sample tests being used ($n_{test} = \sum_{i=1}^{k-1} i$; k is the number of samples being compared, $k > 2$). The increased probability of Type I error with multiple tests is also known as the familywise error rate. Equation 2.9 is a correction for the familywise error rate applied to the α-value when deriving statistical significance. For example, when comparing five samples using two-sample tests, the calculated p-value must be greater than 0.401 to conclude that the samples are statistically similar (in Equation 9: $k = 5$, $\alpha = 0.05$).

2.5.3. Type I and Type II Error Rates

Because there is a balance between Type I and Type II error, consideration should be made about which error type is more desirable to guide the selection of the significance level (α) and the false negative rate (β). For the purposes of defining distribution groups, the occurrence of a Type I error is less desired, because the intended goal is to group as many similar samples as possible. It is more acceptable for dissimilar samples to be grouped than similar samples be deemed different. Therefore, the conservative correction for Type I error in Equation 2.9 is appropriate.

Acceptable Type I and Type II error rates need to be established prior to performing any test. Similar to the significance level (α), the selection of the false negative rate (β) is arbitrary. Common selections for α and β are 0.05 and 0.80, respectively. However, these values may be changed as needed for a given experiment design. The complements of the α and β terms are the false positive rate ($1 - \alpha$) and the power of the test ($1 - \beta$), respectively.

2.5.4. Distribution Tests

A number of tests were used in this study. To list the procedures of each test would require an exhaustive description. Instead, the hypotheses of all tests is generalized, then the statistic used for each test is provided. A brief discussion of each of the tests is provided to describe the advantages, disadvantages, and basic assumptions.

The hypothesis of all tests being used in this study may be reduced to the following:

Null Hypothesis (H_0): All samples are similar

Alternative Hypothesis (H_A): At least one sample is different

In this study, the term *sample* is used to define a collection of grain size measurements, which also represents a grain size distribution. The following tests were compare samples in this study:

Table 1. Distribution tests

Distribution Test	Number of Samples	Test Type	Test Statistic Type
Kruskal-Wallis	≥2	Non-Parametric	Sample Rank in Combined Data Set
Analysis of Variance (ANOVA)	≥2	Parametric	$\frac{\sum(\text{sample means} - \text{overall mean})}{\sum(\text{sample values} - \text{sample mean})}$
Kolmogorov-Smirnov	2	Non-Parametric	Maximum Difference Between Empirical Cumulative Distribution Functions of Samples (Supremum)
Mann-Whitney	2	Non-Parametric	Sample Rank in Combined Data Set
t-Test	2	Parametric	Difference Between Sample Means

t-test

The *t*-test, or Student's t test, is one of the most common parametric test used to compare two distributions. There are numerous forms of the test, depending upon the assumptions and types of data sets. The least conservative form of the test assumes that both the size and variance of the two samples are unequal, which was the form of the *t*-test used in this analysis. The main disadvantage of the *t*-test is that it assumes the two samples being compared are normally distributed.

Mann-Whitney U Test

The Mann-Whitney test is a non-parametric, two-sample test that uses the rank of data to derive a statistic. The test does not assume a directionality to the differences between the two groups. Therefore, a two-tailed test is used. The two data sets are combined and ranked. In the combined data set, if one of the data sets appears to dominate at a tail of the distribution, then there may be a difference between the two samples (Corder, 2014).

Kolmogorov-Smirnov Test

The Kolmogorov-Smirnov test is one of the most common non-parametric tests applied to compare distributions. The test statistic is the supremum, or greatest difference between the cumulative distributions of two samples. The Kolmogorov-Smirnov test is sensitive to ties, so a modified form of this test was used that was developed specifically for discrete data (Conover, 1972).

Analysis of Variance (ANOVA)

The Analysis of Variance (ANOVA) test is the multi-sample extension of the *t*-test. The ANOVA test partitions the degrees of freedom, sum of squares, and mean square error into treatment and error components (Table 2).

Table 2. ANOVA Table

Source	Degrees of Freedom	Sum of Squares	Mean Square Error
Treatment	$df_{Treatment}$	$SS_{Treatment}$	$MS_{Treatment}$
Error	df_{Error}	SS_{Error}	MS_{Error}
Total	df_{Total}	SS_{Total}	MS_{Total}

As shown in Table 1, a statistic is calculated that accounts for the ratio of between-sample differences in means to the inter-sample difference in means. This ratio is called the *F* statistic, and is used to describe the overall fit of the group. Similar to the *t*-test, the ANOVA test assumes normality of the samples being compared.

Kruskal-Wallis H Test

The Kruskal-Wallis *H* test is an extension of the Mann-Whitney *U* test to more than two samples. The parametric equivalent of the Kruskal-Wallis test is the one-way ANOVA test (Corder and Foreman, 2014). It is important to note that the Kruskal-Wallis test indicates whether or not all distributions in a group are statistically similar. The Kruskal-Wallis test does not indicate which distribution within the combined grouping is different. The first step in the Kruskal-Wallis test procedure is to combine all values from all samples being compared and then rank them. The Kruskal-Wallis *H* statistic is computed by summing the squared rank, and normalizing it by the number of samples in the associated group. Adjustments are also made for the total number of values in the combined sample.

CHAPTER 3: STATISTICAL APPROACHES TO MAPPING HETEROGENEOUS, GRAVEL BEDDED STREAM*

This section describes the methods used to conduct the data collection, statistical analysis, mapping of the stream surface, and initialization of hydraulic models. For the purposes of clarity, the term *sample* in this document is referring to a collection of individual grain size measurements gathered from a single location. Also, *group* refers to a collection of samples deemed to be statistically significant.

3.1. Abstract

Heterogeneous patches of gravel on a stream bed contribute to local differences in flow and sediment transport. The cumulative effect of grain size heterogeneity on sediment transport may result in inaccurate hydraulic model predictions if the surface is not appropriately represented. This study attempts to quantify the effects of grain size heterogeneity by applying a statistical analysis to grain size measurements, spatially discretizing the surface into patches, then conducting hydraulic model simulations. Statistical tests used are the Kruskal-Wallis, ANOVA, Kolmogorov-Smirnov, Mann-Whitney, and t-test. Criterion used to evaluate statistical test performance are 1) number of samples grouped, 2) p-value, and 3) differences in approximated Manning's n roughness values. Results of the statistical analysis indicated that two-sample tests are overly-conservative when grouping samples due to the associated familywise error rate. The Kruskal-Wallis test produced results that are considered most useful for the purposes of hydraulic modeling. The multi-sample, non-parametric properties of the test establish grain size distribution groups that translate to roughness values with the least amount of redundancy. A secondary component of the study was to use the surfaces produced by the statistical tests to initialize two-dimensional hydraulic models under both non-deformable and deformable bed conditions. Hydraulic

simulation of the non-deformable bed showed that the heterogeneous and uniform surfaces produce differences in velocity prediction of up to 0.1 m/s (20%). Roughness heterogeneity is demonstrated to have a biologically significant effect on flow predictions.

3.2. Introduction

The proper representation of a stream's surface is essential for making predictions with hydraulic models. In gravel bedded streams, there are typically spatially distinct populations of bed material established by the geomorphic properties of the stream (Leopold et al., 1964). These heterogeneous patches then create local differences in flow and sediment transport properties of the stream surface (Guerit et al., 2014). The objectives of this chapter are to 1) determine which statistical test is most appropriate for application to grain size measurements, and 2) evaluate the differences in hydraulic model performance of surfaces generated by the statistical tests.

To evaluate the appropriateness of each statistical test, groupings of grain size samples are generated using criteria that evaluate the *p*-value, number of samples in each established group, and approximated Manning's *n* hydraulic roughness values. Spatial discretization of the grain size samples is achieved by performing a Thiessen polygon analysis on the grain size measurement locations. Nays2DH software was used to perform hydraulic simulations of the various surface representations (Shimizu et al., 2015). Differences in hydraulic model performance are compared between Thiessen polygon surfaces and a uniform representation.

3.3. Data Collection

3.3.1. Selected Reach Description

To answer the primary study objectives, data are required to characterize the elevation and bed material of a site's surface. Cat Spur Creek, located in northern Idaho, was selected as the site due to its size, accessible location, and timber harvesting land use history (Figure 5). Bed material at the site consists of poorly sorted gravel, sand, and silt (Figure 5). Definite zones of gravel, sand, and silt were present along the stream that distinguished the main flow carrying portion of the channel (thalweg), (Figure 6).

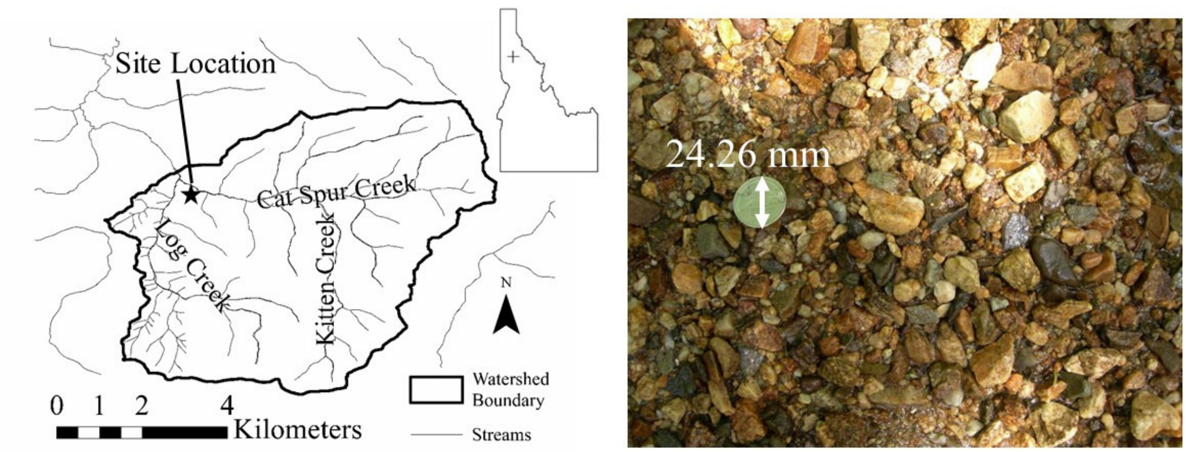

Figure 5. Cat Spur Creek location (left) and photograph of bed material (right)

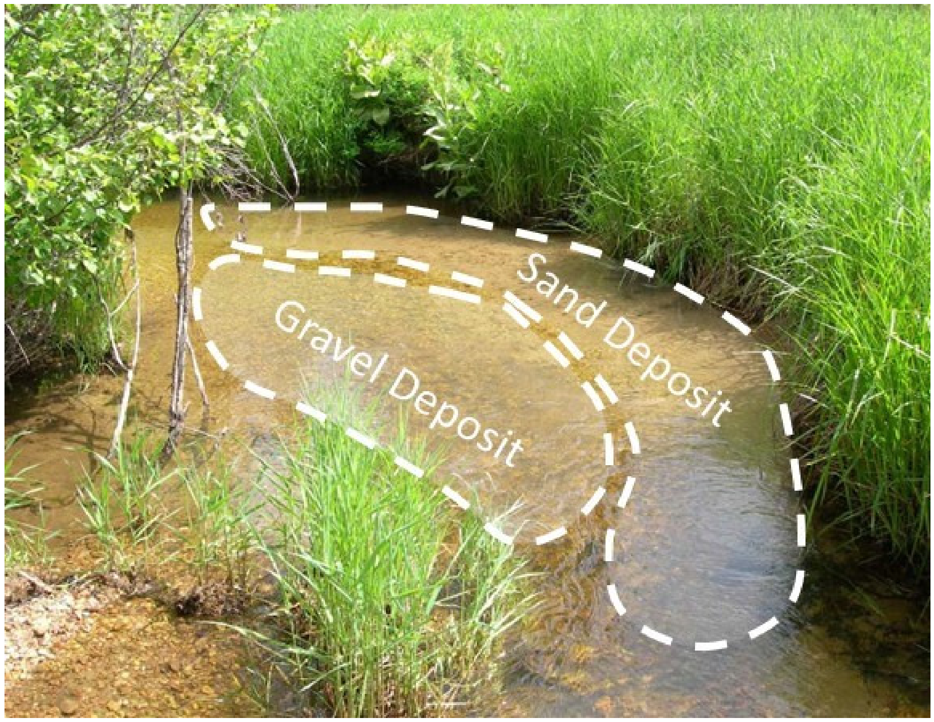

Figure 6. Photograph of sand and gravel deposits along bed at Cat Spur Greek

The selected reach is approximately 40 m in streamwise length and has an average slope of approximately 0.01 (Figure 7). Collapsed banks and in-channel islands are common features along the stream. Reed Canary grass (*Phalaris arundinacea*) at the site has strong roots, and is able to maintain soil stability, even when the bank has been undercut by stream erosion. The Reed Canary grass is a non-native, invasive bunch grass and has altered the morphology of the stream. Site evidence indicated that bank erosion did not occur gradually; instead the banks were undercut to the point of failure and suddenly collapsed (see Appendix E for site photos). Then, the collapsed bank, including the root mass of the Reed Canary grass, would become embedded in the channel. An example of the influence of collapsed banks on the stream cross-section is shown in Figure 8; the collapsed banks are seen in the red line of the right figure (in legend: B. Collapsed Bank) as indentations above the typicaly parabolic shape of the channel cross-section.

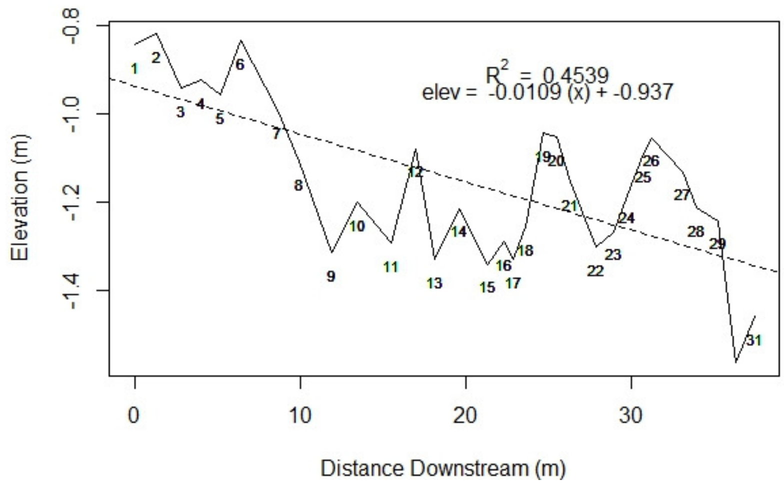

Figure 7. Longitudinal profile of Cat Spur Creek and slope regression, x in regression equation represents downstream distance

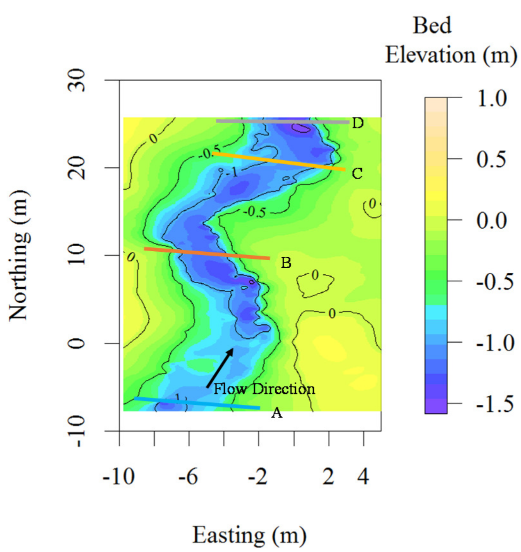

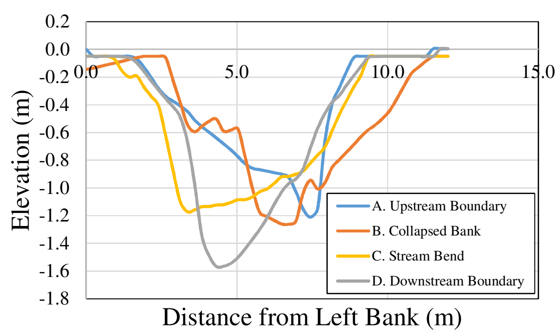

Figure 8. Aerial elevation plot (left) labelled with selected cross-sections (right) of Cat Spur Creek; vertical axis is exaggerated

The trees along the left bank of the reach at Cat Spur Creek were identified as red alders (*Alnus rubra*), (Appendix E). Red alder thickets are short-lived and serve as a cover for seedlings of the next coniferous forest. Red alders pioneer (i.e., are one of the first types vegetation to establish) on landslides, roadsides, and moist locations after disturbances like logging or fire. Thus, it is likely that the bank stability provided by the red alder roots will not persist into the coming decades, altering the morphological properties of Cat Spur Creek as the environment recovers from recent disturbances (Whitney, 1985). The selected reach has debris jams on both the downstream and upstream ends. Sediment had accumulated on the upstream end debris jams, indicating that woody debris is a large influence on stream stability and morphology (see Appendix E for site photos).

3.3.2. Selected Watershed Description

The watershed is approximately 30 km^2, and was most recently logged in 2013. (Figure 10). The land is managed by the Idaho Panhandle National forest. Elevation in the watershed varies from 900 to 1500 meters above mean sea level. Fires occurred in the watershed in 1919 and 1931, burning 7.3 and 8.2 km^2, respectively (USDA FS, 2014). Extensive logging began in 1964 and has continued at a near constant rate to present day (Figure 9). The cumulative area logged between 1964 and 2015 is approximately 20 km^2. The watershed is only 30 km^2, so an equivalent of two thirds the hillslopes have been harvested during the last century. A standard method of harvest has been clearcutting, particularly in the 1990s (Figure 10).

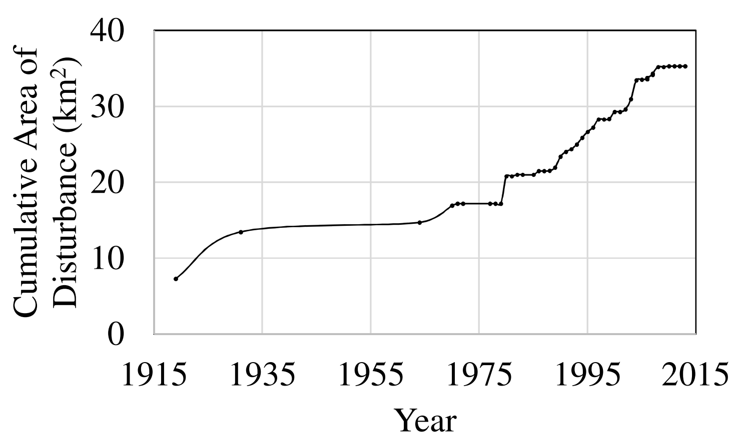

Figure 9. Cumulative area of disturbance for past century in Cat Spur Creek watershed; data includes fires (1919, 1931) and timber harvests (1964-2015), (USDA FS, 2014)

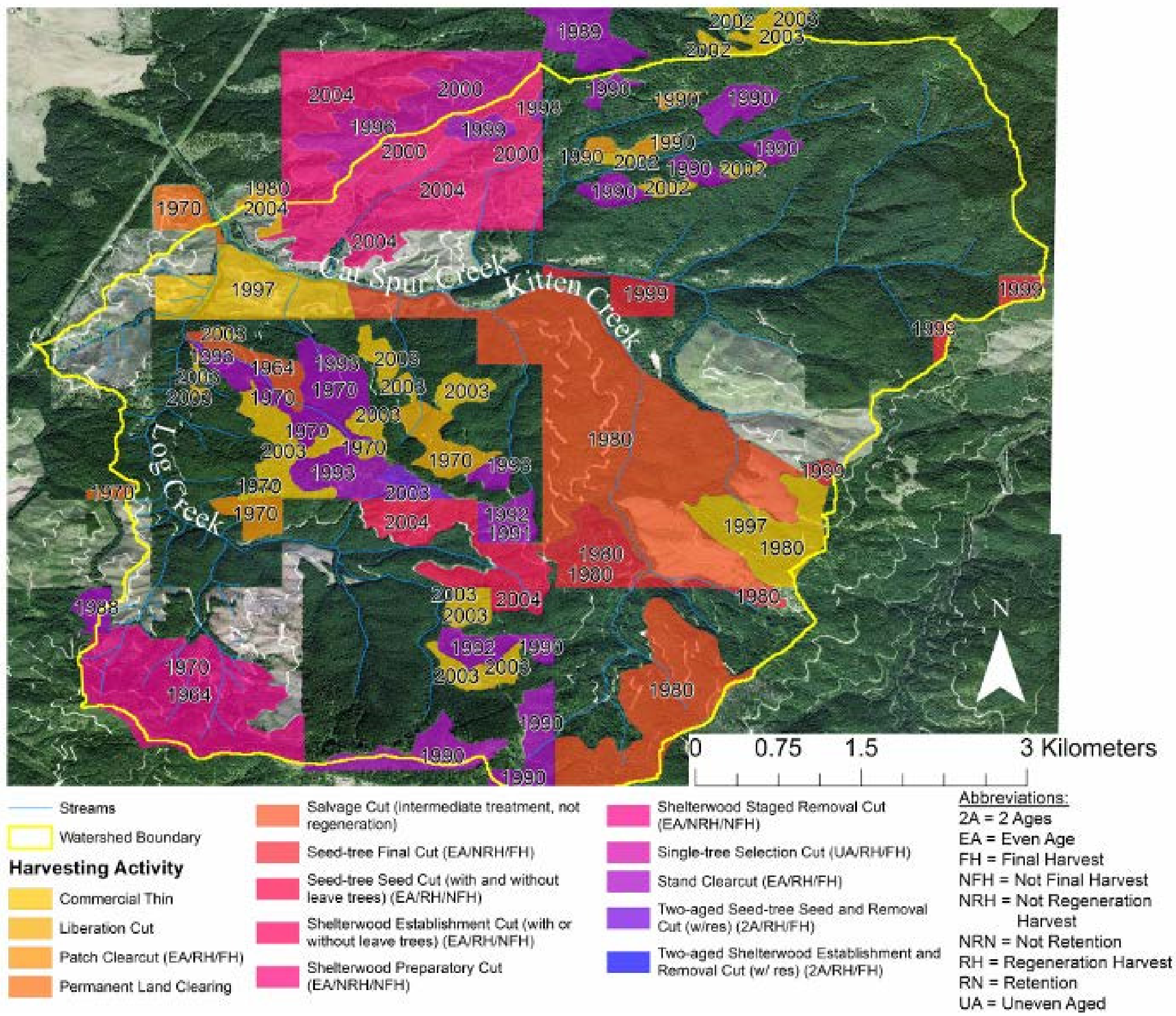

Figure 10. Cat Spur Creek watershed, timber harvesting activities. Number in polygon indicates year of activity. Background aerial photograph taken 2013. Data for most recent logging activity not available, but is visible as cleared areas in background image (USDA FS, 2014)

3.3.3. Elevation Survey

Elevation data were collected on July 16th and 17th, 2014. A total of 35 cross-sections were measured, extending into the floodplain on either side of Cat Spur Creek. The transverse spacing of elevation measurements was approximately 0.25 m, and the longitudinal (downstream) spacing between cross-sections was approximately one meter (Figure 11). Some channel elements such as collapsed banks and small, in-channel islands were surveyed more extensively to properly characterize the surface. Easting, northing, and bed elevation in Figure 11 are relative to an arbitrary site datum, designated as the origin.

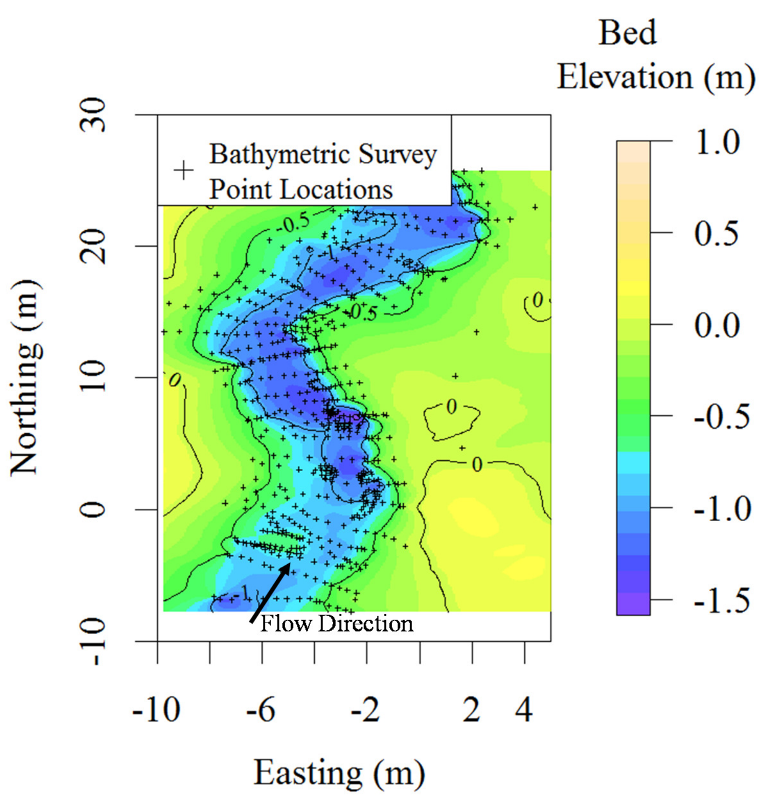

Figure 11. Bathymetric survey point locations, blue colors represent approximate water surface

3.3.4. Bed Material Measurement

A frame was used to assist in the selection of grains to obtain unbiased grain selection and minimize operator error (Bunte and Abt, 2001a), (Figure 12). The size of this frame relative to the stream is small enough that the entire collection of grain size measurements may be treated as a point sample. Measurement of individual grains was made with a gravelometer template to increase efficiency of grain measurement (Figure 12).

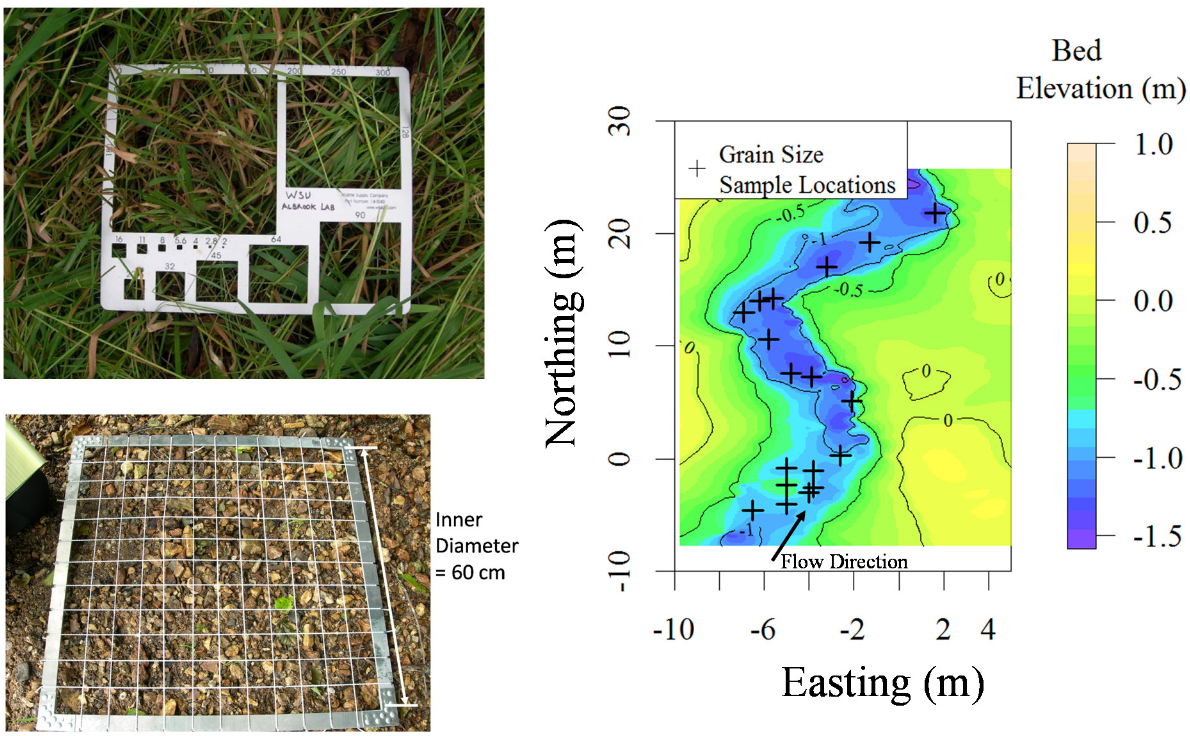

Figure 12. Gravelometer template (top left), gridded sampling frame (bottom left), and site map with labeled grain size sample locations (right). Blue areas of site map approximate water surface elevation.

Sampling occurred on July 22, 2014. A total of 18 separate grain size distributions (samples), each with approximately 120 grains (total of 2,140 grains), were measured by three operators throughout the reach (Figure 12). Bulk samples of sand and silt were also collected, but were excluded from grain size analysis because they were known to represent statistically different material from the remainder of the stream bed. Fine sediments which were not measureable with the smallest sieve size on the gravelometer were recorded as < 2 mm (fines).

The gravelometer does not allow for the measurement of particles less than two mm in diameter along the intermediate axis. Therefore, a category is added to the data to account for particles finer than two mm. The statistical analysis of this lower category is limited to providing only the percentage of particles less than two mm in diameter. Particle in the lowest category have an intermediate axis diameter between zero and two millimeters. The discrete intervals in the gravelometer used in this study are as follows:

Table 3: Gravelometer opening size intervals

Interval	Sieve Size (mm)
1	2
2	2.8
3	4
4	5.6
5	8
6	11
7	16
8	22.6
9	32
10	45
11	64
12	90
13	128
14	180

Fine particles that pass through the 2 mm opening are noted as “fines”. There were some exceptions to the gravelometer interval measurements: some particles were embedded in the surface and could not be removed for measurement. In these instances, the *b*-axes of the particle was measured with a tape measure as best as possible.

Traditional bed particle measurements report the *b*-axis diameter. Particles can be generally described as having a long, intermediate, and short axis. Using a gravelometer, a combination of both the *b* and *c* axes is measured, but the measurement is most influenced by the b axis (Figure 13). Gravelometers are assumed to measure the particle's *b*-axis (Church et al., 1987).

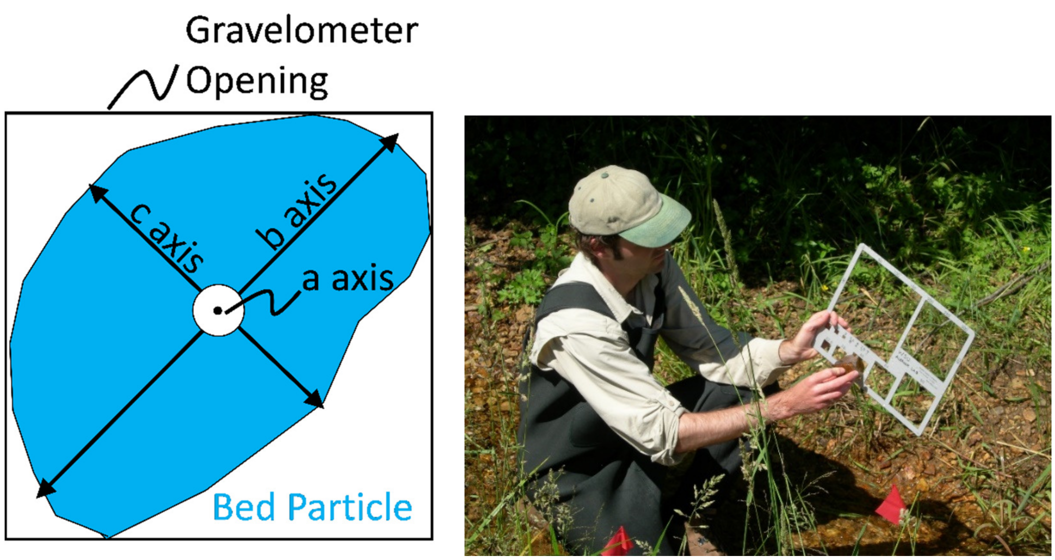

Figure 13: Bed particle in gravelometer opening (left) and demonstration of gravelometer use (right)

3.4. Statistical Tests

The measured grain size distributions (samples) are then tested for similarity to determine which areas of stream surface are comprised of similar bed material. The categories of tests may be simplified by number of sample and test type. Tests capable of comparing more than two samples at once are called multi-sample tests, while two-sample tests can only compare two samples at a time. The Kruskal-Wallis and ANOVA tests are the multi-sample complements of the Mann-Whitney and *t*-test, respectively. The Kruskal-Wallis test is also the non-parametric equivalent of the ANOVA test.

Some important characteristics of the grain size data alter the application of the statistical tests. First, samples were tested using the Kolmogorov-Smirnov test, and all but two samples were statistically similar to lognormal distributions at the α = 0.05 significance level. To satisfy the requirement of normality for the parametric tests, the natural logarithm of the data was taken prior to analysis. Secondly, because a gravelometer template was used, the grain size data is discrete, not continuous. Data are ordered, but confined to the gravelometer sieve sizes, producing many ties. The Kolmogorov-Smirnov test is sensitive to ties, so a modified form of this test was used that was developed specifically for discrete data (Conover, 1972; Gleser, 1985). Lastly, because diameters of the fine particles are unknown, but bounded between zero and two mm. A diameter of one mm was assigned to fine particles; parametric tests were experimentally determined to not be sensitivity to this alteration.

3.4.1. Familywise Error Rate

Multi-sample tests are capable of comparing all candidate samples with one test. When applying two-sample tests, one test is required for every non-repeating combination of samples. The increased probability of a Type I error with the number of tests can be estimated conservatively by:

$$\mathbf{P_{Type\ I} = 1 - (1-\propto)^{n_{test}}} \qquad (3.3)$$

where, $P_{Type\ I}$ is the probability of a Type I error, α is the significance value or acceptable probability of a Type I error, n_{test} is the number of two-sample tests being used ($n_{test} = \sum_{i=1}^{k-1} i$; k is the number of samples being compared, k >2). The increased probability of a Type I error with multiple tests is also known as the familywise error rate. Equation 3.3 is as a familywise error rate correction for the α-value when deriving statistical significance. For example, when comparing five samples using two-sample tests, 10 tests are needed and the calculated *p*-value must be greater than 0.401 to conclude that the samples are statistically similar (in Equation 3.3: k = 5, α = 0.05).

3.4.2. Criterion for Evaluating Groups

Once the statistical analysis of the samples is completed, groups of samples are selected based upon the following criteria:

1. Largest number of samples in group
2. Largest *p*-value; for two-sample tests, the average of all *p*-values associated with the candidate group are used.

Criterion one supersedes the second. These criteria will also be used to compare performance between tests. A procedure was used where every possible combination of samples is examined using every test. A list is created to track each combination, and the associated *p*-values calculated from the statistical tests. Then, the combinations are screened as candidates for a group; first by number of samples in the group, then by *p*-value. For two-sample tests, the minimum *p*-value associated with the group must be greater than the significance value (α) adjusted for the familywise error rate. A third criterion is introduced to evaluate the performance of each test:

3. Difference in Manning's *n* values of groups

If a test produces sample groups that have the same resulting Manning's *n* values, then the groups aren't actually different with respect to flow resistance. Derivation of a Manning's *n* value from a grain size distribution is reviewed in the next section.

3.5. Hydraulic Model Initialization

The hydraulic model used to conduct this analysis is Nays2DH, which was created by the International River Interface Cooperative (iRIC), (Shimizu et al., 2015). Nays2DH is a two dimensional model, capable of predicting sediment transport (aggradation and degradation) of mixed size sediment, and bank erosion. There are three main components required to initialize the physical portion of the Nays2DH hydraulic model: 1) elevation (bathymetry), 2) roughness (Manning's *n*), and 3) grain size regions. Each of these components requires data and processing prior to use in the hydraulic model. Nays2DH allows for point elevation data (x, y, and z) to be imported directly to the software. So, the only processing requirement for elevation data is error checking and formatting.

3.5.1. Roughness Surface Representation

Using the Manning-Strickler equation, a Manning's *n* hydraulic roughness value is calculated for each grain size measurement location. The two spatial configurations for roughness used in this study are uniform and Thiessen polygon. The uniform roughness surface was established by aggregating all grain size measurements, and determining the D_{84} grain size percentile of the composite sample. The Manning-Strickler equation was then used to determine the Manning's *n* value, which was applied to all grid cells within the computational domain.

The Thiessen polygon geometry was determined by grain size measurement locations. Each Thiessen polygon is associated with a grain size sample. Using the results of the statistical tests, samples are assigned to a statistical grouping that has an associated grain size distribution and D_{84} grain size percentile. Similar to the uniform roughness, the Manning-Strickler equation is applied to the D_{84} value, except each polygon is assigned a Manning's *n* value.

3.6. Results

Grain size distributions from each sample, as well as the aggregate of all samples, are shown in Figure 14. Grain size percentiles and the threshold for measurement of fines (2 mm) are also indicated. Table 8 provides the summary of hydraulic model results.

3.6.1. Statistical Tests

The statistical tests provided in were performed on all possible combinations of the Cat Spur Creek grain size samples. A familywise error rate correction was used to account for increased probability of Type I errors from two-sample tests. A summary of the groupings and their associated statistics are shown in Table 6. Mean, standard deviations, and grain size percentiles are shown for each sample (Table 4).

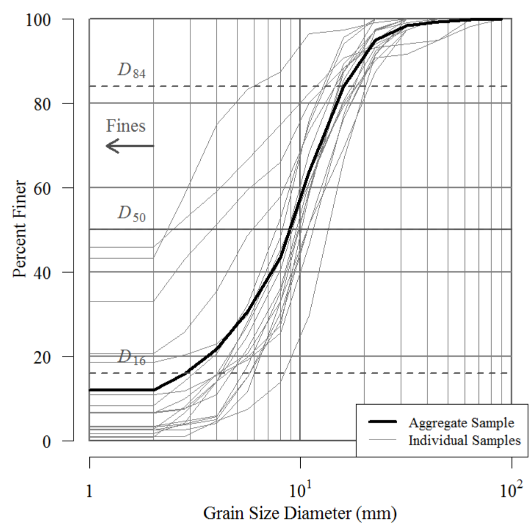

Figure 14. Cat Spur Creek grain size distributions, individual and aggregate (composite) sample

Table 4. Summary of individual sample means, standard deviations, and percentiles. Manning's *n* values calculated using D_{84} values in Manning-Strickler equation

Sample ID	Arithmetic Mean (mm)	Arithmetic Standard Deviation (mm)	Geometric Mean	Geometric Standard Deviation	D_{16} (mm)	D_{50} (mm)	D_{84} (mm)	Manning's n
1	4.2	4.7	2.8	2.4	1	2.8	5.6	0.0792
2	11.3	7.0	9.3	2.0	4	11	16	0.0744
3	13.2	9.4	10.4	2.0	5.6	11	22.6	0.0839
4	9.3	7.6	6.0	2.8	1	8	16	0.0839
5	14.9	13.9	10.9	2.2	5.6	11	22.6	0.0839
6	14.4	7.8	12.2	1.9	8	11	22.6	0.0839
7	13.1	8.9	10.1	2.3	5.6	11	22.6	0.0839
8	13.3	7.8	11.6	1.7	8	11	16	0.0839
9	9.4	5.7	6.7	2.7	1	11	16	0.0839
10	12.5	6.4	10.7	1.9	5.6	11	16	0.0792
11	7.9	8.4	4.3	3.2	1	4	16	0.0792
12	9.3	17.3	3.5	3.7	1	2.8	16	0.0839
13	9.6	5.6	7.6	2.2	4	8	16	0.0839
14	14.5	8.4	12.0	2.0	8	11	22.6	0.0792
15	15.0	10.0	11.2	2.4	4	11	22.6	0.0792
16	16.8	7.1	15.1	1.7	11	16	22.6	0.0839
17	12.2	6.0	10.0	2.1	5.6	11	16	0.0792
18	13.7	7.4	10.5	2.5	4	16	22.6	0.0792
Composite Sample	11.9	9.3	8.4	2.6	4.0	11.0	16.0	0.0792

The grouping of all samples in each test is provided in Table 5. Groupings are color-coded for visual comparison. Blank cells indicate that the sample was determined to not belong to any possible group configuration.

Table 5. Summary statistical test results for each sample. Statistical groupings of samples indicated by color and paired letter.

	Group Tests		Pairwise Tests		
	Kruskal-Wallis	**ANOVA (Lognormal)**	**Kolmogorov-Smirnov (Discrete)**	**Mann-Whitney**	***t*-test (Lognormal)**
Test Type	Non-parametric	Parametric	Non-parametric	Non-parametric	Parametric
Test Statistic Type	Distribution Rank	Mean	Distribution Supremum	Distribution Rank	Mean
Number of Groups	3	1	3	4	4
Largest Number of Samples per Group	10	10	5	6	6
Average *p*-value	0.245	0.154	0.276	0.409	0.343
Sample ID	**Groupings**				
1	C	-	-	D	-
2	-	A	B	C	D
3	A	A	B	A	C
4	B	-	-	C	B
5	A	A	A	A	C
6	A	A	-	D	D
7	A	A	-	C	B
8	A	A	-	D	B
9	B	-	B	C	B
10	A	A	A	B	A
11	-	-	-	B	C
12	C	-	-	A	C
13	B	-	A	A	A
14	A	A	C	B	A
15	A	A	B	A	B
16	-	-	A	A	A
17	A	A	A	B	A
18	A	-	C	B	A

***p*-values**

Group	**Kruskal-Wallis**	**ANOVA (Lognormal)**	**Kolmogorov-Smirnov (Discrete)**	**Mann-Whitney**	***t*-test (Lognormal)**
A	0.174	0.154	0.382	0.647	0.550
B	0.153		0.239	0.553	0.383
C	0.410		0.208	0.266	0.363
D				0.169	0.078

The grain size distributions and their associated groupings for the Kruskal-Wallis test are provided in Figure 15. Similar plots for all other tests are provided in the Appendix B.

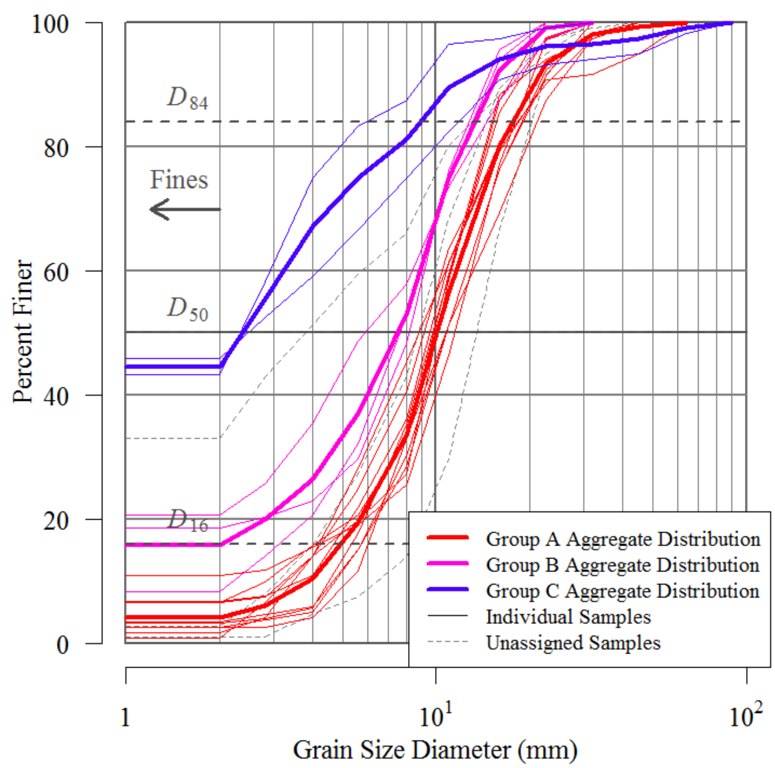

Figure 15. Percent finer plot for grain size distribution groupings derived from the Kruskal-Wallis test

Table 6. Summary of groupings from statistical tests. Manning's n values calculated with Manning-Strickler equation

Test Type	Statistical Test	Group	p-value	Arithmetic Mean (mm)	Arithmetic Standard Deviation (mm)	Geometric Mean	Geometric Standard Deviation	D_{16} (mm)	D_{50} (mm)	D_{84} (mm)	Manning's n
Multi-Sample	Kruskal-Wallis	A	0.174	13.7	8.9	10.9	2.1	5.6	11.0	22.6	0.0839
		B	0.153	9.4	6.4	6.7	2.6	2.0	8.0	16.0	0.0792
		C	0.410	6.8	12.9	3.1	3.1	1.0	2.8	11.0	0.0744
	ANOVA	A	0.154	13.4	8.9	10.8	2.1	5.6	11.0	22.6	0.0839
Two-Sample	Kolmogorov-Smirnov	A	0.382	13.1	8.7	10.5	2.1	5.6	11.0	22.6	0.0839
		B	0.239	12.2	8.5	9.3	2.3	4.0	11.0	22.6	0.0839
		C	0.208	14.1	7.9	11.2	2.2	5.6	16.0	22.6	0.0839
	Mann-Whitney	A	0.647	13.1	11.6	8.9	2.7	4.0	11.0	22.6	0.0839
		B	0.553	12.1	7.7	8.9	2.5	4.0	11.0	22.6	0.0839
		C	0.266	10.8	7.6	7.8	2.5	4.0	11.0	16.0	0.0792
		D	0.169	10.6	8.3	7.3	2.7	2.8	11.0	16.0	0.0792
	t-test	A	0.550	13.1	7.2	10.7	2.1	5.6	11.0	22.6	0.0839
		B	0.383	12.0	8.4	8.8	2.5	4.0	11.0	16.0	0.0792
		C	0.363	11.3	13.0	6.4	3.1	1.0	8.0	16.0	0.0792
		D	0.078	12.9	7.5	10.7	2.0	5.6	11.0	22.6	0.0839
Composite of all Samples				11.9	9.3	8.4	2.6	4.0	11.0	16.0	0.0792

The criterion used to evaluate groups, and the coinciding performance of each tests are listed below:

Table 7. Summary of criterion for test performance

Test Type	Statistical Test	Group	Criterion 1: Number of Samples per Group	Criterion 1 Rank	Criterion 2: Average *p*-value	Criterion 2 Rank	Manning's *n*	Std. Dev. of Manning's *n* values	Criterion 3 Rank
Multi-Sample	Kruskal-Wallis	A	10	1	0.245	4	0.0839	0.005	1
		B	2				0.0792		
		C	2				0.0744		
	ANOVA	A	10	1	0.154	5	0.0839	0.000	4
Two-Sample	Kolmogorov-Smirnov	A	5	3	0.276	3	0.0839	0.000	4
		B	4				0.0839		
		C	2				0.0839		
	Mann-Whitney	A	6	2	0.409	1	0.0839	0.003	2
		B	5				0.0839		
		C	4				0.0792		
		D	3				0.0792		
	t- test	A	6	2	0.343	2	0.0839	0.003	2
		B	5				0.0792		
		C	4				0.0792		
		D	2				0.0839		

A Thiessen polygon map was generated from grain size sample locations and used as a basis for generating all of the maps for sample groupings. Figure 16 shows results for the Kruskal-Wallis test; additional plots are shown in Appendix A. Areas covered by vegetation were excluded from the Thiessen polygon mapping. The silt and sand samples were categorized as unassigned.

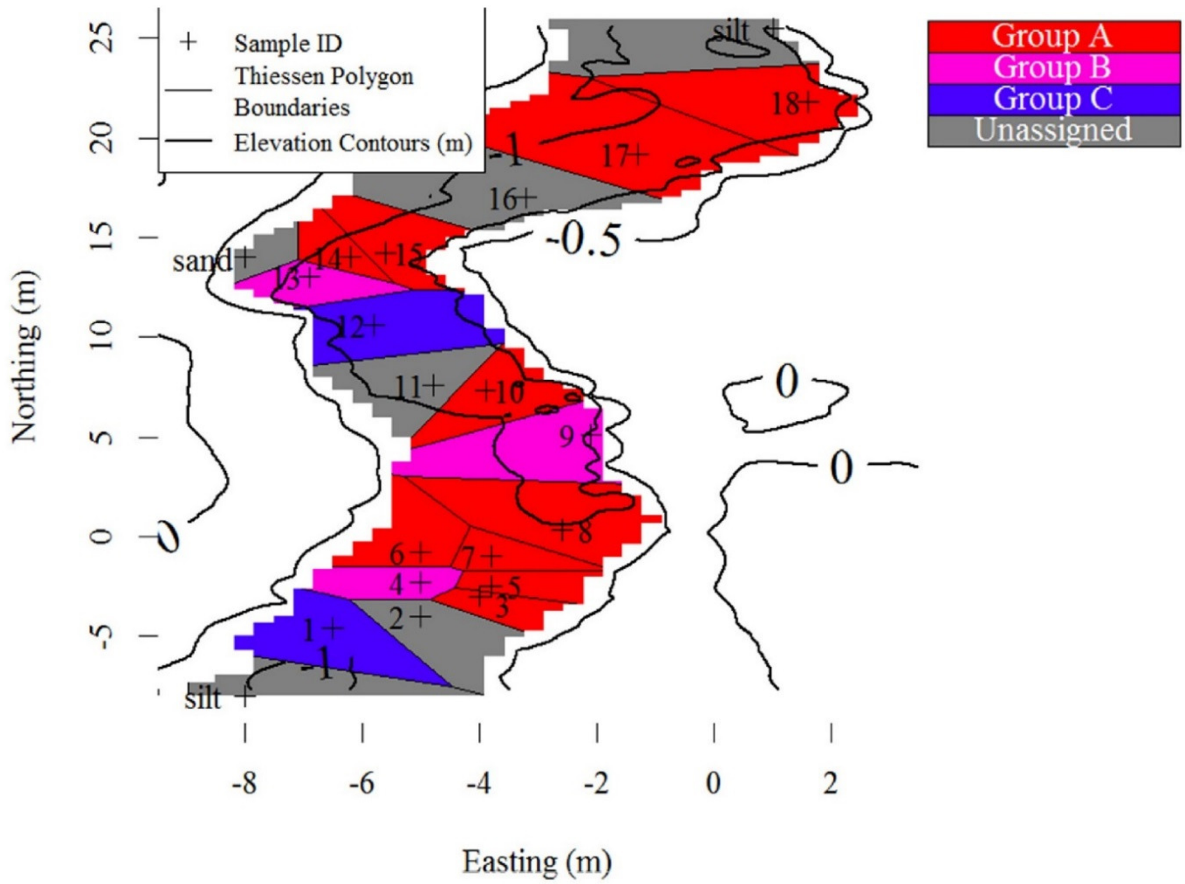

Figure 16. Thiessen polygon map of grain size groups for Kruskal-Wallis test

3.6.2. Hydraulic Modeling

Each of the surfaces generated by the statistical tests was then used to initialize a hydraulic model. The flow rate was a constant 1.5 m^3/s for the two hour duration of each simulation. Results will be presented using two main plot types: time series (spatial average) and Lorenz curves. Tables will also be used for parameter values that were approximately constant throughout the model run. Lorenz curves have only recently been used to present hydraulic data (Clifford et al., 2005). Lorenz curves were historically used to determine the economic distribution of wealth within a society or country. However, the concept is easily adapted to hydraulic data: instead of wealth, a hydraulic parameter is observed (e.g., shear stress or depth); instead of observing the distribution amongst a population, the distribution is observed over the wetted area of a stream. Lorenz curves, as applied to hydraulic data, combine hydraulic data from every wetted grid cell in the computational domain at every time step. The resulting figure indicates the distribution of parameter values over both time and space, providing a visual examination of spatio-temporal differences between simulations. Computation results will be displayed beginning 120 seconds after the model is initialized. Bedload transport was delayed 120 seconds to allow for velocity and depth conditions to establish in the channel.

Table 8. Summary of hydraulic model results from surfaces generated by various statistical tests

Statistical Test	Average Hydraulic Parameters			
	Depth (m)	Velocity Magnitude (m/s)	Froude Number	Vorticity (1/s)
ANOVA	0.426	0.569	0.278	-0.0045
Kolmogorov-Smirnov	0.427	0.568	0.277	-0.0044
Kruskal-Wallis	0.429	0.574	0.284	-0.0043
Mann-Whitney	0.430	0.572	0.283	-0.0044
t -test	0.425	0.572	0.280	-0.0051
Uniform Surface	0.427	0.504	0.234	-0.0033

The differences in model performance were observed without bed deformation. Results of depth, velocity, and Froude number are shown below. Results for a uniform surface, created using the composite of all grain size measurements, are also included in the figures.

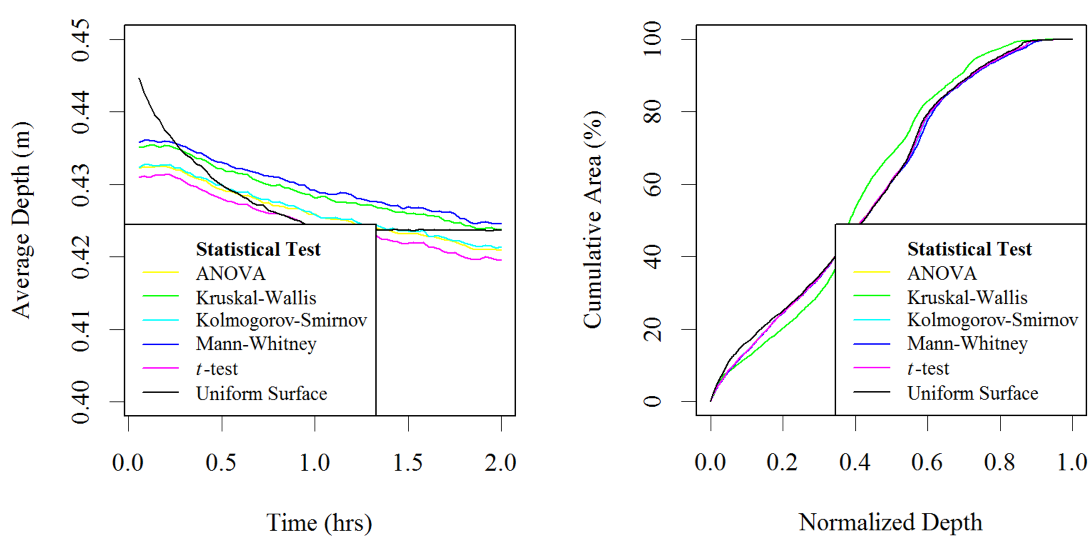

Figure 17. Time series (left) and Lorenz curve (right) of depth for simulations without bed deformation

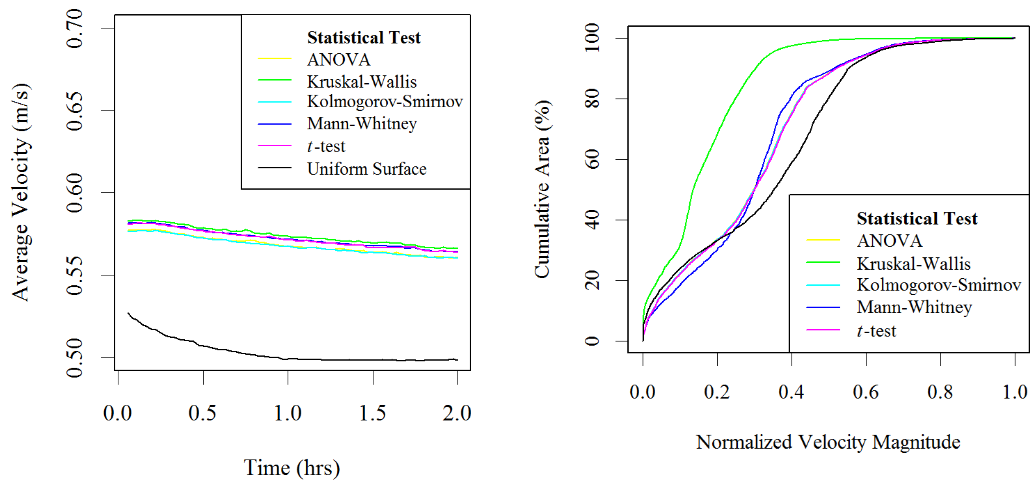

Figure 18. Time series (left) and Lorenz curves (right) of velocity magnitude for simulations without bed deformation

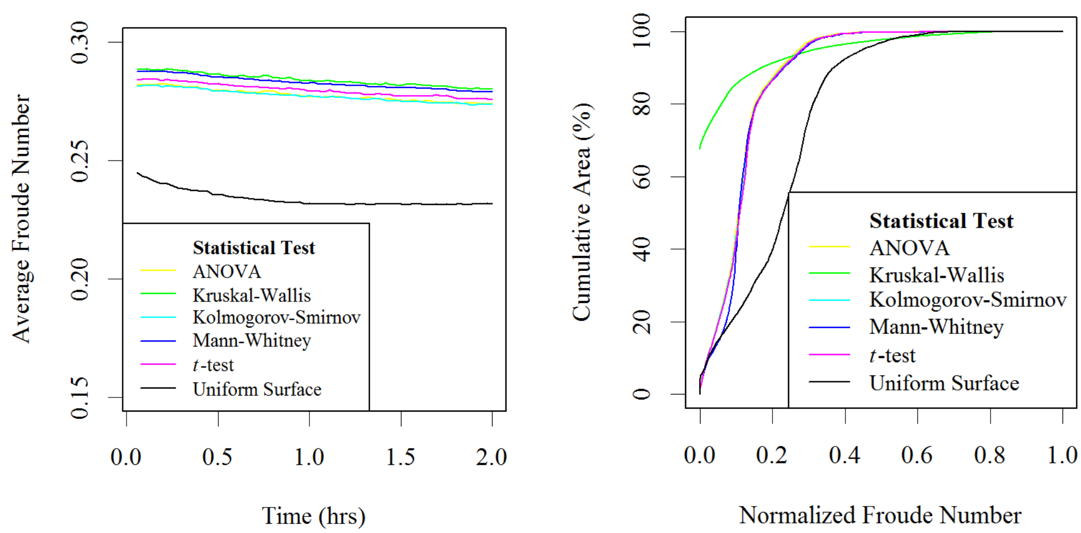

Figure 19. Time series (left) and Lorenz curves (right) of Froude number for simulations without bed deformation

3.7. Discussion

In this section, the results of statistical tests are first compared, then the hydraulic model results are addressed.

3.7.1. Statistical Analysis

According to the criterion established in the methodology, the Kruskal-Wallis test performed most favorably when grouping the grain size samples. Using the established criterion, the Kruskal-Wallis test created a group containing the most samples. Although the *p*-values calculated for the Kruskal-Wallis test were not the highest, they were higher than the *p*-value derived for the ANOVA test. The Kruskal-Wallis test requires the fewest assumptions, and is not susceptible to the familywise error rate increases. The Kruskal-Wallis test and ANOVA test both established a group containing 10 samples. However, the ANOVA test only established one group, while the Kruskal-Wallis test created three, and with greater *p*-values for each group (Table 6). Groups derived from two-sample tests are much more similar than those derived from the Kruskal-Wallis test (Appendix A and B). This is also apparent in the differences of grain size percentiles shown in Table 6; some test established groups that have the same grain size percentiles. Although they may be statistically different groupings, they do not produce different grain size diameter percentiles or Manning's *n* values.

The assumptions and conservativeness of the tests tended to dictate the number of statistical groupings and group size. The multi-sample tests were less conservative because they are not subject to an increased probability of Type I error from multiple tests (i.e., familywise error). As a result, the multi-sample tests formed statistical groupings containing more samples. While the average *p*-values in the two-sample tests are larger, the sample groupings between tests is less consistent. Group A samples in the multi-sample tests are almost identical (Table 5). However, the groupings of the two-sample test have few sample overlaps between tests. This lack of consistent groupings is most likely a result of the familywise error rate correction, which creates a more conservative significance value (α).

Despite the relatively large sample size of 120, many samples were still deemed statistically similar. The two-sample tests indicate that there are at least three or four distinct grain size distributions, with little to no spatial correlation (Figure 16). However, the two-sample tests are suspect due to their lack of consistent groupings and conservativeness. Results of the multi-sample tests are most likely a more accurate depiction of the true grain size distributions at the site. Multi-sample tests indicate that the surface is largely covered by one distribution. The gravel deposits on the stream bed are largely homogenous with respect to grain size distribution, which is indicated by the large grouping of 10 samples formed by the Kruskal-Wallis and ANOVA tests (Table 5).

3.7.2. Heterogeneity of Hydraulic Roughness

Heterogeneity with respect to hydraulic roughness is related to the grain size percentiles of the distributions. Table 6 provides insight into the usefulness of the statistical tests with respect to hydraulic modeling. The two-sample tests produced groups that had the same grain size percentiles, which produce the same Manning's n values; this is also apparent in Appendix B plots. The Kruskal-Wallis test did not form groups with the same percentiles, so those groupings produced a range of Manning's n values. Using the Kruskal-Wallis test to derive roughness values is advantageous because the test is non-parametric, and is capable of comparing multiple samples.

Non-parametric tests are more useful when establishing hydraulic roughness values because they use the rank of data. Hydraulic roughness is commonly computed by grain size percentiles, which are determined by grain size rankings. Multi-sample tests are also not as susceptible to familywise error rate increase. Of the tests used in this study, the Kruskal-Wallis test is most capable of quantifying the heterogeneity of hydraulic roughness. As indicated by Table 6, the Kruskal-Wallis test produces the least redundant Manning's *n* values. The question remains whether or not the heterogeneity observed in grain size percentiles is great enough to produce a difference in hydraulic model results. This question is addressed in the next section.

3.7.3. Hydraulic Models

Hydraulic models simulated non-deformable bed conditions, which elucidate the effects of roughness heterogeneity on flow. The only apparent differences in the hydraulic parameter results were observed in velocity and Froude number. Depth predictions from the simulations were within 4 mm (0.004 m) of each other, which implies that roughness heterogeneity is not a significant concern for flood risk assessments concerned with water depth (Table 8). Average velocity for the uniform surface was approximately 0.07 m/s (14%) lower than the other scenarios, indicating that the uniform roughness introduces more overall resistance to flow. Some fish energetics models (i.e., models simulating energy expenditure of a fish) use principles of a drag force to calculate fish energy and stamina (Statzner and Sagnes, 2009). Because drag force is proportionate to the square of velocity, fish energetics models that use a drag force approach are particularly sensitive to changes in velocity. So, even the small differences in velocity predictions observed between the uniform and heterogeneous surfaces are significant. Additionally, the Lorenz curves of velocity and Froude number for the uniform and Kruskal-Wallis surface show diverge from the other statistically derived surfaces (Figure 18, Figure 19). Variances in the Lorenz curves indicate different spatial distributions of velocity and Froude number, which are also important in fish energetics model predictions (Statzner and Sagnes, 2009).

3.8. Conclusion

In the context of developing a hydraulic model from grain size samples, the Kruskal-Wallis test produced the most favorable results compared to four other statistical tests. Using the Kruskal-Wallis test, large sample groupings were produced that also had the greatest differences in derived Manning's n values. Two-sample tests were shown to be overly-conservative when grouping samples due to the associated familywise error rate. As a result, sample groupings were inconsistent between two-sample tests, and showed little spatial correlation. Hydraulic models of the statistically derived surfaces showed large differences in predicted velocity (13%), indicating that the roughness heterogeneity is a biologically significant factor. Results of this chapter indicate that analysis of stream habitats would benefit from a heterogeneous roughness representation, developed by examining grain size heterogeneity.

CHAPTER 4: SEDIMENT TRANSPORT MODELING OF A HETEROGENEOUS GRAVEL BEDDED STREAM

This chapter examines the hydraulic model predictions from various configurations of roughness and grain size distribution representations in hydraulic models. One of the Thiessen polygon surfaces produced in Chapter 3 will be used as a representation for grain size and roughness regions. Both roughness and grain size heterogeneity are modeled using different surface representations. The terms roughness and Manning's *n* will be used interchangeably throughout this chapter. Also, as in Chapter 3, the term *sample* in this document refers to a collection of grain size measurements gathered from a single location, making up a grain size distribution.

4.1. Abstract

Sediment transport models are often used to make predictions for assessments of flood risk, habitat quality, and other purposes. The accuracy of these predictions influences the decisions made during projects, so it is important to appropriately represent the natural environment to achieve a desired accuracy. A large influence on the uncertainty of hydraulic models is the heterogeneity of the stream bed. This study quantifies some of the uncertainty associated with grain size heterogeneity through sediment transport modeling. Sediment transport models are initialized with various spatial configurations of grain size and roughness. The relative differences in model performance are compared to results from a spatially uniform surface. Simulations of non-deformable surfaces are used to explore the effects of roughness heterogeneity on flow properties. Roughness is shown to minimally change depth predictions, but varied velocity predictions by up to 14 %, with increasing differences with flow rate. Simulations of deformable surfaces examine the effects of grain size heterogeneity. Results indicate that prediction of bedload

transport and bed material composition may vary by approximately 20% between a uniform and heterogeneous representation. The study provides evidence that grain size heterogeneity influences flow and sediment transport predictions of hydraulic models, and will significantly influence any subsequent interpretation of the model results. Analyses of gravel bedded streams will reduce uncertainty in hydraulic models by considering the influence of grain size heterogeneity.

4.2. Introduction and Purpose

Sediment is one of the most globally problematic pollutants, affecting both people and the environment in the U.S. (EPA, 2004). Since the advent of agriculture and silviculture (i.e., growing forests as crops), anthropogenic erosion rates have far outpaced the natural background rates for the current climatic age (Montgomery, 2012). As a result, streams and rivers have undergone extreme changes due to anthropogenic alterations to the landscape (Mount, 1995). Levees and channelization have more obvious, direct impacts. But, the physical and biological impacts from nonpoint sources like agriculture and silviculture are much more difficult to quantify (Chang, 2003; Bathurst and Iroume, 2014). Hydraulic models have become a powerful tool to assess changes in rivers and streams (Wu, 2008). Sediment transport models are important tools in many risk and habitat assessments, but are subject to uncertainty due to the complexity of the natural environment. Previous research has shown that the effects of roughness heterogeneity influence velocity predictions in hydraulic models (Chapter 3). The objective of this chapter is to address the second research question stated in section one: is grain size heterogeneity important for sediment transport modeling purposes? The effects of grain size heterogeneity are explored using predictions of flow and sediment transport for a small creek in northern Idaho.

Two factors controlling sediment transport are the resistance of the stream surface, or roughness, and the grain size of the bed material (Julien, 2010). It is typical to assume that a streambed is uniform with respect to grain size due to the extensive data requirements of characterizing the surface heterogeneity. However, the assumption of uniformity may not be appropriate in gravel bed streams where there are zones of widely varying grain sizes, resulting in variations of flow resistance and sediment transport (Guerit, 2014; Garcia, 1999). In this study, Thiessen polygon discretization as well as the geostatistical approach of kriging have been applied to map streambed roughness and the distribution of grain size in a gravel bedded stream. Kriging is a stochastic method that predicts how the mean and standard deviation of a parameter change spatially, allowing for a better representation of heterogeneity. The purpose of this study is to observe the relative differences in hydraulic model predictions using both uniform and heterogeneous surface representations. Velocity, depth, bedload transport, and other metrics are used as a basis for comparison. To explore the interdependencies of roughness and sediment transport, simulations are conducted with bed deformation. The hydraulic modeling software used to conduct this analysis is Nays2DH, which was created by the International River Interface Cooperative (iRIC), (Shimizu et al., 2015). Nays2DH is a two dimensional flow and sediment transport model, capable of predicting aggradation and degradation of mixed size sediment, and bank erosion. Predictions of the hydraulic models are interpreted in the context of the physical and biological impacts to the stream environment.

4.3. Background and Motivation

Grain size influences two components of flow in both physical settings and hydraulic models: roughness and sediment transport. The main purpose of this analysis is to observe relative differences in representations of roughness and grain size in hydraulic models. Consider two stream beds composed of rounded particles: a heterogeneous (poorly sorted) gravel bed, and a uniform (well sorted) sand bed (Figure 20). Flow over the uniform surface is obstructed by the very small protuberances in the bed resulting from the settling positions of sand particles (Figure 20, right). With respect to sediment transport, the uniform surface only presents one grain size for bedload transport, distributed evenly over the surface.

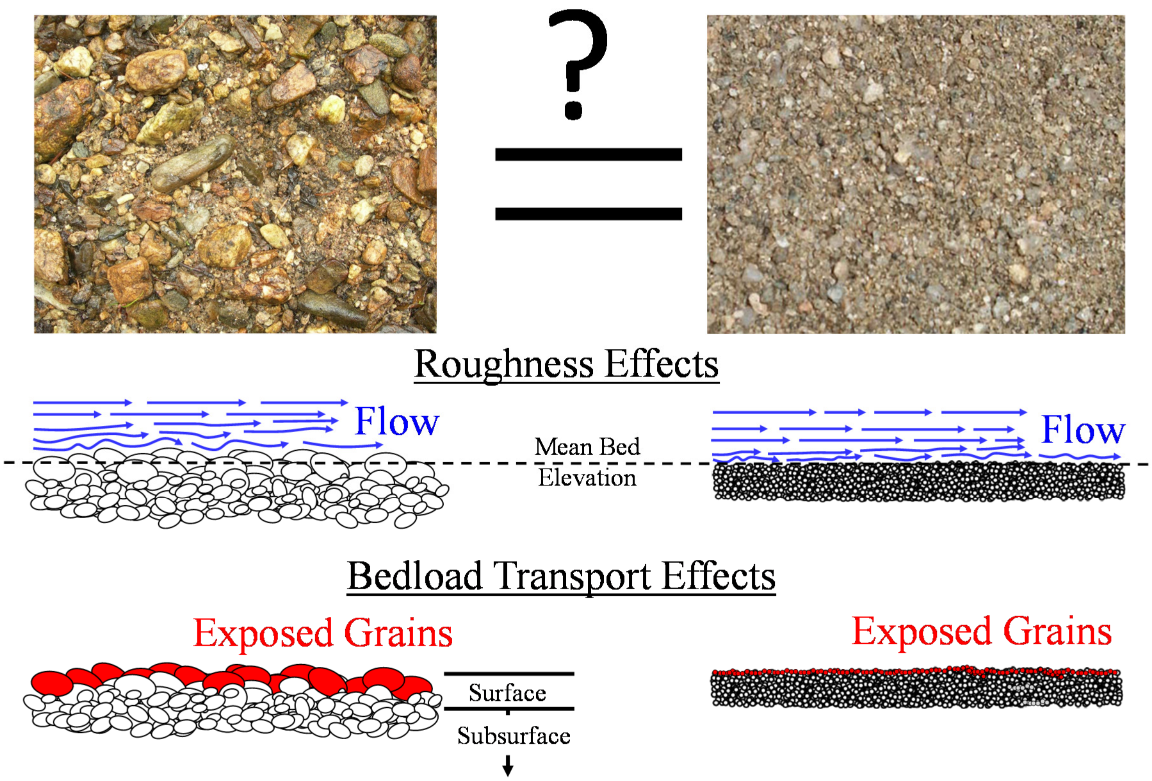

Figure 20. Heterogeneous (left) and uniform (right) grain sizes and their effect on flow and bedload transport

In contrast, the gravel bed surface is much rougher, and larger protuberances are present because the grains extend further above the average bed surface (Figure 20, left). Additionally, mixed size sediment like gravel beds develop a surface layer, also called an armor or pavement layer, which is typically made up of larger grains than the subsurface layer. Smaller grains are hidden from flow because they are able to pass through the gaps between the larger grains on the surface. Thus, only larger particles are available for bedload transport, requiring a much larger shear stress to produce incipient motion than would be expected from the bulk grain size distribution. The exception to the typical bedload transport process in gravel streams is when the pavement layer is removed in higher flows, exposing the smaller subsurface particles. Other possible configurations for stratification exist in gravel beds, depending upon the shape and standard deviation (i.e., degree of sorting) of the grains. However, a majority of these possible configurations have larger grains in the surface layer (Church et al., 1987).

The three types of surface representations used in this study are uniform, polygon, and smoothed surfaces (Figure 21), (Csillag, 1996). These surfaces are generated from the median grain size, Thiessen polygons, and kriged, respectively. Each representation type has its own advantages and associated assumptions. By using a uniform surface, the assumption is made that the spatial heterogeneity of hydraulic roughness is limited enough that no difference will be present even if a heterogeneous representation were used. With regard to stream beds, this assumption may apply to uniform grain sizes such as sand beds or other well sorted channels. Uniform surfaces have the advantage of simplicity when initializing a hydraulic model.

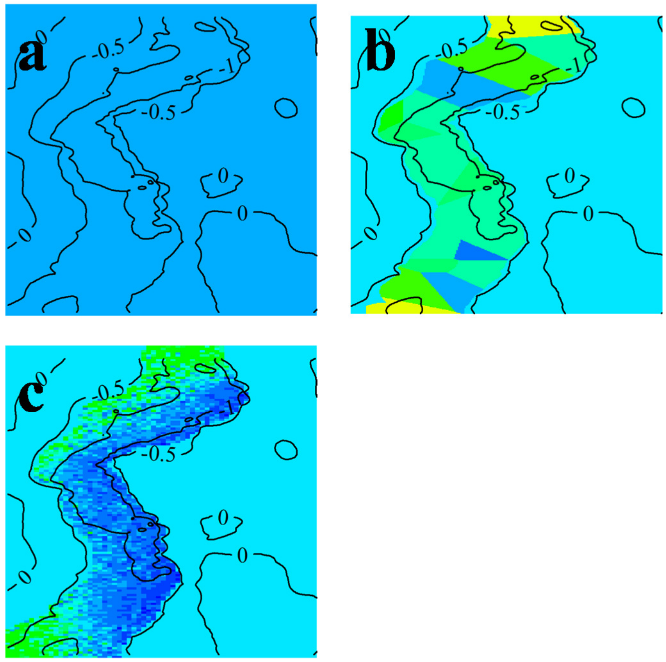

Figure 21. Surface representations: a) uniform, b) Thiessen polygons, and c) kriged. Elevation contours shown. Floodplain area above approximately -0.6 m in elevation were excluded from surface representation.

Thiessen polygons are useful when a surface is heterogeneous, but the geometry of the spatial heterogeneity is not known (Figure 21, b). Thiessen polygons are commonly applied to rainfall data, where point estimates are available for rainfall depth, but the area-weighted rainfall depth over an area is desired. Assigning a bulk value to a polygon area simplifies hydraulic model initialization. The generation of Thiessen polygons is relatively simple, and programming code is readily available for use. With respect to a physical interpretation for Thiessen polygons, they are most similar to bedforms in a stream, where the roughness and/or grain size may be considered to be spatially distributed in patches.

Lastly, a smoothed surface assumes that there is a gradual, spatial change of the mean parameter value that cannot be captured by a uniform or Thiessen polygon approach (Figure 21, c). Creating a smoothed surface requires establishment of the covariance relationship between points. This study uses a kriging approach, which fits a semi-variance model to data. The semi-variance model is then used to predict both the mean and standard deviation of point estimates over the desired domain. Kriging is more complex and computationally intensive than other methods, but has been shown to be a very powerful tool (Kitanidis, 1996). Kriging may be interpreted as modeling the more gradual changes in channel complexity, such as the gradual fining or coarsening of grain sizes along and across the channel. These gradual changes are not captured by a Thiessen polygon or uniform representation.

An additional component of this study uses Monte Carlo simulation to create multiple realizations of hydraulic roughness over the streambed (see sections 2.3 and 2.4 in Literature Review). Kriging has been demonstrated to predict parameter values within a 95% confidence level (Kitanidis, 1996). However, error in kriging prediction increases as the distance of the extrapolated point increases from known (measured) point locations. This error creates a range of probable parameter values that cannot be represented by the mean alone. Monte Carlo sampling allows for the usage of information provided by both the mean and standard deviation of predictions from kriging. Multiple Monte Carlo realizations of a kriged surface create a more accurate representation of true parameter values. Performing Monte Carlo simulation on kriging results is not a new concept; it has been used in subsurface modeling for many decades (Gelhar, 1986). However, the application of this stochastic approach to hydraulic roughness has not been explored.

4.4. Methodology

There are three main components required to initialize the physical portion of the Nays2DH hydraulic model: 1) stream channel geometry (bathymetry), 2) hydraulic roughness (Manning's *n*), and 3) grain size distribution of the bed material. Each of these components requires data and processing prior to use in the hydraulic model. In this section, a description is first provided of the data collection. Next, methods used to calculate the different roughness and grain size surfaces are explained. Nays2DH is briefly described in addition to the parameter values required to initialize the simulations.

4.4.1. Data Collection

Data were collected from the Cat Spur Creek watershed, located in northern Idaho (see section 3.3.1). Bed material at the site is comprised of poorly sorted gravel, sand, and silt (Figure 5). An extensive elevation survey was conducted to characterize bed elevation (see section 3.3.2). Resolution of the survey was approximately 1 m in the longitudinal direction and 0.25 m in the transverse direction. Bed material measurements were also collected to characterize the grain sizes at the site. A total of 18 samples were collected, with approximately 120 grains measured per sample (see section 3.3.4).

4.4.2. Manning's *n*

Hydraulic roughness in the Nays2DH software is determined by the Manning's *n* coefficient value. Nays2DH is only capable of representing one roughness value for each grid cell in the model. So, the roughness effects of an entire grain size distribution must be reduced to a single value. A common approach is the Manning-Strickler equation:

$$\boldsymbol{n} = \frac{\boldsymbol{k_s}^{1/6}}{7.66\sqrt{\boldsymbol{g}}} \qquad (4.1)$$

where,

k_s = relative roughness height (m)

Relative roughness is related to a sediment size diameter within the range of the grain size distribution.

$$\boldsymbol{k_s} = \boldsymbol{\alpha D_x} \qquad (4.2)$$

where,

α = empirical constant between 1 and 3

D_x = representative grain diameter (m), (e.g., D_{50}, D_{84})

The subscripts on the representative grain size diameter indicate the percentage of grains in the grain size sample that are finer than the given diameter. This is the same concept as a percentile in a cumulative distribution function. In Figure 22 below, the D_{84} percentile of the sample is approximately 10 mm.

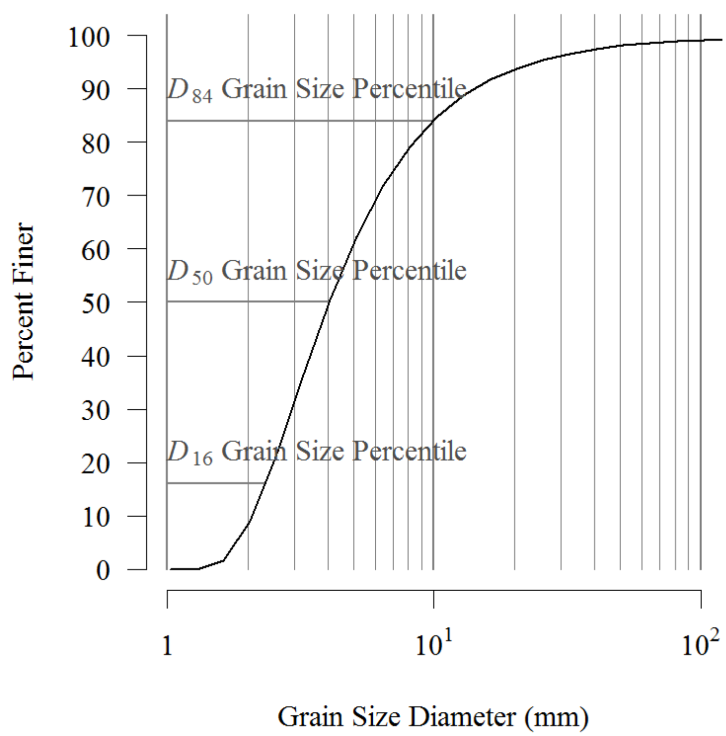

Figure 22. Example cumulative distribution of grain size diameters

The appropriate combinations of empirical constant (α) and representative grain size (D_x) in literature are extensive. From Yen, 1991, D_x varies between D_{35} and D_{90}, α_m varies between 1.0 and 6.6. Because larger grains are more exposed, they have a greater role in resisting flow. Thus, larger grain size percentiles are typically used as the representative grain size, D_x. For this study, the Manning-Strickler coefficients for α and D_x were 2.95 and D_{84}, respectively (Whiting and Dietrich, 1990). The selection of Manning-Strickler coefficients is arbitrary, and the effect on the overall results will be negligible because the analysis is only concerned with the *relative* differences between surface representations. Manning-Strickler coefficients are kept constant, and the relative differences between model performances will remain the same.

4.4.3. Roughness Surface Representation

The actual parameter value for Manning's n may be approximated if a grain size or grain size distribution is provided for a location. The three possible roughness surface configurations used in this study are the uniform, Thiessen polygon, and kriged-Monte Carlo. The uniform roughness surface was established by aggregating the grain size measurements, and determining the desired grain size percentile of the composite sample. The Manning-Strickler equation (Eq. 4.1) was then used to determine the Manning's n value, which was applied to all grid cells within the computational domain. The Thiessen polygon geometry, and grain size distributions associated with the polygons were established through statistical testing. The Kruskal-Wallis H test was applied to grain size samples, and the sample groups were established based on average p-value and number of samples per group; higher p-values and larger groups were preferred. The Thiessen polygon geometry was determined by grain size measurement locations. Each Thiessen polygon is associated with a grain size sample. Using the results of the statistical tests, samples are assigned to a statistical grouping that has an associated grain size distribution and D_{84} grain size percentile. Similar to the uniform roughness, the Manning-Strickler equation is applied to the D_{84} values, except each polygon is assigned a Manning's n value. Kriging was applied to the grain size measurement locations and corresponding grain size percentiles from the samples. A surface representing the D_{84} grain size percentile was kriged using an exponential semi-variogram (see

Appendix D for semi-variogram selection). Then, the Manning-Strickler equation was applied to each kriged point to create a Manning's *n* surface.

4.4.4. Grain Size Surface Representation

Due to constraints imposed by the hydraulic modeling software, only a single grain size distribution was applied uniformly for the kriging-Monte Carlo surface type. The Nays2DH solver is only capable if simulating up to ten separate grain size distributions. The grain size distributions are loaded into the software, then grid cells are assigned to those distributions. The kriging-Monte Carlo method produces a smoothed surface, so there are no distinct boundaries defining separations of grain size distributions. Each cell could potentially have a unique grain size distribution, similar to the actual stream surface.

For the uniform grain size representation, the aggregate grain size distribution was applied over the entire computational domain. For the Thiessen polygon grain size representation, the geometry of the polygons was defined by the sampling locations of the grain size measurements. The grain size group assigned to each polygon are defined by the Kruskal-Wallis statistical test. Grain size distributions and spatial locations derived with the Kruskal-Wallis test are shown in Appendices A and B.

4.4.5. Initializing Hydraulic Models

Numerous conditions need to be set to properly initialize the Nays2DH model. Boundary conditions are of particular importance. Conditions used in this analysis and the justification for their selection are provided in this section. Because the relative influence of each surface is to be determined, the boundary conditions were first established for some preliminary models, then kept consistent throughout each model simulation, with the exception of some models used to perform the sensitivity analyses.

Through experimentation with preliminary models, the boundary conditions and calculation settings were established. Asterisks indicates parameters selected for sensitivity analysis and subsequent parenthesis are values used in the sensitivity analysis:

Table 9. Calculation conditions and parameters selected for sensitivity analyses

Calculation Condition	**Value**
Flow Rate* (m^3/s)	1.5 (0.25, 0.5, 1.5, 4.0)
Bedload Transport Equation	Ashida and Michiue (see Appendix C)
Computatoinal Grid Resolution* (m)	0.25 (0.125, 0.25, 0.5, 1.0)
Upstream Velocity	Determined from uniform flow
Downstream Water Surface Elevation	Determined from uniform flow
Boundary Conditions	Non-periodic
Finite Difference Solver	Cubic-Interpolated Pseudoparticle (CIP)
Percentage Equilibrium Sediment Discharge (%)	100
Calculation Time Step (s)	0.02
Simulation Time (hrs)	2

Flow Rate

The desired flow rate will induce bedload transport, so a flood flow of 1.5 m^3/s was selected. Using previously collected flow data, this flow was deemed to correspond two year return interval flood, and induced bedload transport in preliminary models (Figure 23). Flow rate was held constant throughout each model run.

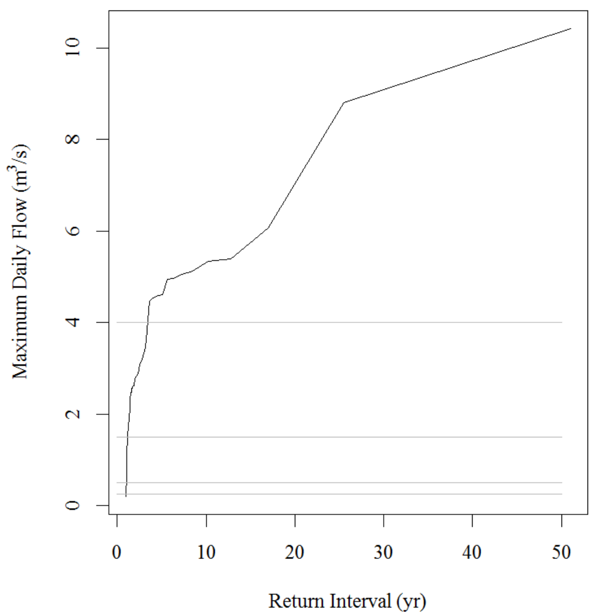

Figure 23. Return intervals and corresponding peak flow for Cat Spur Creek, ID (BAT, 2014)

Bedload Transport Equation

For non-uniform grain size representation (i.e., simulation of bedload transport for a grain size distribution), the only option in the Nays2DH software was the Ashida and Michiue bedload transport equation (Appendix C). This equation was used for all simulations of bedload transport.

Computational Grid Resolution

No recent bedload data are available for this study to validate the appropriateness of selected grid resolution. However, relative effects of model performance should remain consistent with changes in grid resolution. Grid resolution was selected based upon computation time, grid resolution used in similar studies, and physical interpretation (Wu, 2004). A grid resolution that is smaller than the largest particles size would have little physical interpretation. The largest particles in Cat Spur Creek were 90 mm (0.09 m), so a grid resolution of 0.125 m is close to the finest grid resolution that is appropriate. Differences in model performance with grid size were explored in the sensitivity analysis.

Boundary Conditions

The options for the downstream boundary condition in Nays2DH are constant water surface elevation or a determination from uniform flow. Both settings were attempted using preliminary models, and fixing the depth required calibration for each surface type. Additionally, fixing the water surface elevation at the downstream end may prevent differences in surface representation from being simulated. Thus, the downstream water surface elevation was calculated assuming a uniform flow condition at the boundary, a close approximation for constant flow rate through a minimally changing channel. For the upstream boundary, velocity is also calculated assuming uniform flow.

An important consideration when initializing a hydraulic model is the boundary conditions. In the Nays2DH solver, there are two options: periodic and non-periodic. The periodic boundary conditions simply set the downstream output as the upstream input. The sediment, velocity, and flow depth at the ends of the numerical grid are set to be equal. Using the non-periodic boundary conditions, the model establishes the upstream depth and sediment input by calculating equilibrium conditions. Equilibrium conditions are determined from the downstream output, and sediment input is set as a fraction of the equilibrium, or downstream, sediment discharge (i.e., 75% or 100%). There has been much debate in literature over whether natural streams are best reproduced by non-periodic or periodic boundary conditions (Parker et al., 1982). Experiments have been conducted with both a recirculating flume (replicating periodic conditions), and a feed system (replicating non-periodic conditions). Ultimately, natural streams operate as a hybrid of periodic and non-periodic systems (Wilcock and Southard, 1989; Parker et al., 1982). Two primary factors controlling the periodicity of natural streams are prior flow and sediment transport conditions. For this study, non-periodic boundary conditions were used for two primary reasons: model stability and the presence of fine material in the bedload. However, periodic boundary conditions were considered.

Periodic boundary conditions reproduce a recirculating feed system, where sediment from downstream is diverted to the upstream input. So, periodic boundary conditions are typically used to replicate laboratory experiments, or designed channels with repeating features such as fish ladders. To justify using periodic boundary conditions to model a natural stream, sufficient data are required to validate the assumption. Wilcock and Southard (1989) state that for short time periods of several hours or less, periodic boundary conditions may be appropriate. Experimentation with periodic boundary conditions shows that there are severe issues with model instability. Because natural channels do not have a uniform cross-section, equating the upstream and downstream velocity profiles causes a misalignment of boundary conditions. Large eddies and countercurrents were observed at both the upstream and downstream boundaries (Figure 24). The Nays2DH solver does not currently provide the option to separate periodicity of sediment transport and velocity conditions.

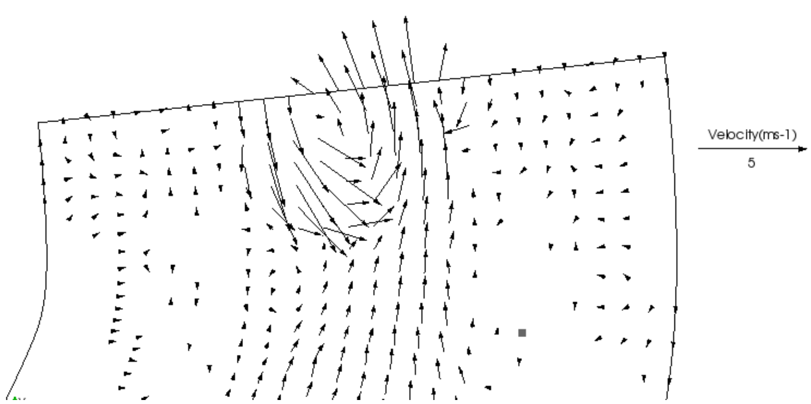

Figure 24. Areal plot of periodic boundary conditions, instability of velocity field at downstream boundary caused by misalignment of upstream and downstream channel cross-sections

Non-periodic boundary conditions produced much more stable model conditions. Velocity, sediment transport, and depth were free to change at the boundaries. The use of non-periodic boundary conditions is supported by Milhous, 1973; when a large portion of the bed material is represented by fines, the system acts like a non-periodic feed system. Sediment transport data collected by the Boise Adjudication Team indicates that bedload at Cat Spur Creek has been dominated by fine material less than two millimeters in diameter (BAT, 2014).

Finite Difference Solver

Nays2DH uses a finite difference approach, with two solver options: upwind scheme, and Cubic-Interpolated Pseudoparticle (CIP) method. The CIP method has been demonstrated to provide a stable, efficient solution to nonlinear problems (Yabe et al., 1990). The CIP method was used for all simulations.

Simulation Time

All of the observed parameters (i.e., velocity, depth) exhibited asymptotic behavior that had either stabilized or was approximated by a linear trend after two hours. So, a simulation time of two hours was selected to allow for differences in model behavior to be observed. This selection also minimized computational effort.

Additional Adjustments for Model Initialization

In addition to the previously listed conditions, a non-erodible upstream channel extension was added to stabilize upstream velocity prior to reaching the erodible portion of the channel. Experimentation with preliminary models showed that the velocity profile required approximately five meters to stabilize; a ten meter extension was used to ensure that the upstream velocity conditions were established.

Nays2DH allows for the possibility of delaying the simulation of bedload transport after model initialization. This setting is useful to allow for the establishment of the water surface elevation and velocity conditions in the stream prior to simulating bedload transport. Preliminary models indicated that the depth in the non-erodible stream channel was essentially stable after approximately 90 seconds. Thus, bedload transport calculation commenced after 120 seconds of flow simulation.

4.4.6. Model Scenarios

The following matrix outlines all of the model simulations (scenarios) required to evaluate roughness heterogeneity, grain size distribution heterogeneity, and perform the sensitivity analyses. There will be three main types of model scenarios performed, each with a different type of representation for the grain size distribution (GSD) and/or Manning's *n* value: uniform, Thiessen polygon, and kriging-Monte Carlo. Within these main classifications, there are some variations to account for different grain size percentiles (i.e., D_{16}, D_{50}, or D_{84}) and representation of a grain size distribution (GSD).

Table 10. List of simulations

Model Scenario Description	Manning's n Representatoin	Grain Size Representation	Flow (m^3/s)	Grid Resolution (m)
No Bedload Transport Scenarios				
Uniform	Uniform, D_{84}	Uniform, D_{84}	0.5	
Uniform	Uniform, D_{84}	Uniform, D_{84}	1.5	
Thiessen Polygon	Thiessen Polygon, D_{84}	Thiessen Polygon, D_{84}	0.5	
Thiessen Polygon	Thiessen Polygon, D_{84}	Thiessen Polygon, D_{84}	1.5	
Kriging - Monte Carlo	Monte Carlo Realizations, D_{84}	Uniform, D_{84}	0.5	
Kriging - Monte Carlo	Monte Carlo Realizations, D_{84}	Uniform, D_{84}	1.5	
Bedload Transport Scenarios				
Uniform	Uniform, D_{16}	Uniform, D_{16}	1.5	
Uniform	Uniform, D_{50}	Uniform, D_{50}	1.5	
Uniform	Uniform, D_{84}	Uniform, D_{50}	1.5	
Uniform	Uniform, D_{84}	Uniform, D_{84}	1.5	
Uniform	Uniform, D_{84}	Uniform, GSD	1.5	
Thiessen Polygon	Thiessen Polygon, D_{84}	Thiessen Polygon, D_{50}	1.5	
Thiessen Polygon	Thiessen Polygon, D_{84}	Thiessen Polygon, D_{84}	1.5	
Thiessen Polygon	Thiessen Polygon, D_{84}	Thiessen Polygon, GSD	1.5	
Kriging - Monte Carlo	Monte Carlo Realizations, D_{84}	Uniform, D_{50}	1.5	
Kriging - Monte Carlo	Monte Carlo Realizations, D_{84}	Uniform, D_{84}	1.5	
Kriging - Monte Carlo	Monte Carlo Realizations, D_{84}	Uniform, GSD	1.5	
Flow Rate Sensitivity				
Thiessen Polygon	Thiessen Polygon, D_{84}	Thiessen Polygon, GSD	0.25	
Thiessen Polygon	Thiessen Polygon, D_{84}	Thiessen Polygon, GSD	0.5	
Thiessen Polygon	Thiessen Polygon, D_{84}	Thiessen Polygon, GSD	1.5	
Thiessen Polygon	Thiessen Polygon, D_{84}	Thiessen Polygon, GSD	4	
Uniform	Uniform, D_{84}	Uniform, GSD	0.25	
Uniform	Uniform, D_{84}	Uniform, GSD	0.5	
Uniform	Uniform, D_{84}	Uniform, GSD	1.5	
Uniform	Uniform, D_{84}	Uniform, GSD	4	
Kriging - Monte Carlo	Monte Carlo Realizations, D_{84}	Uniform, GSD	0.25	
Kriging - Monte Carlo	Monte Carlo Realizations, D_{84}	Uniform, GSD	0.5	
Kriging - Monte Carlo	Monte Carlo Realizations, D_{84}	Uniform, GSD	1.5	
Kriging - Monte Carlo	Monte Carlo Realizations, D_{84}	Uniform, GSD	4	
Grid Resolution Sensitivity				**Grid Resolution (m)**
Thiessen Polygon	Thiessen Polygon, D_{84}	Thiessen Polygon, GSD	1.5	0.125
Thiessen Polygon	Thiessen Polygon, D_{84}	Thiessen Polygon, GSD	1.5	0.25
Thiessen Polygon	Thiessen Polygon, D_{84}	Thiessen Polygon, GSD	1.5	0.5
Thiessen Polygon	Thiessen Polygon, D_{84}	Thiessen Polygon, GSD	1.5	1

4.4.7. Basis for Comparing Results

The list of output variables from the Nays2DH software is extensive. At each time step, and each grid cell, the following variables are available:

Table 11. Parameters used to compare results of hydraulic model simulations

Computed Parameter	Units	Interpretation
Vorticity	s^{-1}	The tendency of flow to rotate; indicates the presence of circulating flow
Froude Number	unitless	The ratio of inertial forces to gravitational force; used to determine current energy state of flow (i.e., subcritical or supercritical)
Depth	m	Water depth
Shields Parameter (τ_*)	unitless	Ratio of shear stress to particle diameter, density, and gravity; used to determine whether bed material is in motion and magnitude of change.
Bedload Transport	kg/s	The rate at which bed material is being moved downstream
Mean Grain Size of Bed Material	mm	Composition of bed material; important for deriving biological significance. Salmon species are particularly sensitive to changes in bed material.
Aggradation/Degradation	mm	Elevation changes of bed material

Shields parameter is commonly used in sediment transport to determine if incipient motion has occurred. The difference between Shields parameter and some threshold value for a particular sediment size is used to determine the magnitude of bedload transport. Shields parameter is calculated by the following equation:

$$\tau_* = \frac{\tau_0}{(\rho_s - \rho)gd} \tag{4.3}$$

where,

τ_0 = shear stress (N/m^2)

ρ_s = density of bed material (kg/m^3)

ρ = density of water (kg/m^3)

g = gravitational acceleration (m/s^2)

d = diameter of bed material (mm)

Although Nays2DH does simulate the fractional transport of mixed size sediment, the software does not output the results of the analysis due to limit the extent of data output. Only the mean grain size diameter of the bed material is available to infer grain size distribution changes over the stream surface. Additionally, when simulating a non-deformable bed, shear stress is not provided.

4.5. Results

Results are presented using two main plot types: time series (spatial average) and Lorenz curves (Figure 25). Tables will also be used for parameter values that were roughly constant throughout the model run. Time series are common plot types, however, the Lorenz curve has only recently been used to present hydraulic data (Clifford et al., 2005). Lorenz curves have historically been used to determine the economic distribution of wealth within a country. However, the concept is easily adapted to hydraulic data: instead of wealth, a hydraulic parameter is observed (e.g., shear stress or depth). Instead of observing wealth distribution amongst a population, a hydraulic parameter distribution is observed over the wetted area of a stream (Figure 25).

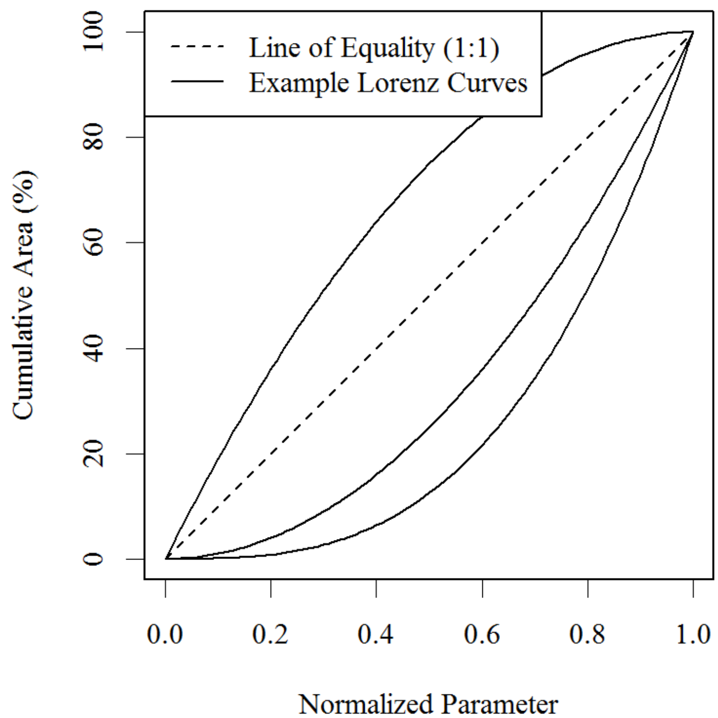

Figure 25. Example Lorenz curve

Lorenz curves, as applied to hydraulic data, combine hydraulic data from every wetted grid cell in the computational domain at every time step. Data are ranked, then normalized by the minimum and maximum value, so all values are between zero and one. Because data are obtained from all the wetted grid cells, the data also represent the proportional area each value occupies. The resulting figure indicates the cumulative distribution of parameter values over both time and space, providing a visual examination of spatio-temporal differences between simulations. The line of equality in Figure 25 indicates an even parameter distribution. In terms of economic wealth, the equality line would indicate that each portion of a population possesses an equal portion of the total wealth (e.g., half of the population has half of the wealth, 75% of the population has 75% of the wealth, etc…). Deviations from the line of equality indicate an uneven spatial or temporal distribution. If the Lorenz curve is above the line of equality, economically this would indicate that there are not very many wealthy people. Lorenz curves, when applied to wealth, are typically below the line of equality, meaning that a small part of the population has a large amount of the wealth. As applied to hydraulic parameters, when the Lorenz curve is above the line of equality, the distribution of the parameter is skewed towards smaller values. Conversely, when the Lorenz curve is below the line of equality, the distribution of the parameter is skewed towards larger values.

4.5.1. Roughness Surfaces

The roughness surfaces for the uniform, Thiessen polygon, and kriged-Monte Carlo methods are shown below (Figure 26). Due to the presence of vegetation at elevations greater than approximately -0.6 m, these areas were excluded from the roughness maps and set to a different roughness value. In typical model simulations, the water surface never extended into vegetated areas.

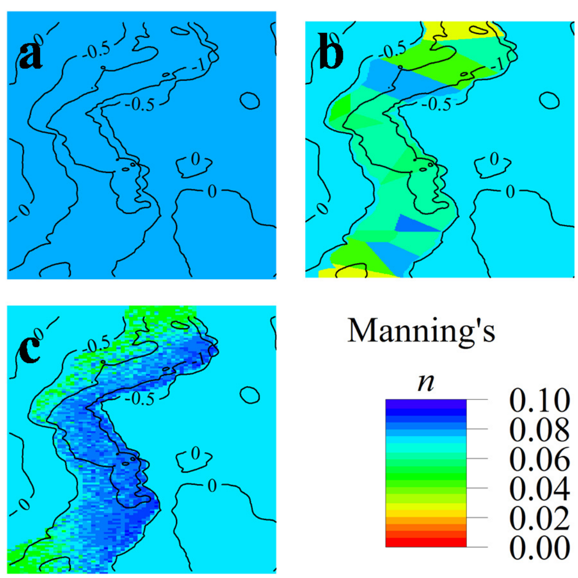

Figure 26. a) Uniform , b) Thiessen polygon, and c) kriged-Monte Carlo roughness surfaces

4.5.2. Grain Size Region Surfaces

The grain size surface for the Thiessen polygon is shown below (Figure 27). For the Thiessen polygon surface, the geometry is identical to the roughness maps, but the value assigned to each polygon is associated with a statistically derived grain size group. For grain size surface, there are four possible configurations of grain size representation: D_{16}, D_{50}, D_{84}, and grain size distribution (GSD). For the uniform grain size surface, the same grain size percentile or grain size distribution is applied over the entire surface. However, for the Thiessen polygon representation, a single grain size or GSD is applied to each corresponding polygon. Grain size percentiles and distributions are provided in Figure 28. The grain size percentiles and corresponding Manning's *n* values of the aggregate distribution are provided in Table 12.

Table 12. Results for aggregated grain size measurements

Number of Grains in Sample	Mean Grain Size (mm)	Standard Deviation (mm)	D_{16} (mm)	Manning's *n*	D_{50} (mm)	Manning's *n*	D_{85} (mm)	Manning's *n*
2140	**11.8**	**9.4**	**4.0**	**0.063**	**11.0**	**0.074**	**16.0**	**0.079**

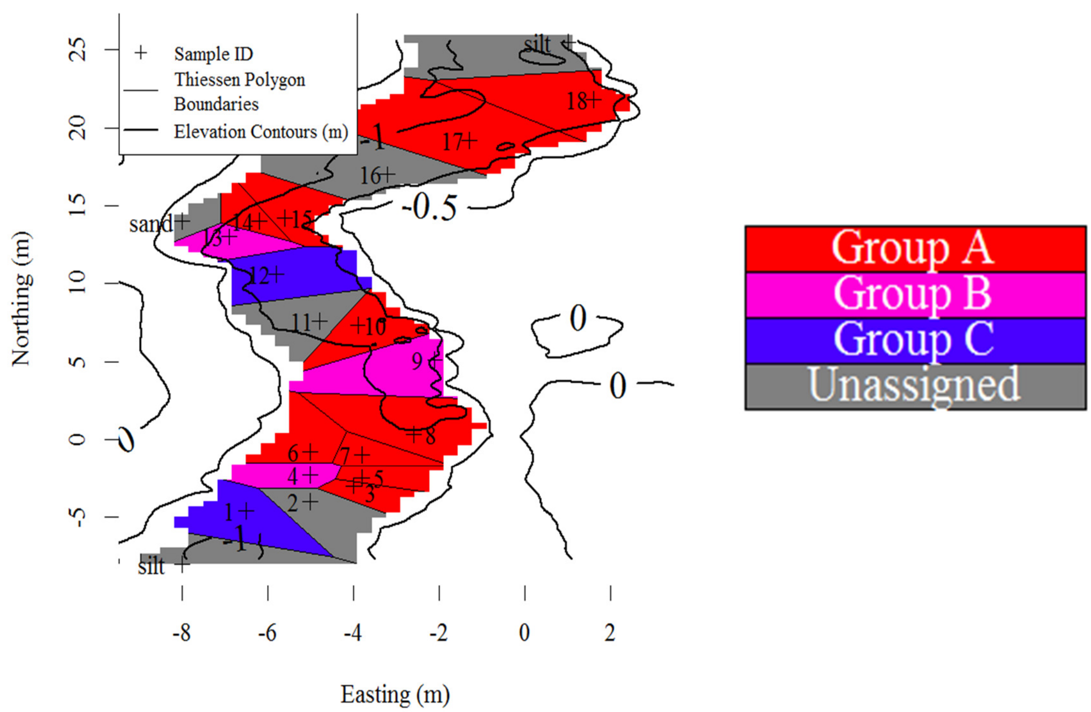

Figure 27. Grain size region groups for Thiessen polygon surface

Table 13. Group summary and corresponding grain size percentiles and Manning's *n* values

Statistical Test	Group	*p*- value	Arithmetic Mean (mm)	Arithmetic Standard Deviation (mm)	Geometric Mean	Geometric Standard Deviation	D_{16} (mm)	D_{50} (mm)	D_{84} (mm)	Manning's *n*
	A	0.174	13.7	8.9	10.9	2.1	5.6	11.0	22.6	0.0839
Kruskal-Wallis	B	0.153	9.4	6.4	6.7	2.6	2.0	8.0	16.0	0.0792
	C	0.410	6.8	12.9	3.1	3.1	1.0	2.8	11.0	0.0744

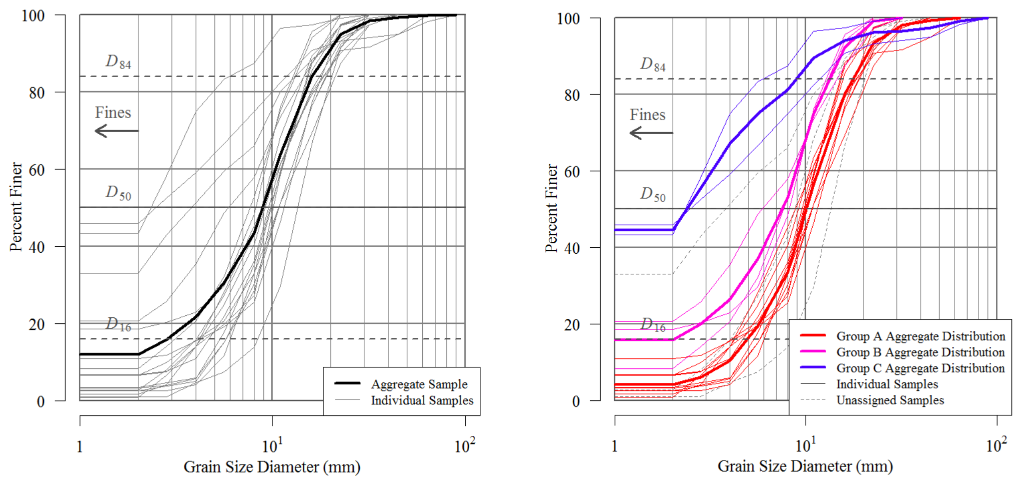

Figure 28. Grain size distributions used for uniform (left) and Thiessen polygon (right) grain size surface representations

4.5.3. Hydraulic Model Results

Results Legend

The following legend identifies the line types used to present data from different simulations. Color is used to distinguish the Manning's *n* roughness representation, and dash type indicates grain size representation. Legends will be associated with each figure, but these configurations will remain consistent throughout this chapter except where noted.

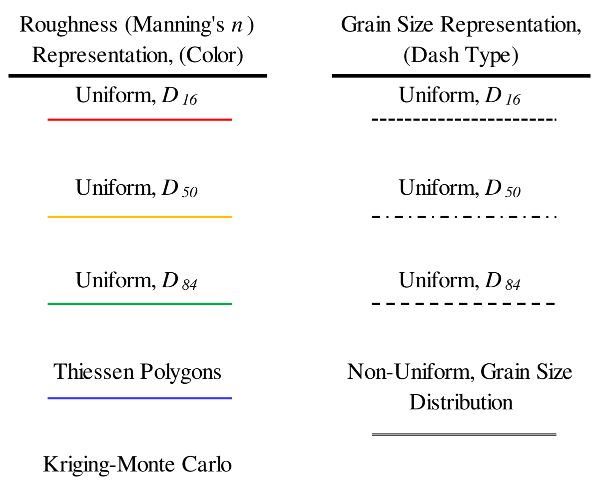

Figure 29. Results plotting legend

No Bedload Transport Scenarios

Variations of each surface type were first simulated *without* stream bed deformation to elucidate any differences that might be present solely due to roughness. Sensitivity to flow was also examined; flows of 1.5 m^3/s (two year return interval), and a low flow of 0.5 m^3/s were modeled.

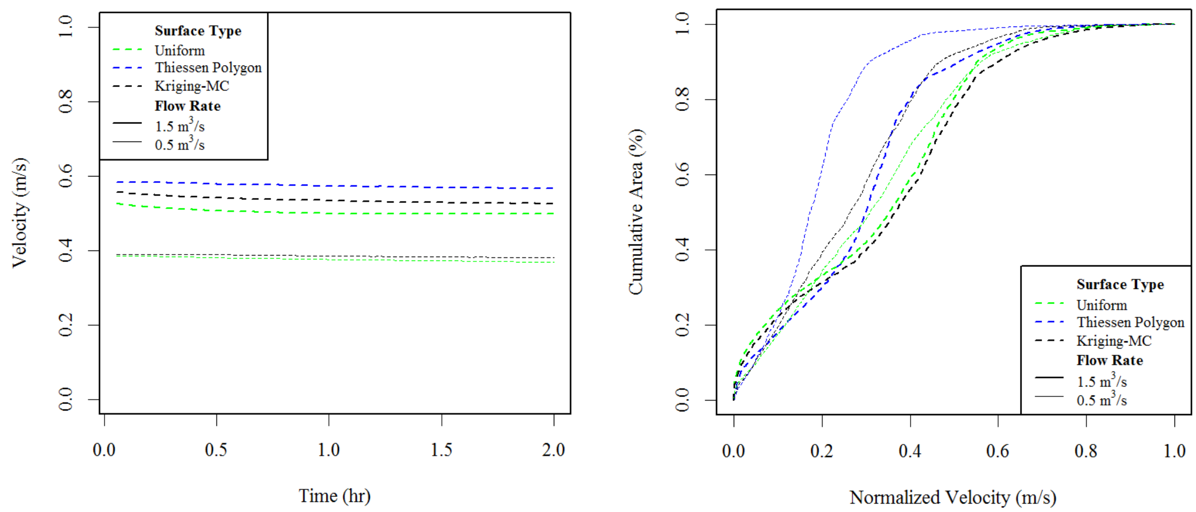

Figure 30. Time series (left) and Lorenz curves (right) of velocity for all surface types with varying flow rate

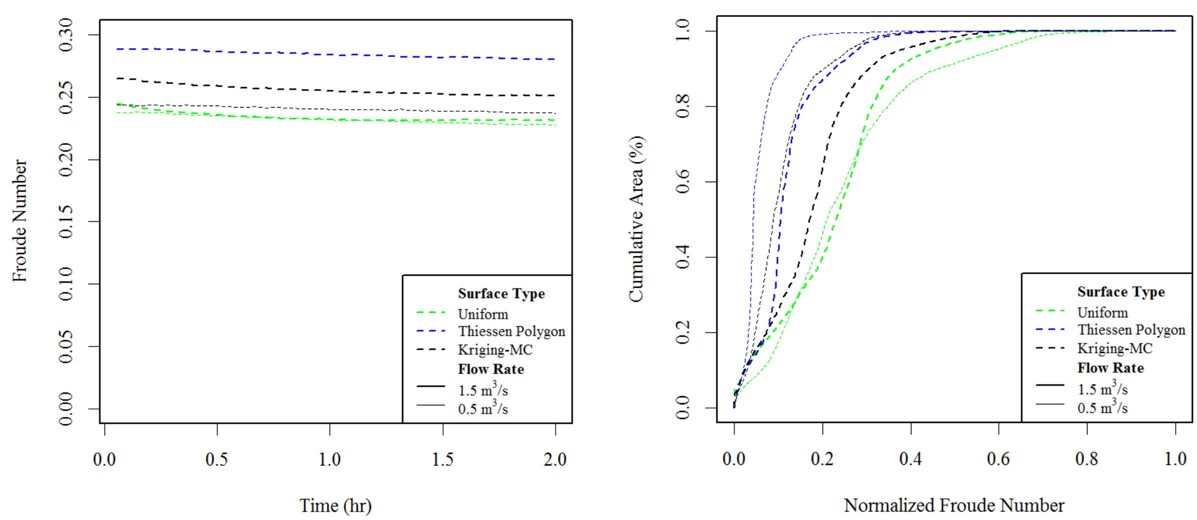

Figure 31. Time series (left) and Lorenz curves (right) of Froude number for all surface types with varying flow rate

Table 14. Summary of flow simulations without bedload transport.

Surface Type	Roughness	Grain Size	Flow Rate (m^3/s)	Average Parameter Values Depth (m)	Vorticity (1/s)	Froude Number	Velocity, Magnitude (m/s)
Uniform	D_{84}	D_{84}	0.5	0.287	-0.005	0.232	0.377
Kruskal-Wallis	D_{84}	D_{84}	0.5	0.293	-0.008	0.256	0.402
Kriging-MC	D_{84}	D_{84}	0.5	0.290	-0.007	0.241	0.386
Uniform	D_{84}	D_{84}	1.5	0.427	-0.003	0.234	0.504
Kruskal-Wallis	D_{84}	D_{84}	1.5	0.429	-0.004	0.284	0.574
Kriging-MC	D_{84}	D_{84}	1.5	0.424	-0.005	0.256	0.536

Bedload Transport Scenarios

Simulation results from scenarios conducted with bedload transport (i.e., bed deformation) are shown. Results for bedload, Shields parameter, aggradation, degradation, and mean bed material diameter are provided. Similar to the above section, results from a uniform surface are also provided. Multiple realizations of the kriging-Monte Carlo (kriging-MC) surfaces were generated for the D_{84} roughness, D_{84} grain size (uniform grain size) scenario. There are multiple lines associated with this simulation type to show the differences in hydraulic performance between Monte Carlo realizations of the same surface.

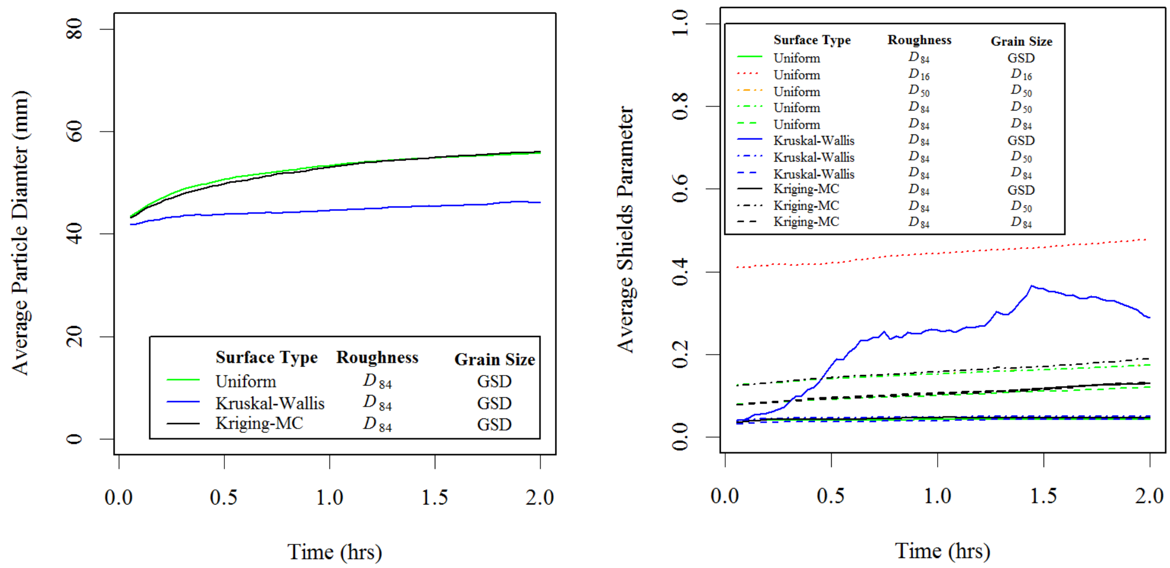

Figure 32. Time series for mean diameter of bed material (left) and average Shields parameter (right). Mean particle diameter data are only available for simulations with mixed size sediments (GSD representation)

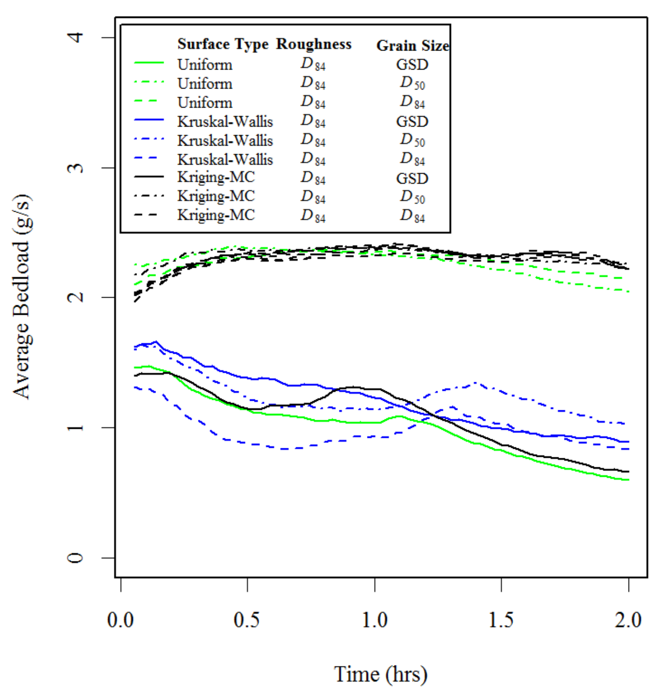

Figure 33. Time series of average bedload transport rate for simulations with bed deformation

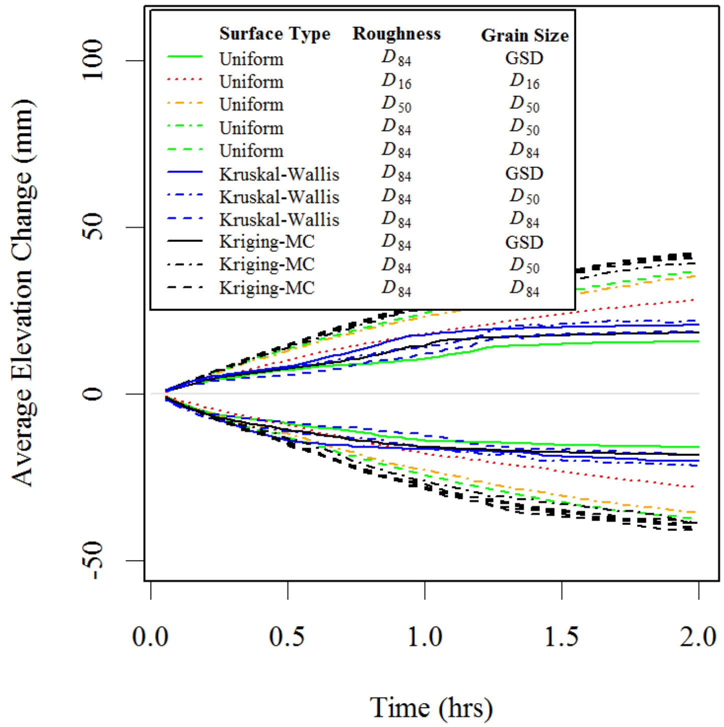

Figure 34. Average aggradation (+elevation change) and degradation (- elevation change) for simulations with bed deformation

Table 15. Summary of bedload transport scenario parameters. Parenthesis associated with kriging-MC surface types indicate realization number

			Average Parameter Values								
Surface Type	**Roughness**	**Grain Size**	**Depth (m)**	**Aggradation (mm)**	**Degradation (mm)**	**Vorticity (1/s)**	**Mean Diameter (mm)**	**Froude Number**	**Shields Parameter**	**Velocity Magnitude (m/s)**	**Total Bedload (kg)**
Uniform	D_{84}	GSD	0.409	10.69	-12.03	-0.0066	52.5	0.242	0.04	0.52	7.2
Kruskal-Wallis	D_{84}	GSD	0.409	14.73	-15.34	0.0012	44.5	0.293	0.24*	0.60	8.6
Kriging-MC	D_{84}	GSD	0.403	12.77	-13.97	0.0010	52.2	0.270	0.04	0.56	7.8
Uniform	D_{16}	D_{16}	0.416	17.11	-16.72	0.0071		0.239	0.44*	0.52	13.5
Uniform	D_{50}	D_{50}	0.412	21.48	-21.62	0.0027		0.230	0.15	0.50	16.3
Uniform	D_{84}	D_{50}	0.412	21.48	-21.60	0.0029		0.230	0.15	0.50	16.3
Kruskal-Wallis	D_{84}	D_{50}	0.411	14.29	-15.22	-0.0110		0.284	0.05	0.58	9.0
Kriging-MC	D_{84}	D_{50}	0.413	24.08	-23.71	0.0006		0.239	0.16	0.51	16.7
Uniform	D_{84}	D_{84}	0.410	22.48	-22.89	-0.0012		0.225	0.10	0.49	16.4
Kruskal-Wallis	D_{84}	D_{84}	0.412	11.86	-12.48	-0.0087		0.288	0.04	0.59	7.1
Kriging-MC (1)	D_{84}	D_{84}	0.412	25.09	-25.00	-0.0036		0.232	0.10	0.50	16.4
Kriging-MC (2)	D_{84}	D_{84}	0.411	24.98	-25.28	0.0003		0.234	0.10	0.50	16.5
Kriging-MC (3)	D_{84}	D_{84}	0.419	25.68	-26.07	-0.0048		0.238	0.11	0.51	16.7
Kriging-MC (4)	D_{84}	D_{84}	0.418	25.66	-25.76	-0.0067		0.236	0.11	0.51	16.7
Kriging-MC (5)	D_{84}	D_{84}	0.415	25.36	-25.45	-0.0009		0.237	0.11	0.51	16.6

*See note in *Uncertainty of Hydraulic Simulations* section on over-predicted Shields parameters

Sensitivity to Flow Rate

The Thiessen polygon surface representation was selected to explore the sensitivity to flow rate. Roughness and grain size were both represented by the D_{84} percentile, spatially distributed in Thiessen polygons. A cross-section of the resulting water surface elevations is shown in Figure 35. The slight slope in the water surface near the streambed boundary are caused by grid resolution. Water surface elevation in the 4.0 m^3/s flow extends above the floodplain and reaches the transverse boundary of the computational grid. The boundary condition for flow at the transverse extent of the grid is a no-slope, no-flow condition; flow is not allowed to leave the grid at the transverse boundary, and there is also no frictional contribution. For visual simplicity, some flow rates are not shown in figures, but are tabulated in Table 16.

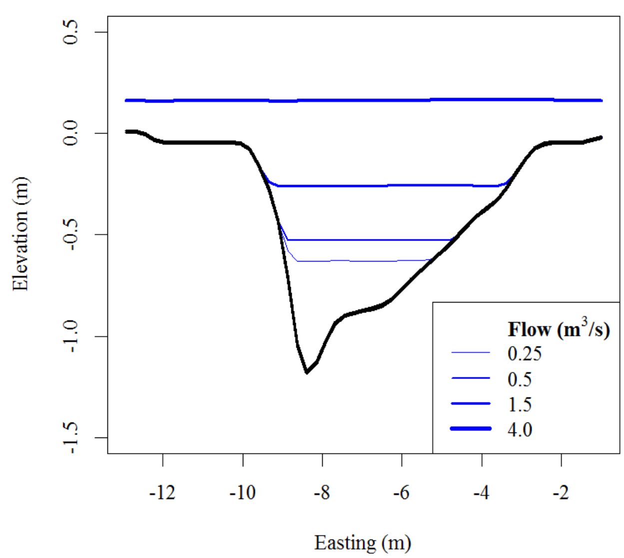

Figure 35. Cross-sections of water surface elevation at upstream boundary. Transverse slope of water surface near channel boundary is due to visualization error. Grid node spacing was insufficient to maintain a flat slope.

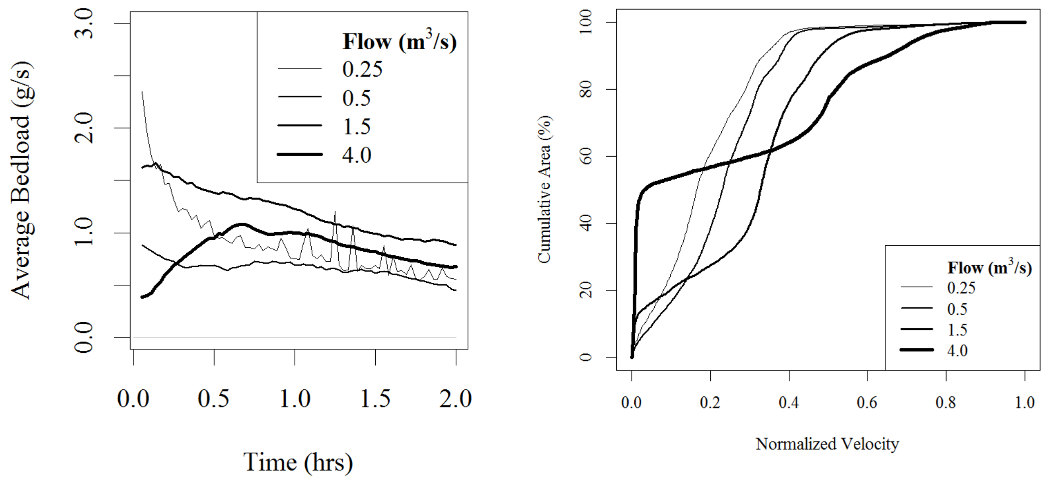

Figure 36. Time series of average bedload (left) and Lorenz curve of normalized velocity (right) for flow rate sensitivity scenarios

Table 16. Summary table for flow rate sensitivity scenarios

Surface Type	Roughness	Grain Size	Flow Rate (m^3/s)	Average Parameter Values								Total Bedload (kg)
				Depth (m)	Aggradation (mm)	Degradation (mm)	Vorticity (1/s)	Mean Diameter (mm)	Froude Number	Shields Parameter	Velocity Magnitude (m/s)	
Kruskal-Wallis	D_{84}	*GSD*	0.05	0.151	0.8	-1.2	-0.012	36.5	0.182	0.011	0.170	0.83
Kruskal-Wallis	D_{84}	*GSD*	0.1	0.176	1.2	-2.2	-0.008	37.1	0.213	0.018	0.233	2.01
Kruskal-Wallis	D_{84}	*GSD*	0.25	0.223	2.5	-3.5	-0.014	38.0	0.239	0.027	0.327	2.81
Kruskal-Wallis	D_{84}	*GSD*	0.5	0.278	5.4	-7.1	-0.023	39.5	0.280	0.044	0.436	4.72
Kruskal-Wallis	D_{84}	*GSD*	1.5	0.409	14.7	-15.3	0.001	44.5	0.293	0.239	0.596	8.65
Kruskal-Wallis	D_{84}	*GSD*	2.5	0.476	18.4	-16.4	-0.009	47.7	0.259	0.470	0.612	10.24
Kruskal-Wallis	D_{84}	*GSD*	3	0.492	18.3	-14.5	-0.025	51.6	0.233	0.445	0.580	9.57
Kruskal-Wallis	D_{84}	*GSD*	4	0.412	12.3	-9.6	-0.028	65.3	0.153	0.392	0.398	6.03
Kruskal-Wallis	D_{84}	*GSD*	5	0.480	11.4	-7.5	-0.037	68.6	0.127	0.352	0.358	4.91

*See note in *Uncertainty of Hydraulic Simulations* section on over-prediction of Shields parameter

Sensitivity to Grid Resolution

Conducting high resolution simulations with bedload transport calculations proved to be computationally intensive. So, the comparison between simulations occurred only during the first hour of the two year (1.5 m^3/s) flow. Differences in grid resolution are indicated by line type. The Thiessen polyon surface was used to spatially discretize the grain size and roughness.

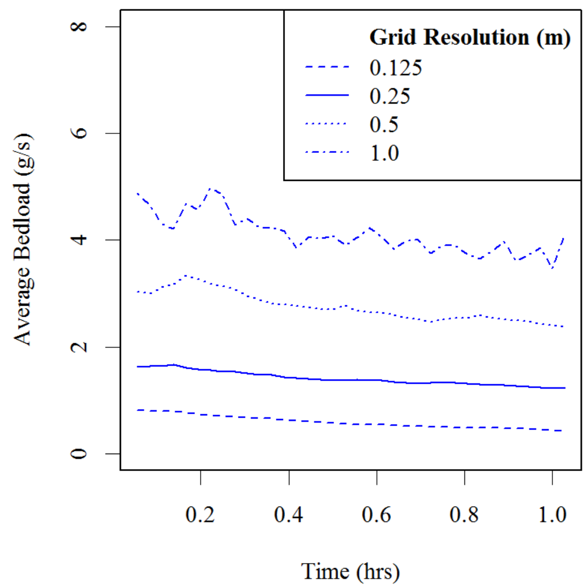

Figure 37. Time series of average bedload for grid resolution sensitivity analysis

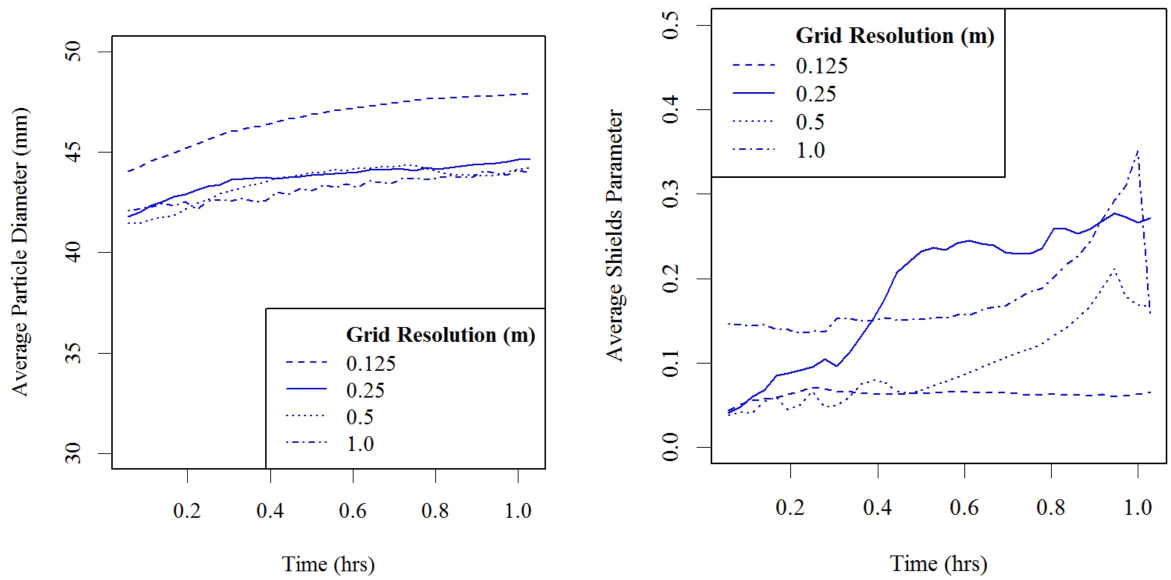

Figure 38. Time series of average particle diameter (left) and average Shields parameter

Table 17. Summary table for grid resolution sensitivity scenarios

Surface Type	Roughness	Grain Size	Grid Resolution (m)	Average Parameter Value: Depth (m)	Aggradation (mm)	Degradation (mm)	Vorticity (1/s)	Mean Diameter (mm)	Froude Number	Shields Parameter	Velocity Magnitude (m/s)	Total Bedload (kg)
Kruskal-Wallis	D_{84}	GSD	0.125	0.465	9.7	-9.4	-0.0057	46.9	0.238	0.064	0.53	4.0
Kruskal-Wallis	D_{84}	GSD	0.25	0.409	14.7	-15.3	0.0012	44.5	0.293	0.239	0.60	8.6
Kruskal-Wallis	D_{84}	GSD	0.5	0.389	11.9	-13.1	0.0065	44.1	0.301	0.172	0.59	16.7
Kruskal-Wallis	D_{84}	GSD	1.0	0.330	6.4	-6.6	0.0089	43.8	0.290	0.178	0.55	26.5

4.6. Discussion

The results of the model scenarios highlight the fundamental differences between surface types. Each surface was generated with a unique underlying statistical assumption; the surface is homogenous (uniform), the surface is discretized into patches (Thiessen polygon), or the surface is smoothed with small-scale heterogeneity (kriging-Monte Carlo). All of the models simulate the same stream, but achieve varying results depending upon the assumed surface heterogeneity.

4.6.1. No Bedload Transport Scenarios

The primary purpose of these scenarios was to observe any fundamental differences that might arise solely from variations in roughness representation in the hydraulic models. There are slight differences in the hydraulic performance of the three surfaces. The depths for all surfaces are almost identical for the same flows (Table 14). The times series of velocity indicates that the Thiessen polygon surface achieves an average velocity of approximately 0.07 m/s (14%) greater than the uniform surface, and 0.05 m/s greater than the kriging-MC surface (Figure 30). However, the more apparent trend is the increase in differences of velocity and Froude number with decreasing flow rate (Figure 30 and Figure 31). The Lorenz curves illustrate that the lower flows cause the distribution of velocities to shift towards relatively lower magnitudes. Decreasing the flow rate increased the spatial and temporal distribution of hydraulic parameters due to the influences of small scale differences in hydraulic roughness. The steepness of the Lorenz curves also indicates that a majority of the velocities are associated with one value, and higher velocities only occur in a few locations (a stepwise Lorenz curve would indicate that there was only one parameter value), (Figure 31). As the flow rate increases, the difference in magnitude of parameters increases with flow rate, whereas the differences in spatial and temporal distribution of parameters decreases. Some fish energetics models use a drag relationship to determine the energy usage of fish in a stream, and are sensitive to changes in velocity (Statzner and Sagnes, 2009). Therefore, roughness heterogeneity is an important factor when predicting biological impacts in a stream.

4.6.2. Bedload Transport Scenarios

By simulating bedload transport, the interdependent relationship between flow and form of the stream is explored. Fundamental differences between surface types are much more apparent than if only flow were simulated. An important result is that the predicted bedload transport is not constant throughout each simulation, even though the flow rate is fixed (Figure 33). As bed material is transported, the bed form is altered, which in turn induces a hydraulic response and changes the bedload transport rate. Eventually, the bedload reaches an equilibrium rate, established after approximately two hours.

Similar to the no bedload scenarios, there were no obvious differences in hydraulic performance between simulations. Depth, velocity, and Froude number remained nearly constant. Also, the Froude numbers were somewhat distinct between the roughness representations; the Froude numbers for the uniform, Kruskal-Wallis, and kriging-MC GSD representations were 0.242, 0.293, and 0.27, respectively.

When a mixed grain size was modeled (GSD representation), the predicted bedload transport rates between surface representations were most similar (Figure 33, solid lines). The Kruskal-Wallis surface tended to predict approximately half the total bedload transport of the other surfaces, except when the mixed size grain size was simulated (Table 15). Predictions of bedload from the Kruskal-Wallis surfaces were also more consistent between single grain size and mixed grain size representations (Figure 33, blue lines). Total bedload predictions from the Kruskal-Wallis surfaces varied between 7.1 and 9.0 kg, which is a much more consistent prediction than the uniform and kriging-MC simulations (Table 15). The average mean particle diameter varied between 44.5 mm predicted by the Kruskal-Wallis surface to approximately 52 mm, predicted by both the uniform and kriging-MC surfaces (Table 15). This difference of 8 mm in predicted grain size is a significant, considering that the simulations were only performed for two hours.

There were minimal differences between the kriging-MC realizations for the D_{84} grain size scenarios (Table 15). Total bedload transport predictions only varied by 0.3 kg. This finding indicates that the kriging error was not significant. All of the realizations produced similar hydraulic sediment transport predictions. Also, the uniform surface performed similarly to the kriging-MC simulations for all roughness and grain size representations (Table 15). Because both the uniform and kriging-MC scenarios had a spatially uniform grain size, this finding indicates that roughness differences alone is not sufficient to induce a significant difference in sediment transport.

4.6.3. Sensitivity to Flow Rate

Vorticity decreases with increasing flow, which is somewhat expected. Vorticity is the curl of the velocity vector, or tendency of the flow field to rotate. In a two-dimensional model, the vorticity is the rotational tendency of a vector perpendicular to the water surface, which would arise from channel elements like bends in the stream. Sign (+/-) of the vorticity simply indicates the direction of rotation, magnitude indicates the rotation rate. The velocity field compensates for the increased flow by establishing a greater longitudinal (downstream) velocity, decreasing the ratio of longitudinal to transverse velocity. As longitudinal velocity increases, rotational elements in the flow like eddies become less dominant in defining flow paths (streamlines).

Mean diameters for the flows exceeding 2.5 m^3/s were very large. Because the subsurface was not accurately characterized at the site, the model does not accurately reproduce high flow capable of scouring the armor layer and exposing the subsurface. In the two-dimensional model, shear stress is proportional to depth. This is most likely why the aggradation, degradation, and total bedload predicted by the 2.5 m^3/s flow simulation are greater in magnitude than the predictions of the 4.0 m^3/s flow (Table 16). An increased depth is required to accommodate the larger flow, but shear stress would not be expected to decrease. The 4.0 m^3/s flow is expected to be able to transport more bedload, not less. Predictions for flows above bankfull discharge (2.5 m^3/s) are likely inaccurate for multiple reasons: 1) insufficient data were collected to characterize the floodplain roughness and elevation, 2) the floodplain is covered in vegetation; Nasy2DH has a simplistic relation for flow drag imposed by vegetation, and 3) floodplain flow has three-dimensional properties that cannot be captured by a two-dimensional solver.

4.6.4. Sensitivity to Grid Resolution

As grid cell size increased, the average depth decreased, but the average Froude number and total bedload transport increased (Table 17). The differences in bedload transport rates between the simulations highlight the importance of careful selection of grid resolution (Figure 36, Table 17). Bedload transport increased almost linearly with grid resolution. As grid cell size becomes too large or small, the physical interpretation diminishes. At Cat Spur Creek, a grid cell of 1.0 m^2 would need to accurately represent the effect that hundreds of bed particles have on flow and sediment transport. The 0.5 m and 1.0 m resolution grids are most likely too coarse to produce accurate measurements. Channel width is only two meters at some cross-sections, and there would not be enough nodes to properly represent the flow. The most appropriate grid resolution is likely dependent upon the heterogeneity of the surface and particle size of the stream bed.

4.6.5. Uncertainty of Hydraulic Simulations

For some areas along Cat Spur Creek, the simulated Shields parameter values were extremely high (~300). These areas of high shear were due to improper representation of the bank morphology at the site. As described previously, bank collapse is the main process promoting channel mobility in Cat Spur Creek. This occurs suddenly in banks that are severely undercut, and Nays2DH is not able to simulate the process. Instead, Nays2DH simulated banks with very high transverse slopes. Because Shields parameter is proportionate to the square root of the surface slope, Shields parameter and transverse bedload transport were over-predicted in the grid cells with steep banks (Figure 39). However, this problem was corrected by excluding the Shields parameter and transverse bedload transport in these cells from inclusion in the overall results.

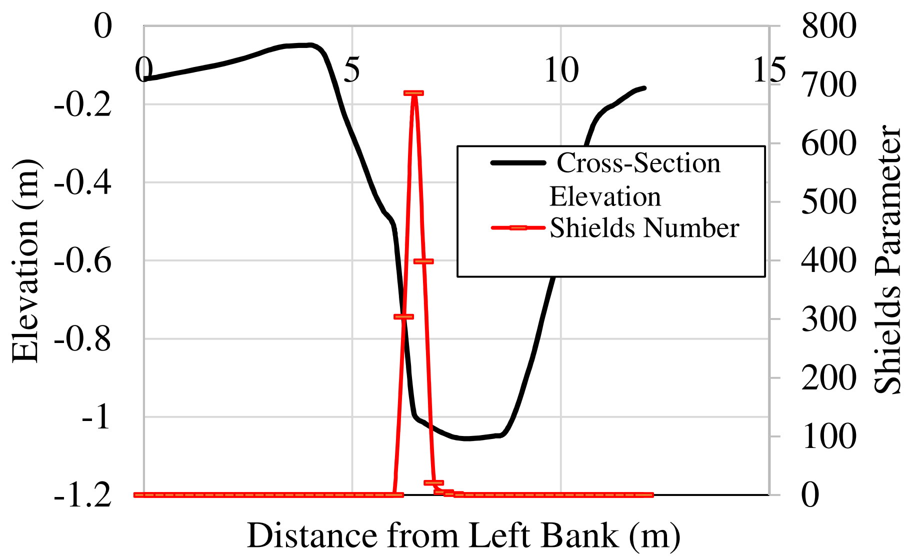

Figure 39. Over-prediction of Shields parameter at grid cells with steep banks

4.7. Conclusions

Results of the hydraulic models that simulated a non-deformable bed explored the effects of roughness heterogeneity, which affects flow predictions. There were large differences observed in velocity predictions (14%), but not depth. Therefore, roughness heterogeneity (which is a product of grain size heterogeneity in gravel bed streams), is an important consideration when predicting biological impacts. Fish energetics models are particularly sensitive to velocity (Statzner and Sagnes, 2009). As the flow rate is increased, average differences in uniform and heterogeneous simulations become more apparent. At low flow rates, roughness variations become more influential on the spatial distribution of velocity. Sediment transport predictions are more sensitive to grain size than to roughness differences. Mean bed particle diameter and total bedload transport are sensitive to the grain size representation. Total bedload transport predictions can vary by 100% between a heterogeneous and uniform grain size representation. Implications for these conclusion depend upon the intended purpose of the hydraulic model. The following conclusions about specific scenarios are also made:

- Discharges greater than bankfull were susceptible to model inaccuracies such as improper floodplain characterization, vegetation, and misrepresentation of three dimensional flow.
    - As demonstrated by the high flow scenarios, vegetation plays a large role in channel morphology. Because current hydraulic models have simplistic approaches to simulating vegetative effects on flow, predictions for high flow or long extended periods of time are inaccurate.
- When using a uniform grain size, the spatially uniform representations of grain size predicted twice the total bedload as a heterogeneous surface. However, when using a mixed size sediment (GSD) representation, sediment transport predictions show less variance between surface types.
- The Kruskal-Wallis (Thiessen polygon) surface, which was the only surface to use a heterogeneous grain size representation, produced the most consistent sediment transport predictions: 7.1 to 9.0 kg.
    - Total bedload transport predictions resulting from the uniform and kriging-MC surfaces varied from 7.2 kg to 18.7 kg
- Differences in sediment transport predictions between kriging-Monte Carlo realizations was minimal, indicating that standard error in kriging predictions of hydraulic roughness was not large enough to affect sediment transport predictions.

CHAPTER 5: HILLSLOPE AND STREAM IMPACTS OF RESIDUAL BIOMASS REMOVAL IN A HARVESTED WATERSHED

5.1. Introduction

The Northwest Advanced Renewables Alliance (NARA) project is assessing the possibility of converting residual woody biomass (i.e., slash, branches or fallen trees) remaining after a timber harvest into bio-jet fuel. The purpose of the NARA project is to provide a sustainable source of jet fuel in the Pacific Northwest. Sustainability of the soil, streams, and other environmental conditions are essential to NARA project feasibility. The proposed procedure has been developed to predict the impacts of residual woody biomass removal to sediment transport in streams of the Pacific Northwest. No implications are made for the actual feasibility of the NARA project with respect to environmental sustainability. The purpose of the analysis is to provide a methodology, and a basin-specific example of the predictions that can be made with the methodology. Portions of this methodology may be improved in the future to provide more accurate estimates of hillslope and stream response. Tools used to make the predictions are free and publicly available, so the analysis may be easily repeated.

5.2. Methodology

Due to the inherent difficulty in predicting hillslope erosion and sediment transport, a very general methodology was developed to account for the expected error in calculations. Typical hillslope and stream properties that influence erosion and sediment transport rates are shown below.

Table 18. Physical and biological variables controlling erosion and sediment transport in a watershed

Physical	Biological
Slope	Vegetation type
Soil depth	Age of forest
Antecedent moisture conditions	Canopy (leaf area index)
Presence and quality of roads	Burrow holes of ground-dwelling organisms
Soil porosity	
Geology	
Method of harvest	
Climatic variability	
Presence of rock or bare surfaces	
Location of disturbance on hillslope	
Additional watershed activities and their timing	
Presence of a buffer strip	
Wood on hillslope and in channel	
Grain size of stream sediment	

Accounting for each of these properties for a set of basins would require an exhaustive effort. Instead, an approach is used that accounts for some of the physical properties of a basin such as slope, vegetation, percent cover, presence of rock, and soil type. The remaining factors are assumed to be accounted for by preset conditions established in the hillslope model. The model used to predict hillslope response to timber harvesting and the subsequent NARA project is the Forest Service Disturbed version of the Watershed Erosion Prediction Project (FS WEPP) online interface, which is an abridged version of WEPP. The model used to predict the stream response is Nays2DH, a two-dimensional solver capable of simulating flow, sediment transport, and bed deformation.

There have been sufficient forest hydrology studies to demonstrate that quantitatively extrapolating timber harvesting impacts from one watershed to another is not possible (Bathurst and Iroume, 2014; Dunne, 2001). Thus, site-specific analyses, conducted with knowledge of important variables controlling watershed response, will likely prove to be a more useful approach. There is a large amount of uncertainty in predicting the sediment yield from a hillslope. Due to the stochastic nature of precipitation-runoff-sediment relationships, a range of possible responses is more appropriate than individual values. FS WEPP has an accuracy of ±50% with respect to erosion, runoff, and sediment yield predictions (Elliot and David, 2010). This analysis predicts the response of a stream to a single storm event using percent changes predicted by the FS WEPP model. The predictions of sediment yield increase from the FS WEPP hillslopes model are then used as input to the Nays2DH stream model.

5.2.1. Site Selection and Data Acquisition

The first component of the analysis is to find a site with desirable features. With respect to the NARA project, it is advantageous to select a watershed with historical logging and previously collected data, particularly data relating to sediment transport. Cat Spur Creek, ID was selected as the optimal watershed (Figure **40**). Data were previously collected by the Boise Adjudication Team (BAT) between 1988 and 1996 (BAT, 2014). Additionally, geospatial information of forest activity data were available from the Forest Service beginning in 1913 (FS, 2014). Public domain Digital Elevation Models (DEMs) were available for download at multiple resolutions.

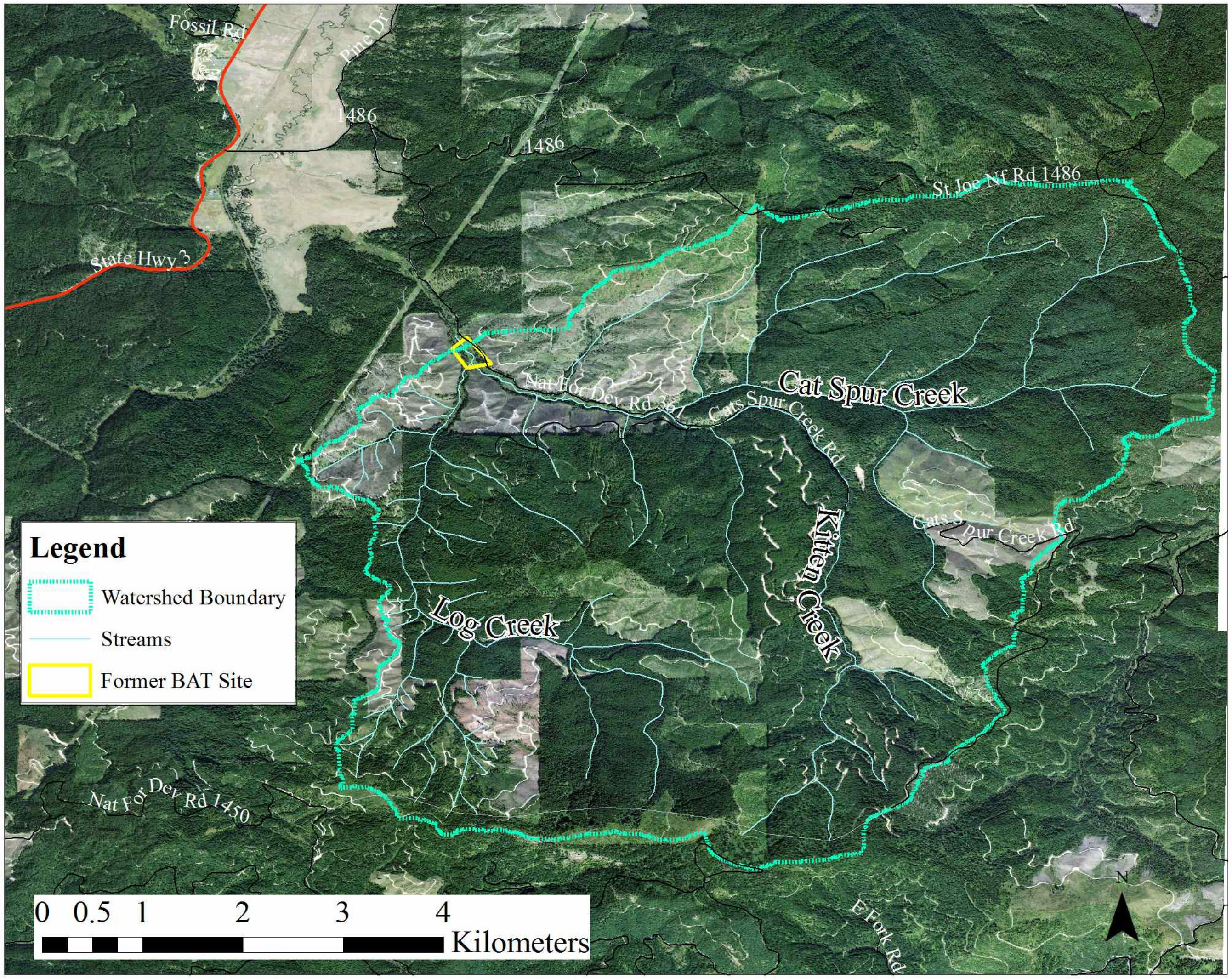

Figure 40**.** Cat Spur Creek watershed and former BAT site. Reach used in this study is located at former BAT site shown in figure.

Climate data were obtained from the National Climate Data Center from a weather station in Clarkia, ID located approximately two miles north of the Cat Spur Creek watershed (NCDC, 2014). The data was aggregated into monthly intervals, the format required by FS WEPP (Figure 41).

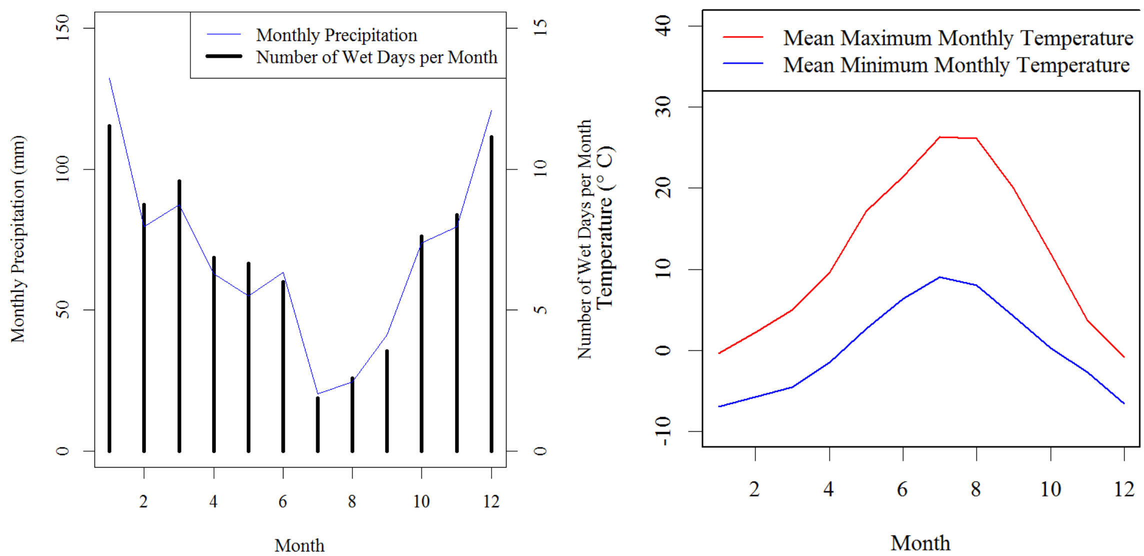

Figure 41. Monthly precipitation and number of wet days (left), and monthly temperature extremes (right) for Clarkia, ID

5.2.2. Hillslope Delineation and Characterization

FS WEPP requires physical measurements for all hillslopes in a basin. Instead of characterizing every hillslope in the Cat Spur Creek watershed, representative hillslopes were selected to determine the response for larger basins (Figure 42, Figure 43).

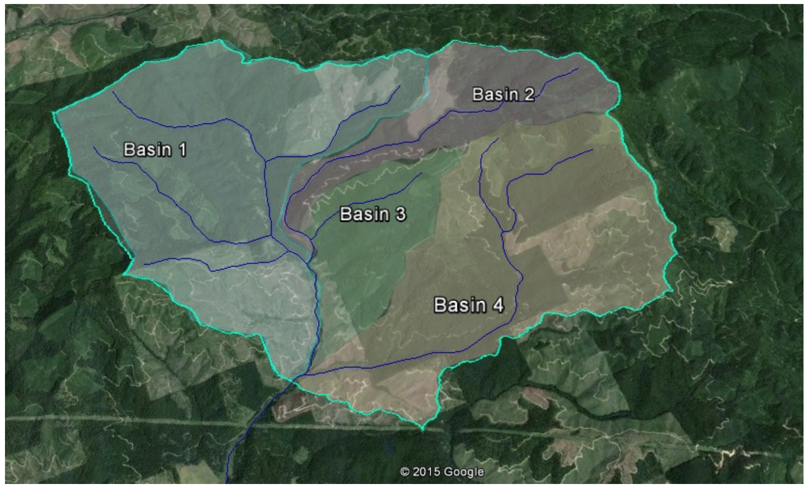

Figure 42. Basin delineation in Cat Spur Creek watershed

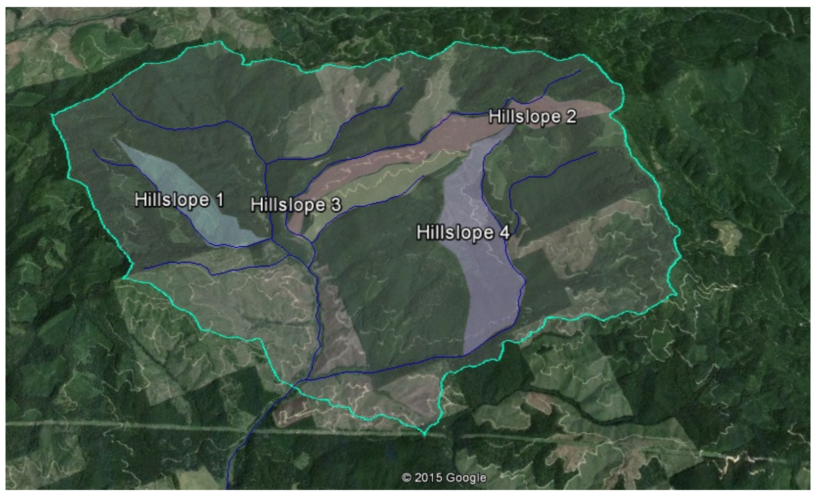

Figure 43. Selected representative hillslopes in Cat Spur Creek watershed

The following tabulated data corresponds to the hillslopes shown in Figure 43. Topographic analysis was conducted in ArcGIS to determine the appropriate slopes and hillslope lengths. Each hillslope is assumed to be representative of the corresponding basin.

Table 19. Hillslope conditions for FS WEPP analysis

						Upper Hillslope			Lower Hillslope		
Hillslope Label	Hillslope Area (km^2)	Corresponding Basin Area (km^2)	Top Elevation (ft)	Middle Elevation (ft)	Bottom Elevation (ft)	Top Hillslope Length (ft)	Top Slope (%)	Bottom Slope (%)	Bottom Hillslope Length (ft)	Top Slope (%)	Bottom Slope (%)
1	0.7	11.8	3720	3570	3490	760	0%	20	500	16	5
2	1.5	4.4	4170	4000	3840	880	0%	19	915	17	5
3	0.7	3.0	3890	3766	3640	830	0%	15	580	22	5
4	1.6	8.9	4200	3830	3680	1570	0%	24	860	17	5
	Total	**28.2**									

There are numerous soil types in the Cat Spur Creek watershed, but all correspond to the silt loam classification in FS WEPP (NRCS, 2012).

5.2.3. FS WEPP Prediction of Erosion and Sediment Yield

Erosion and sediment yield predictions were made with FS WEPP. The model has a simple online interface that accounts for climate, soil type, vegetation, slope, hillslope length, percent cover, and percent rock (Figure 44). The FS WEPP model has an accuracy of approximately ±50% with respect to runoff and erosion predictions (Elliot et al., 2000). For the desired years of simulation, FS WEPP creates stochastic climates and calculates the return interval rates for runoff, erosion, and sediment yield.

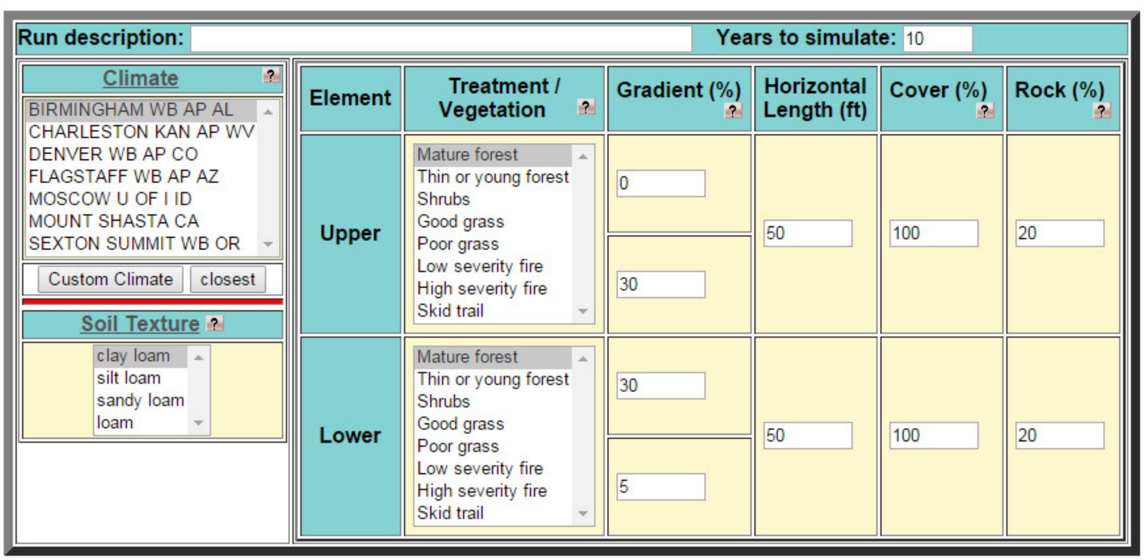

Figure 44. Example FS WEPP interface (Elliot and David, 2010)

The primary assumption of this analysis is that the impacts of biomass removal will be proportional to the area disturbed. Although there has been some recent evidence to suggest that the sediment yield is not correlated to area of disturbance, this may be a product of site-specific factors (Bathurst and Iroume, 2014). A disturbance in one basin will produce a different sediment yield than the same disturbance in another basin. However, the same disturbance on the same hillslope would be expected to produce a similar response. It is assumed that physical and climatic parameters used in FS WEPP are sufficient enough to predict erosion and sediment yield.

The FS WEPP model uses the steady-state WEPP erosion model to derive the annual erosion yields (Foster et al., 1995):

$$\frac{dG}{dx} = D_f + D_i \tag{5.1}$$

where,

G	= sediment load $\left(\frac{kg}{s\cdot m}\right)$
x	= distance downslope (m)
D_i	= interill sediment delivery to rill $\left(\frac{kg}{s\cdot m^2}\right)$
D_f	= rill erosion $\left(\frac{kg}{s\cdot m^2}\right)$

G is solved on a horizontal unit of rill width basis (i.e., perpendicular to elevation contours). Further methodology for describing the WEPP erosion model is provided in Foster et al. (1995). It should be noted that FS WEPP does not provide information on landslides or mass movement events in the watershed. In FS WEPP, solutions to Equation 5.1 have been calibrated for all possible combinations of soil type and vegetation (4 soil and 8 vegetation types), so the database contains 32 sets of conditions, which are then corrected for the assigned hillslope conditions.

There are eight possible pre-defined vegetation treatment options built into the interface. Altering the vegetation changes the following physical properties (Elliot and David, 2010):

- Plant height, spacing, leaf area index and root depth

- Percent of live biomass remaining after vegetation
- Soil rill and interrill erodibility and hydraulic conductivity
- Default radiation energy to biomass conversion ratio

FS WEPP is very sensitive to vegetative cover. Variances within each of the eight vegetation conditions are possible by altering the cover. There are many ways to harvest lumber from a forest, from less invasive helicopter logging to clearcutting. These different harvesting methods produce different post-harvest conditions. However, FS WEPP does not have conditions set for each harvesting methodology. It is assumed that the variables for cover and treatment encompass both harvest method and age post-harvest. The conditions to replicate the associated scenarios are given in Table 18.

Table 20. Parameter values for initializing FS WEPP scenarios

Scenario	Cover Type	Cover (%)	Rock (%)	Soil Type
Baseline (natural conditions)	Mature Forest	100	0	Silt Loam
Timber Harvest	Thin Forest	100	0	Silt Loam
Biomass Removal (5% basin area)	Thin Forest	95	0	Silt Loam
Biomass Removal (10% basin area)	Thin Forest	90	0	Silt Loam

5.2.4. Hydraulic Model Predictions of Bedload Transport

A hydraulic model has been developed for a small reach (40 m) at the outlet of the Cat Spur Creek watershed. Nays2DH software was used, which is a two dimensional solver capable of predicting flow and bedload transport. Due to model limitations, hydraulic simulations will only be conducted using the two year return interval flood (1.5 m^3/s). Simulations with large sediment supply rates over long periods of time are very computationally intensive. Also, bankfull discharges and greater produced highly unstable simulation results when attempting to model increased sediment supply, and were excluded from simulation.

Instead of directly simulating the influences of increased runoff provided by FS WEPP, hydraulic models are initialized with varying sediment input. Stream impacts from increased sediment yield will be observed by the sensitivity of the Nays2DH model to sediment supply. The percent of equilibrium sediment supply setting is used to adjust the upstream sediment supply in Nays2DH (Shimizu et al., 2014). The percent sediment equilibrium setting uses the downstream input as the upstream input, and allows for variations within the percent change of sediment supply. Sediment increases will be observed ranging from 100% equilibrium condition to 160%.

5.2.5. Combining FS WEPP and Hydraulic Model Predictions

FS WEPP was not developed to make predictions for disturbances like those anticipated from biomass removal following harvesting. To relate FS WEPP predictions to biomass removal impacts, the following assumptions are made:

- Biomass removal impacts are proportionate to the area of disturbance
- Biomass removal impacts are equivalent to traditional timber harvesting impacts of the same area
- Sediment yield in FS WEPP is equivalent to sediment supply in Nays2DH
- Current conditions at Cat Spur Creek represent a harvested watershed

Biomass removal will likely disturb a small area of land relative to the initial timber harvest. The assumption that impacts will be as intensive as traditional harvesting practices will provide a conservative estimate. All sediment yield predicted by FS WEPP is finer than 0.3 mm in diameter (Elliot and David, 2010). A limitation of the Nays2DH model is that the user is not able to control grain size fractions of sediment input to the model. It is assumed, therefore, that sediment yield increases from FS WEPP correspond to sediment supply increases in Nays2DH. This assumption is based on the premise that the bedload transport at Cat Spur Creek is comprised of finer particles, which is supported by field data collected from the site. BAT bedload transport measurements indicate that approximately 80% of bedload transport is comprised of particles finer than 2 mm in diameter (BAT, 2014). By using a large flow, it is also assumed that bedload transport rate of particles 0.3 mm in diameter (FS WEPP input) will be equal to bedload transport of particles 2 mm in diameter (BAT data finding). Another key assumption is that current conditions at Cat Spur Creek represent are representative of a logged watershed. Thus, sediment supply impacts are predicted using sediment yield changes relative to the timber harvest scenarios.

5.2.6. Sensitivity Analysis

The following parameters in the FS WEPP model will be tested for sensitivity:

- Climate: Clarkia, ID (2015 climate)*, Clarkia, ID (2050 climate)
- Vegetative cover: 100%*, 95%, 90%

*Indicates baseline parameter used for Cat Spur Creek analysis.

The sensitivity of these parameters will be observed using physical measurements from Hillslope 1 in the Cat Spur Creek watershed. The primary variable of concern in this analysis is sediment yield. To simplify interpretation of results, the sensitivity of the FS WEPP output will be observed only with respect to sediment yield. To approximate the 2050 climate at Clarkia, ID, average monthly temperature and precipitation of an ensemble of global climate models are used (Nature Conservancy, 2009).

5.3. Results

Results are shown for the data processing required to determine the flow rate return intervals. Predictions from the FS WEPP hillslope model and Nays2DH hydraulic model are also provided.

5.3.1. Analysis of Previously Collected Data

The data gathered from both the U.S. Forest Service and the BAT were combined to observe any trends in sediment transport and forest activity (Figure 45).

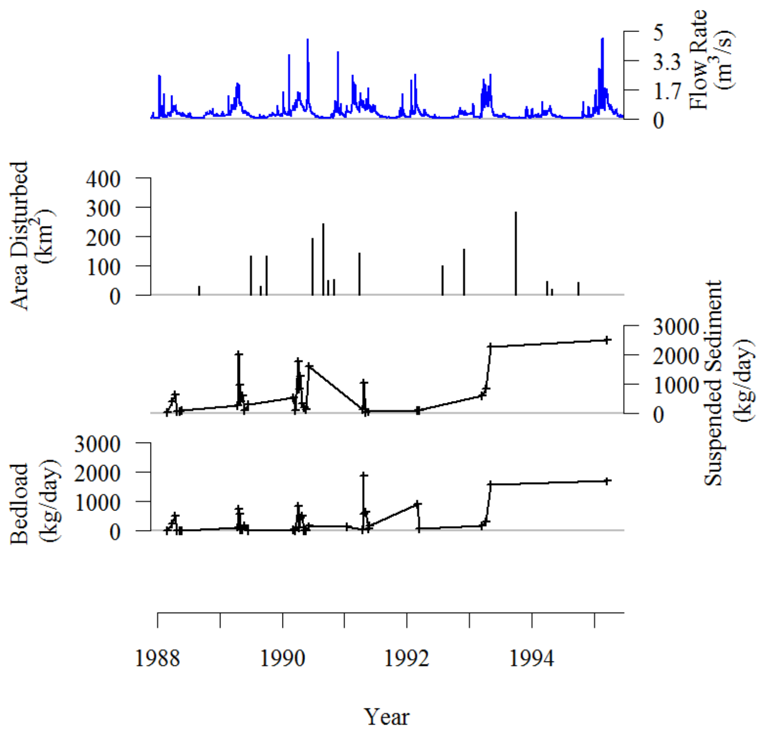

Figure 45. Compiled data from Forest Service and BAT sources (USDA FS, 2014; BAT, 2014)

U.S. Geological Survey gauge data was available for the St. Maries River; Cat Spur Creek is a tributary of the St. Maries River. Gauge data was available for the St. Maries River from 1965 to 2015 at a gauge located approximately 20 miles from the Cat Spur Creek watershed. Correlation of the two data sets is shown (Figure 46).

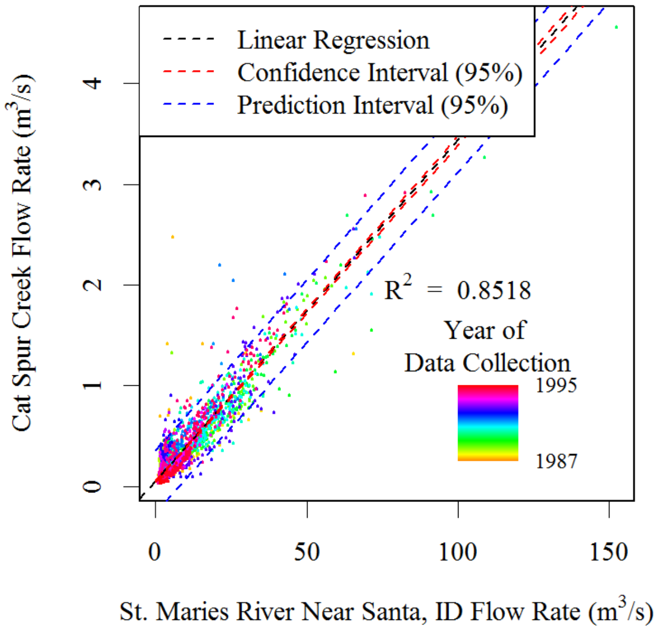

Figure 46. Correlation of gauge data collected from Cat Spur Creek and St. Maries River near Santa, ID between 1988 and 1995

Using the regression performed on the St. Maries River data, flow rate in Cat Spur Creek was extrapolated between 1965 and 1988, and 1995 to 2015. Using the extended data set, return intervals were derived (Figure 46).

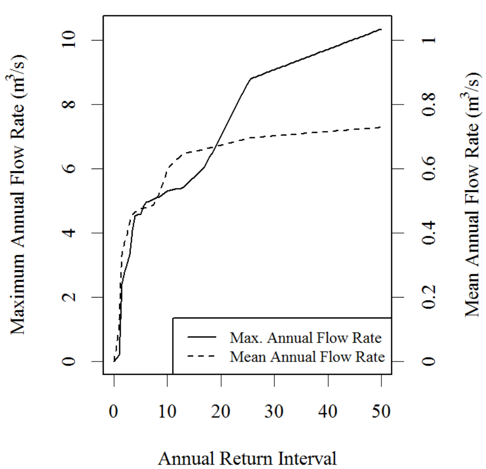

Figure 47. Return interval calculations for Cat Spur Creek using extrapolated flow data (1965 - 1988, 1995 - 2015)

5.3.2. Model Predictions

Predictions of hillslope sediment yield changes are shown below in addition to sediment yields calculated using the 2050 climate approximation (Figure 48). The predicted changes in sediment yield from timber harvest and subsequent biomass removal are provided in Table 21. Sediment yield impacts predicted by the Nays2DH hydraulic model are shown in Figure 49 and tabulated in Table 22.

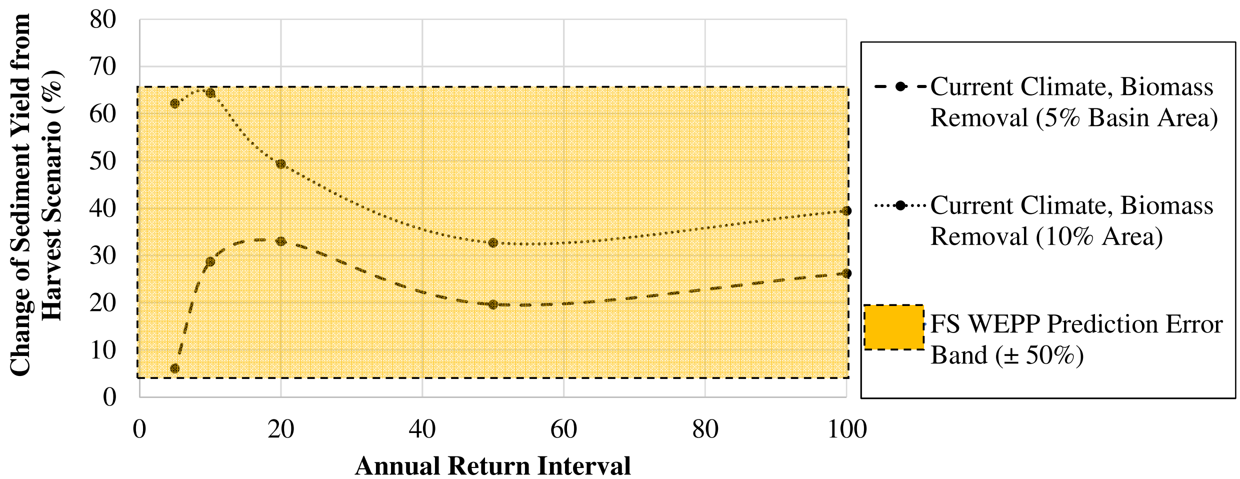

Figure 48. FS WEPP predictions for average annual sediment yield. Annual return intervals correspond to mean annual flow rate. Orange band brackets error in estimate

Table 21. Summary of NARA project impacts to sediment yield

Scenario:	Baseline	Harvest	Biomass Removal (5% of Basin Area)		Biomass Removal (10% of Basin Area)	
Annual Return Interval	Sediment Yield (Mg/yr)	Sediment Yield (Mg/yr)	Sediment Increase from Baseline (%)	Sediment Increase from Harvest (%)	Percent Increase (%)	Sediment Increase from Harvest (%)
100	987	2200	181%	26%	211%	39%
50	698	871	49%	20%	66%	33%
20	181	247	81%	33%	104%	49%
10	130	155	53%	29%	96%	64%
5	56	44	-16%	6%	29%	62%

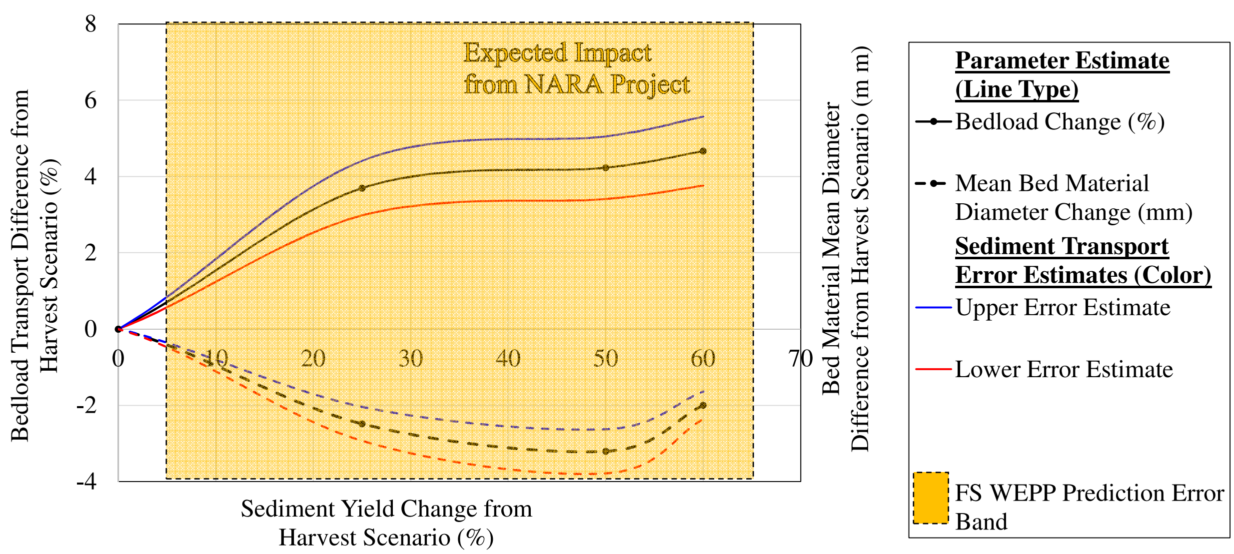

Figure 49. Bedload transport rate and mean bed material diameter predictions from Nays2DH with varying sediment supply. Orange box shown brackets error in estimate produced by FS WEPP; also present in Figure 48

Table 22. Summary of sediment transport model response to increased sediment supply

Sediment Supply Increase (%)	Average Parameter Values				Total Bedload (kg)	Bedload Transport Difference from Harvest Scenario (%)
	Aggradation (mm)	Degradation (mm)	Mean Bed Particle Diameter (mm)	Mean Bed Diameter Difference from Harvest Scenario (mm)		
-25	10.2	-12.6	41.8	0.82	10.06	-2.43
0	10.1	-12.4	40.9	0.00	10.31	0.00
25	10.1	-12.0	38.4	-2.49	10.69	3.69
50	9.8	-11.7	37.7	-3.21	10.75	4.23
60	10.2	-12.0	38.3	-2	10.79	4.67

2.3.3. Climate Change Analysis

Using ClimateWizard, the 2050 temperatures and precipitations were predicted (Nature Conservancy, 2009), (Figure 50, Figure 51). The climate data was then used to initialize FS WEPP using physical measurements made from Hillslope 1 in the Cat Spur Creek watershed (Figure 52).

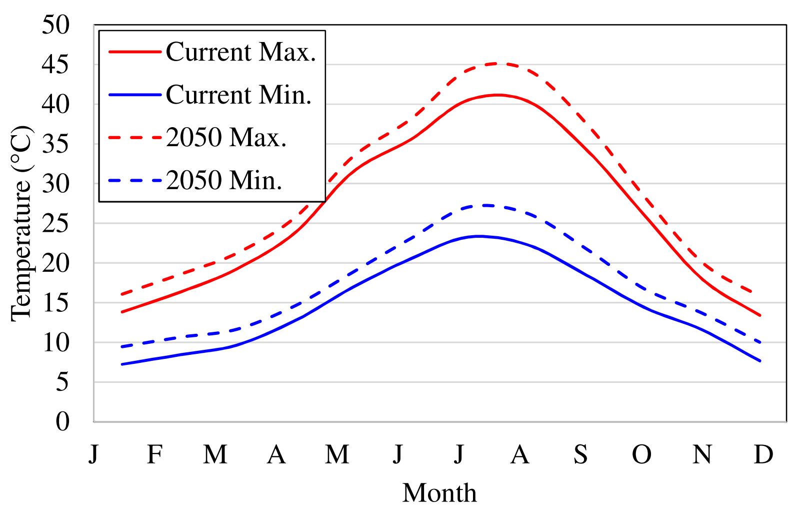

Figure 50. Mean maximum and mean minimum monthly temperature for current and 2050 climate (Nature Conservancy, 2009)

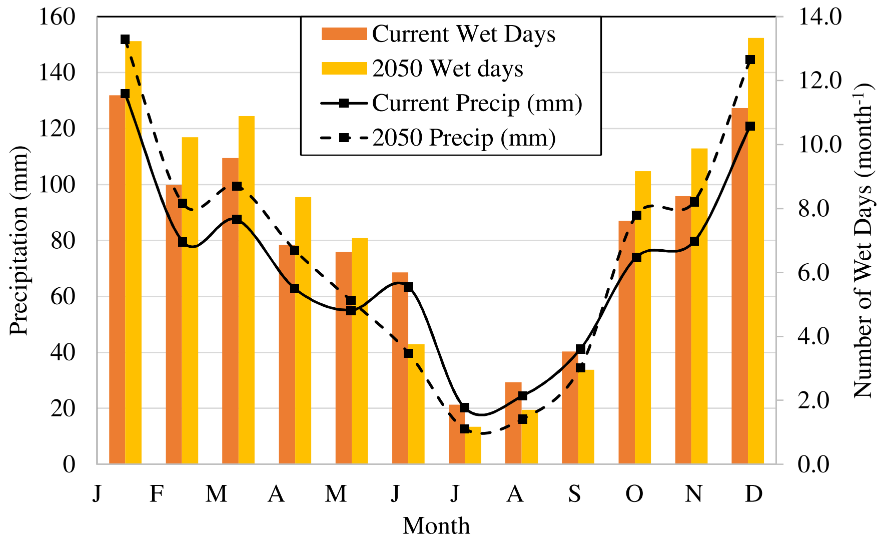

Figure 51. Monthly precipitation for current and 2050 climate (Nature Conservancy, 2009)

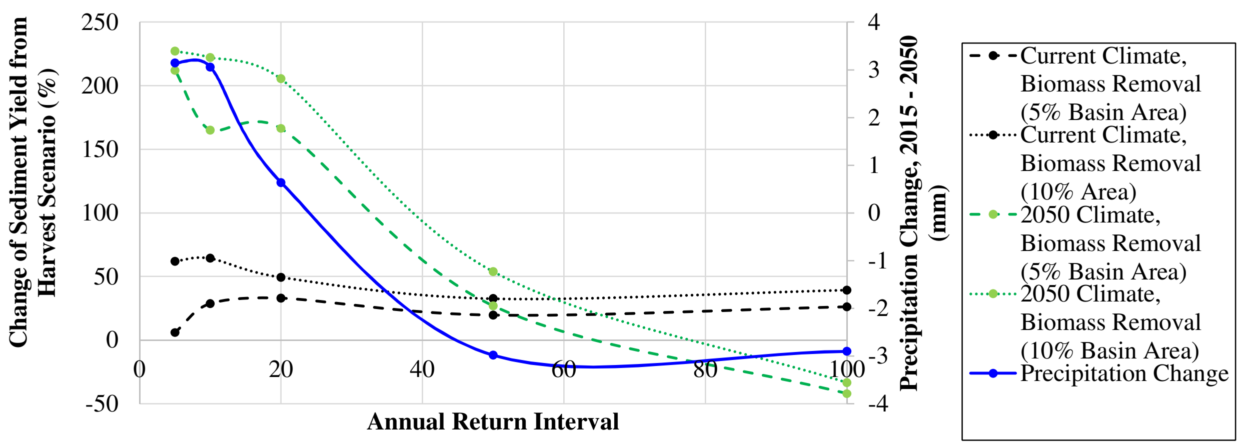

Figure 52. Climate change impacts to sediment yield. All percentages are relative to the sediment yield predicted for a timber harvest conducted in the current climate. Precipitation changes are shown for comparison

5.4. Discussion

FS WEPP predictions show that sediment yield of the hillslope will increase by 6 to 65% as a result of biomass removal (Figure 48). These values reflect biomass removal disturbances that are in addition to the initial timber harvest in the watershed. From the Nays2DH predictions, increases of 6 to 65% in sediment supply correspond to an approximate 1 to 6% increase in bedload transport for a two year return interval flow. Mean bed particle diameter is predicted to decrease by up to 4 mm (Table 22). These predictions are approximations that provide a general description of biomass removal impacts; the FS WEPP model has a stated accuracy of ±50% (Elliot and David, 2010). The physical and biological consequences of these changes to sediment yield, bedload transport and bed material diameter are unknown. Further interpretation would require an ecological assessment of Cat Spur Creek. Salmon habitat is particularly sensitive to changes in bed material composition that may result from alterations of the bedload transport regime and an increase of fine sediments (Bathurst and Iroume, 2014).

The FS WEPP model also showed high sensitivity to changes in climate (Figure 52). Changes in sediment yield mainly reflect changes in precipitation. As more precipitation is delivered to a hillslope, there is more runoff and more sediment carried downslope. Multiple components of the WEPP model are also sensitive to temperature. FS WEPP uses the Priestly-Taylor method to compute daily evapotranspiration, which only requires solar radiation and temperature data to make predictions. Daily potential evapotranspiration is calculated as a function of daily net solar radiation, albedo, slope of the saturated vapor pressure at mean air temperature, and plant biomass (Savabi and Williams, 1995). Evapotranspiration is a direct loss of water to the atmosphere. Water is drawn from the soil layers, reducing the water content in the soil. Plant growth and residue also influence the water balance in a watershed (Savabi and Williams, 1995). A less influential component of the water balance in WEPP is the vegetation interception of rainfall, which is a function of the above ground biomass (Arnold et al., 1995). The plant growth component of WEPP also includes a water stress function that reduces water use efficiency in plant metabolism. The WEPP model predicts that increases in temperature are expected to result in more evapotranspiration and a greater reduction of water content in the soil.

However, the loss of water in soil is not great enough to offset the expected increases in precipitation for some annual return intervals (Figure 52). Predictions of sediment yield increases from biomass removal were exacerbated by climate change for higher frequency annual return intervals (Figure 52). This finding indicates that climate change should be a concern for the NARA project. Sensitivity of sediment yield response to climate is also supported by long-term modeling of basin response to climate change (Coulthard et al., 2008).

The actual response of Cat Spur Creek to the NARA project disturbance of woody biomass removal will be confounded by the presence of sediment retention elements in the channel. Debris jams and vegetation resist flow, decreasing the velocity and transport capacity of the stream and have a large influence on sediment transport predictions (Hallisey and Belt, 1996). If the sediment yield to the stream increases, these obstructions would be expected to dampen the overall stream response (Hassan et al., 2005b). In watersheds without woody debris, streams will most likely be more sensitive to changes in sediment input. This analysis assumes impacts are proportional to the area of disturbance, which is a conservative estimate.

5.4.1. Uncertainty and Disadvantages of FS WEPP

The FS WEPP technical documentation (Elliot et al., 2000) explicitly states that the software has an accuracy of ± 50%. A majority of this error is likely caused by the model structure. The FS WEPP model structure creates a simplification, and perhaps oversimplification, of many physical processes occurring on a hillslope as a tradeoff for less required initialization data.

An additional need of forest hydrology as a whole is an update of the mass movement processes and their relation to current lumber harvesting practices (Gomi et al., 2005). Many studies examining lumber harvesting effects on watersheds were written in the decades following 1950. As the forestry community became more aware of the impact harvesting has on erosion and sediment yields within watersheds, more precautions were created for the tree removal and road construction process. These changes in forestry practices need to be incorporated into existing soil erosion and stream models to accurately predict sediment yields and runoff. Because the vegetation conditions are predetermined and fixed, there is an assumed stationarity of the physical parameters and no physical-biological feedback can be accounted for. The predetermined treatment categories limit the use of FS WEPP to applications where only the relative amounts of erosion, sediment, and runoff yield are required.

5.5. Future Work

To extend the application of this methodology, some components of the analysis may be replaced with more accurate predictors. For examples, the FS WEPP model may be replaced with a more sophisticated hillslope model that has been calibrated for NARA project impacts. Additionally, model calibration would be possible with a sufficiently characterized watershed. The use of remote sensing data (e.g., elevation or vegetation) in combination with field measurements (e.g., bedload transport, suspended sediment, erosion rates, and sediment yield) would provide more accurate initial parameters to initialize the hillslope model. The Nays2DH models were very computationally intensive, limiting the length of time that the models could be ran. Longer term predictions of stream response to sediment yield would be very useful to predict biomass removal impacts. So, if more computational processing ability or a more efficient model were used, a more complete analysis of stream response could be completed. Additionally, a larger scale model of the entire stream network in a watershed could predict some of the downstream impacts throughout the watershed

5.6. Conclusions

Predictions from the FS WEPP indicate that removal of biomass may increase the sediment yield from hillslopes by approximately 35 to 60% compared to traditional logging. The stream response resulting from this increase in sediment yield is predicted to increase in bedload transport between 4 to 5% and may lead to a decrease in mean bed material diameter by up to 4 mm. The assumption that impacts of biomass removal will be as intensive as traditional logging practices will provide a conservative estimate. When implementing this methodology, it will likely be appropriate to multiply predictions by some attenuation factor that will account for forest management practices and forest road construction. A need for more accurate description of biomass removal processes would aid in understanding the extent to which vegetative cover and other FS WEPP parameters would change. Also, ecological assessments would

In this chapter, a methodology capable of predicting both hillslope and stream impacts resulting from woody biomass removal is demonstrated. Two models were used: FS Disturbed WEPP and Nays2DH, which predicted hillslope and stream response to biomass removal, respectively. Both models are free and publicly available. Results of the analysis indicate that there will be an increase in sediment yield (6 to 65%) if vegetative cover and biomass residue are removed from a hillslope. The sediment yield delivered to the stream from the hillslope will result in an increase in bedload transport rate (1 to 6%) and a decrease in mean bed material diameter (up to 4 mm). These predictions are subject to error due to the difficulty in predicting hillslope erosion rates. Hillslope response also showed sensitivity to changes in climate; a simulation using the 2050 climate showed an exacerbation of sediment yield impacts. Ecological consequences of changes to sediment yield, bedload transport, and bed material in the watershed are not known, but could be approximated with an ecological assessment. Monitoring of erosion rates, bedload transport rate, and bed material composition would also be useful to validate the hillslope and stream models. Additional needs for the project are more long-term assessments of stream response and larger scale stream models.

CHAPTER 6: FINAL DISCUSSION AND THESIS SUMMARY

In Chapter 3, statistical analyses and hydraulic simulation of a gravel bedded stream indicated that there are differences in a uniform versus a heterogeneous representation. Statistical analysis of grain size samples indicated that multi-sample, non-parametric tests like the Kruskal-Wallis tests produce most favorable grain size sample groupings. Subsequent hydraulic modeling of surfaces generated from statistical tests showed minimal differences in depth prediction, but up to 39% differences in velocity when the simulations were conducted without bed deformation. This finding shows that roughness heterogeneity alone is sufficient to induce a change in model performance. Using a previously-developed relationship translating grain size to fish size, the differences in velocity predictions were deemed biologically significant.

In Chapter 4, difference in the hydraulic model results of three surface types were explored: uniform, polygon, and smoothed. These surfaces were derived using mean, Thiessen polygon, and kriging calculations, respectively. As a secondary component to the analysis, the difference in hydraulic predictions were compared between Monte Carlo realizations of a kriged roughness surface. Hydraulic models initialized without bed deformation showed a trend of increasing difference in velocity between surfaces with increasing flow rate. The uniform and Thiessen polygon representations performed similarly, indicating that roughness heterogeneity alone was not sufficient to induce a change to sediment transport. Total bedload transport predictions varied by 100% between a heterogeneous and uniform grain size representation. Additionally, the realizations of the kriged surface produced similar sediment transport estimates, indicating that the kriging error estimate was minimal. Bedload transport predictions were shown to be sensitive to grid resolution.

Finally, a combination of hillslope modeling with FS WEPP and sediment transport modeling with Nays2DH was used to approximate the impacts of the NARA project on streams. The increase in sediment yield from additional biomass removal was compared to traditional timber harvest predictions. Results showed that sediment yield predictions had more sensitivity to lower frequency events. NARA project impacts were predicted to increase sediment yield by 6 to 65% compared to traditional harvest practices. The resulting changes in sediment transport from Nays2DH were a 1 to 6% increase in bedload transport and reduction in average bed material grain size of up to 4 mm.

When considering that the bed material at Cat Spur Creek is relatively homogeneous with respect to the full range of natural variability, differences in hydraulic model performance become more significant (Figure 53). Differences in hydraulic model predictions would be expected to increase with increased heterogeneity. Thus, the representation of roughness and grain size distributions become more important as grain size heterogeneity increases.

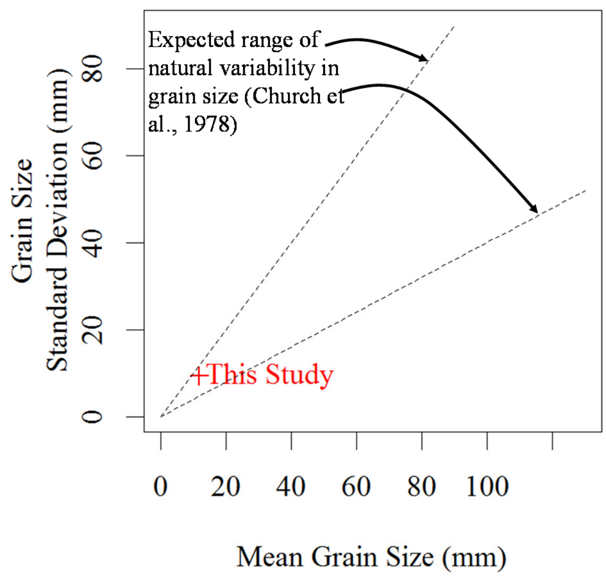

Figure 53. Expected natural variability of grain size mean and standard deviation

Reed Canary grass at the site established banks that are vertical or over-vertical. Vertical banks are not possible in the Nays2DH model. So, the hydraulic models were initialized without modeling bank erosion because it was not necessary nor was the model capable of replicating actual site conditions. However, this setting did produce unreasonably high Shields parameter values in some simulations due to the steepness of the banks. Shear stress is proportional to the slope of the stream, in both transverse and longitudinal directions. In some simulations, banks became nearly vertical, creating a very steep slope. Any amount of flow over this steep portion of the channel then produced a very high shear stress and Shields parameter on the channel banks. Additional complications from vegetation were present when simulating flows greater than bankfull discharge (2.5 m^3/s). At the selected reach along Cat Spur Creek, the floodplain is lined with grass. During flow above bankfull discharge, the vegetation on the floodplain is submerged, causing an increase in resistance to the flow. Work in the field of fluid mechanics has only recently attempted to quantify the effects of vegetation of flow resistance (Nikora, 2010). Thus, predictions of flows greater than bankfull discharge were excluded from analysis.

The influence of biomass removal on the biological environment was not considered in this analysis, but is an essential component of project feasibility. The Cat Spur Creek watershed was recently logged prior to data collection. Vegetation at the site (Reed Canary grass and Red Alders) provided evidence of a disturbed environment. The relationship between vegetation and stream morphology has not fully been explored. Due to the inherent difficulty in simulating fluid flow over vegetation, long-term predictions are assumed to be have a large amount of uncertainty. Vegetation is also likely to change over time in a recovering landscape, influencing soil and stream morphological factors. Biophysical relationships in streams and rivers are not fully understood.

One foreseeable problem with the Nays2DH solver is that the Manning's *n* values are static once set. However, when bedload transport occurs, the D_{84} for a particular location (grid cell) is likely to change over time. Ideally, Manning's *n* would be computed directly from the established grain size distribution, because the two are related by the Manning-Strickler equation. However, this adaptability is not currently established in the Nays2DH solver.

In the context of climate change, the proper representation of natural heterogeneity will become increasingly important. As extreme flow conditions become more common, streams in North America will become more similar to those in New Zealand (Winterbourn et al., 1981), where unpredictable, dynamic climate conditions are typical. Predicting the response that hydraulic and sediment transport parameters will have to these changing conditions will require a more accurate representation of the initial conditions because the natural system will become more dynamic. This will be particularly true in headwater streams, where there is no artificial control of flow by dams.

REFERENCES

(EPA), Environmental Protection Agency. 2004. The Incidence and Severity of Sediment Contamination in Surface Waters of the United States. In *National Sediment Quality Survey*. Washington, D.C.: U.S. EPA.

Arnold, J.G., M.A. Weltz, E.E. Alberts, and D.C. Flanagan. 1995. WEPP Documentation, Ch. 8 Plant Growth Component. United States Department of Agriculture.

Bathurst, J.C., and A. Iroume. 2014. Quantitative generalizations for catchment sediment yield following forest logging. *Water Resources Research* 50 (11):8383-8402.

Bertin, S., and H. Friedrich. 2014. Measurement of Gravel-Bed Topography: Evaluation Study Applying Statistical Roughness Analysis. *Journal of Hydraulic Engineering* 140 (3):269-279.

Bilby, B. 2014. Personal Communication, Weyerhaeuser Meeting 4/3/2014, Vancouver, WA.

Boise Adjudication Team, (BAT). 2014. Sediment Transport in Idaho and Nevada. Forest Service

Bunte, Kristen, and S.R. Abt. 2001a. Sampling Frame for Improving Pebble Count Accuracy in Coarse Gravel-Bed Streams. Journal of the American Water Resources Association.

Bunte, K, and S.R. Abt. 2001b. Sampling Surface and Subsurface Particle-Size Distributions in Wadable Gravel- and Cobble-Bed Streams for Analyses in Sediment Transport, Hydraulics, and Streambed Monitoring. United Stated Department of Agriculture, Forest Service, Rocky Mountain Research Station.

Chappell, A., G. L. Heritage, I.C. Fuller, A. R. G. Large, and D. J. Milan. 2003. Geostatistical analysis of ground-survey elevation data to elucidate spatial and temporal river channel change. *Earth Surface Processes and Landforms* 28 (4):349-370.

Church, M.A., D.G. McLean, and J.F. Wolcott. 1987. *River Bed Gravels: Sampling and Analysis*, *Sediment Transport in Gravel-Bed Rivers*: John Wiley & Sons Ltd.

Clifford, N.J., P.J. Soar, O.P. Harmar, A.M. Gurnell, G.E. Petts, and J.C. Emery. 2005. Assessment of hydrodynamic simulation results for eco-hydraulic and eco-hydrological applications: a spatial semivariance approach. *Hydrological Processes* 19 (18):3631-3648.

Conover, W.J. 1972. A Kolmogorov Goodness-of-Fit Test for Discontinuous Distributions. Taylor and Francis.

Conservancy, Nature. 2009. ClimateWizard.<climatewizard.org>. Access date: 3/15/2015

Corder, G. 2014. *Nonparametric Statistics A Step-by-Step Approach*. Edited by D. I. Foreman. 2nd ed. ed, *Nonparametric Statistics*. Hoboken: Hoboken : Wiley.

Coulthard, T. J., J. Lewin, and M. G. Macklin. 2008. Non-stationarity of basin scale sediment delivery in response to climate change. *Gravel-Bed Rivers Vi: from Process Understanding to River Restoration* 11:315-335.

Crowder, D. W., and P. Diplas. 1997. Sampling heterogeneous deposits in gravel-bed streams. *Journal of Hydraulic Engineering-Asce* 123 (12):1106-1117.

Csillag, F., M. Kertesz, and A. Kummert. 1996. Sampling and mapping of heterogeneous surfaces:

Multi-resolution tiling adjusted to spatial variability. *International Journal of Geographical Information Systems* 10 (7):851-875.

Dunne, T. 2001. Introduction to section 2 - Problems in measuring and modeling the influence of forest management on hydrologic and geomorphic processes. *Land Use and Watersheds: Human Influence on Hydrology and Geomorphology in Urban and Forest Areas* 2:77-83.

Elliot, W.J., D.E. Hall, and D.L. Scheele. 2000. Disturbed WEPP (Draft 02/2000): WEPP Interface for Disturbed Forest and Range Runoff, Erosion and Sediment Delivery. USDA Forest Service.

Elliot, W. J., and E. David. 2010. Disturbed WEPP Model 2.0. Ver. 2014.04.14. In *Online at* <*http://forest.moscowfsl.wsu.edu/fswepp*>. Moscow, ID: U.S. Department of Agriculture, Forest Service, Rocky Mountain Research Station.

Foster, G.R., D.C. Flanagan, M.A. Nearing, L.J. Lane, L.M. Risse, and S.C. Finkner. 1995. Chapter 11. Hillslope Profile and Watershed Model Documentation. In *Water Erosion Prediction Project*. United States Department of Agriculture (USDA).

Fripp, J. B., and P. Diplas. 1993. Surface Sampling in Gravel Streams. *Journal of Hydraulic Engineering* 119 (4):473-490.

Garcia, C., J.B. Laronne, and M. Sala. 1999. Variable source areas of bedload in a gravel-bed stream. *J SEDIMENT RES* 69 (1):27-31.

Gleser, L.J. 1985. Exact Power of Goodness-of-fir Tests of Kolmogorov Type for Discontinuous Distributions. *Journal of the American Statistical Association* 80 (392):954-958.

Gomi, T., R.D. Moore, and M.A. Hassan. 2005. Suspended sediment dynamics in small forest streams of the Pacific Northwest. *Journal of the American Water Resources Association* 41 (4):877-898.

Graham, D. J., I. Reid, and S. P. Rice. 2005. Automated sizing of coarse-grained sediments: Image-processing procedures. *Mathematical Geology* 37 (1):1-28.

Grant, G.E., and A.L. Wolff. 1991. Long-Term Patterns of Sediment Transport after Timber Harvest, Western Cascade Mountains, Oregon, USA. *Sediment and Stream Water Quality in a Changing Environment : Trends and Explanation* 203:31-40.

Guerit, L., L. Barrier, C. Narteau, F. Metivier, Y. Liu, E. Lajeunesse, E. Gayer, P. Meunier, L. Malverti, and B. Ye. 2014. The Grain-size Patchiness of Braided Gravel-Bed Streams – example of the Urumqi River (northeast Tian Shan, China) Advances in Geosciences.

Hallisey, J.E., and G.H. Belt. 1996. Relationships between particle movement and channel morphology in some northern Idaho streams. *Water Resources Bulletin* 32 (2):383-391.

Hassan, M.A., M. Church, T.E. Lisle, F. Brardinoni, L. Benda, and G.E. Grant. 2005a. Sediment transport and channel morphology of small, forested streams. *Journal of the American Water Resources Association* 41 (4):853-876.

Hassan, M.A., D. L. Hogan, S.A. Bird, C.L. May, T. Gomi, and D. Campbell. 2005b. Spatial and temporal dynamics of wood in headwater streams of the Pacific Northwest. *Journal of the American Water Resources Association* 41 (4):899-919.

Heede, B.H. 1991. Response of a Stream in Disequilibrium to Timber Harvest. *Environmental*

Management 15 (2):251-255.

Julien, P.Y. 2010. Erosion and Sedimentation. Cambridge University Press.

Kitanidis, P.K. 1996. On the geostatistical approach to the inverse problem. *Advances in Water Resources* 19 (6):333-342.

Kovacs, A., and G. Parker. 1994. A new vectorial bedload formulation and its application to the time evolution of straight river channels. *Journal of Fluid Mechanics* 267.

Leopold, L.B., M.G. Wolman, and J.P Miller. 1964. Fluvial Processes in Geomorphology. Freeman.

Milhous, R.T. 1973. Sediment transport in a gravel-bottom stream. In *Ph.D. thesis*. Corvallis, OR: Oregon State University

Montgomery, D.R. 2012. Dirt: The Erosion of Civilizations. Berkeley, CA: University of California Press.

Mount, J.F. 1995. *California rivers and streams : the conflict between fluvial process and land use*. Berkeley: Berkeley : University of California Press.

National Climate Data Center, (NCDC). 2015. Climate Data, Clarkia, ID, US.

Nikora, V. 2010. Hydrodynamics of Aquatic Ecosystems: An Interface Between Ecology, Biomechanics and Environmental Fluid Mechanics. *River Research and Applications* 26 (4):367-384.

Parker, G., P.C. Klingeman, and D.G. McLean. 1982. Bedload and Size Distribution in Paved Gravel-Bed Streams. *Journal of the Hydraulics Division-Asce* 108 (4):544-571.

Riebe, C.S., L.S. Sklar, B.T. Overstreet, and J.K. Wooster. 2014. Optimal reproduction in salmon spawning substrates linked to grain size and fish length. *Water Resources Research* 50 (2):898-918.

Robinson, M., and A. Dupeyrat. 2005. Effects of commercial timber harvesting on streamflow regimes in the Plynlimon catchments, mid-Wales. *Hydrological Processes* 19 (6):1213-1226.

Ryan, S.E., and G.E. Grant. 1991. Downstream Effects of Timber Harvesting on Channel Morphology in Elk River Basin, Oregon. *Journal of Environmental Quality* 20 (1):60-72.

Savabi, M.R., and J.R. Williams. 1995. WEPP Documentation, Ch. 5 Water Balance and Percolation. United States Department of Agriculture (USDA).

Shimizu, Y., H. Takebayashi, T. Inoue, M. Hamaki, T. Iwasaki, and N. Mohamed. 2015. Nays2DH Solver Manual, iRIC Software.

Smart, G., J. Aberle, M. Duncan, and J. Walsh. 2004. Measurement and analysis of alluvial bed roughness. *Journal of Hydraulic Research* 42 (3):227-237.

Smith, J. D., and S. R. McLean. 1984. A Model for Flow in Meandering Streams. *Water Resources Research* 20 (9):1301-1315.

Statzner, B., and P. Sagnes. 2009. Hydrodynamic abilities of riverine fish: a functional link between morphology and velocity use. *AQUAT LIVING RESOUR* 22 (1):79-91.

U.S.D.A. Forest Service, (USDA FS). Personal Contact via email: Weston, John and Cameron, Margie. 2014. U.S. Forest Service, Region 1 – RRM Regional FACTS Specialist

Whiting, P.J., and W.E. Dietrich. 1990. Boundary Shear-Stress and Roughness Over Mobile Alluvial Beds. *Journal of Hydraulic Engineering-Asce* 116 (12):1495-1511.

Whitney, S. 1985. *Western forests*. Edited by S. National Audubon. New York: New York : Knopf : Distributed by Random House.

Winterbourn, M.J., J.S. Rounick, and B. Cowie. 1981. Are New Zealand stream ecosystems really different? : New Zealand Journal of Marine and Freshwater Research

Wu, W. 2008. Computational River Dynamics. Taylor and Francis e-Library: Taylor and Francis.

Wu, W., P. Wang, and N. Chiba. 2004. Comparison of Five Depth-Averaged 2-D Turbulence Models for River Flows. Hydro-Engineering and Environmental Mechanics.

Yabe, T., T. Ishikawa, Y. Kadota, and F. Ikeda. 1990. A Multidimensional Cubic-Interpolated Pseudoparticle (CIP) Method Without Time Splitting Technique for Hyperbolic Equations. *Journal of the Physical Society of Japan* 59 (7):2301-2304.

Yen, B.C. 1991. Hydraulics in Open Channels. In *Channel Flow Resistance: Centennial of Manning's n Formula*. Highlands Ranch, CO: Water Resource Publications.

APPENDIX

Appendix A: ROUGHNESS REGION PLOTS FOR STATISTICAL TESTS

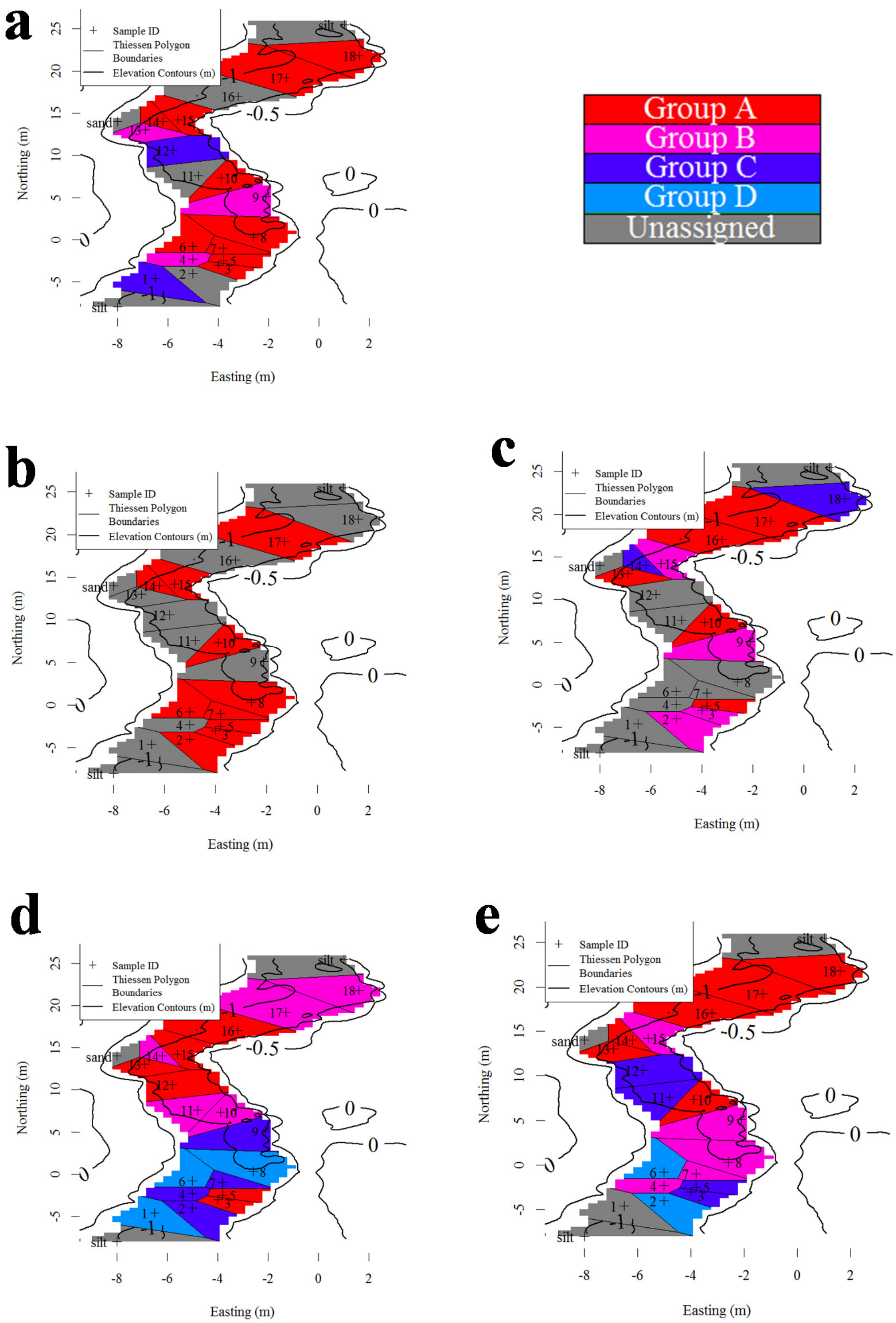

Figure 54. Grain size region plots for (a) Kruskal-Wallis, (b) ANOVA, (c) Kolmogorov-Smirnov, (d) Mann-Whitney, and (e) *t*- statistical tests

Appendix B: GRAIN SIZE DISTRIBUTION PLOTS FOR STATISTICAL TESTS

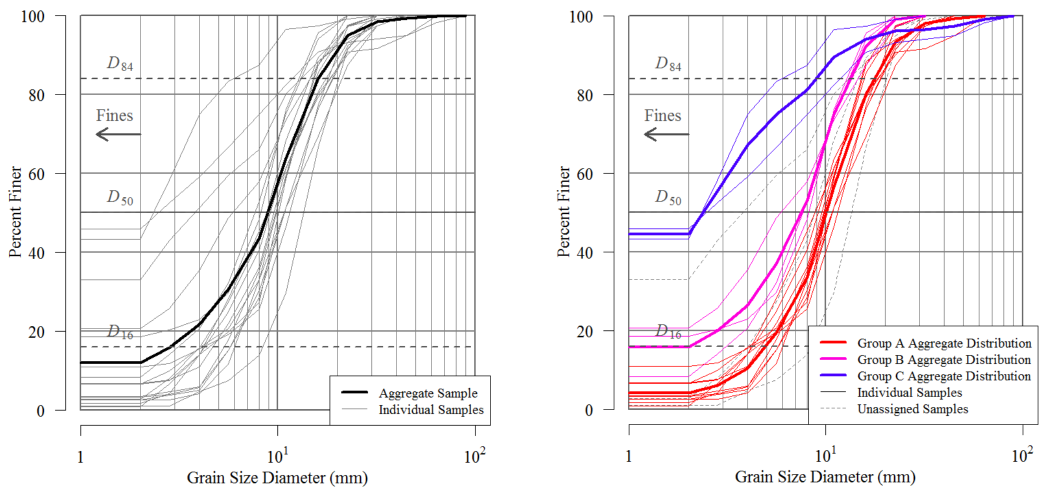

Figure 55. Individual and aggregate grain size distributions (left), and grain size distribution groupings derived from Kruskal-Wallis test (right)

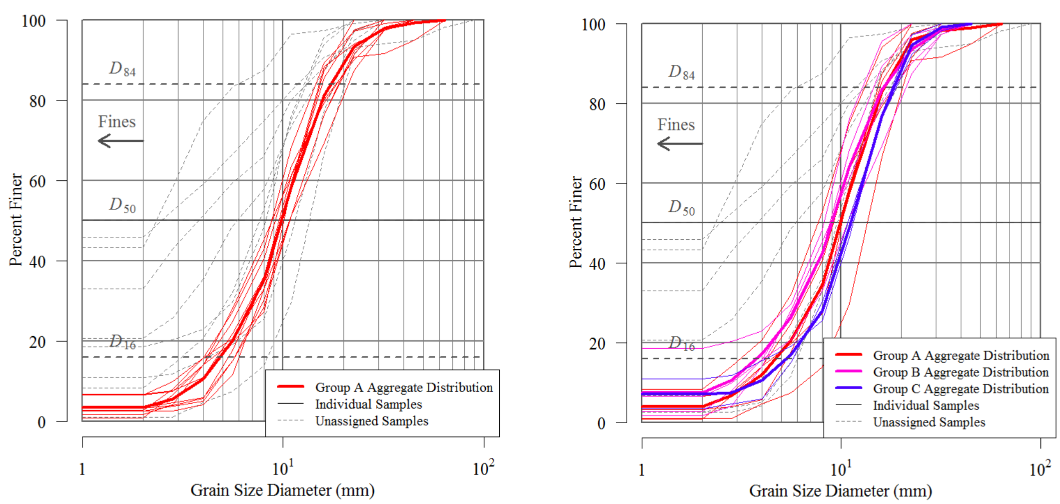

Figure 56. Grain size distribution groupings derived from ANOVA (left), and Kolmogorov-Smirnov (right) tests

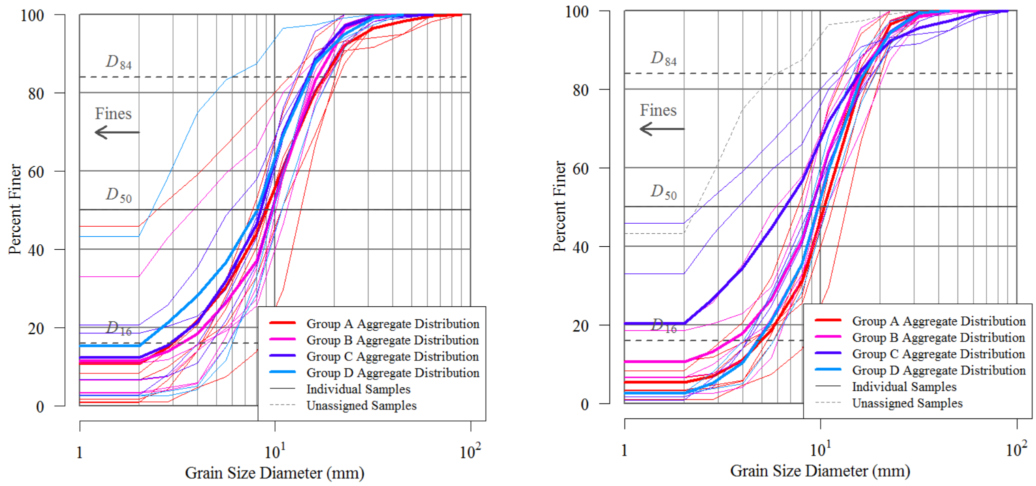

Figure 57. Grain size distribution groupings derived from Mann-Whitney (left) and *t*-test (right)

Appendix C: BEDLOAD TRANSPORT EQUATIONS

Suspended sediment transport is negated in this study, so only bedload transport is considered. There are two options for calculating the bedload transport rate in the Nays2DH software: 1) Meyer-Peter and Müller (Meyer-Peter and Müller, 1948) and 2) Ashida and Michiue formulas (Ashida and Michiue, 1972). Ashida and Michiue formula may be used for mixed size sediment, whereas the Meyer-Peter and Müller formula is only applicable to single sized, or uniform bedload transport.

Meyer-Peter and Müller Bedload Transport Formula

The Meyer-Peter and Müller formula was derived for uniform sediment bedload transport. The grain size data used to validate this formula had means ranging between 3.17 mm and 28.6 mm. The formula was derived from empirical data and was presented in a relatively complex form. Modification of the original formula was later performed to produce a more simplified version (Chien, 1956):

$$\boldsymbol{q_b = 8(\tau_* - \tau_{*c})^{1.5}\sqrt{s_g g d^3}\, r_b} \qquad \text{(C.1)}$$

where,

q_b = unit bedload transport rate (m^2/s)

τ_* = shear stress (N/m^2)

τ_{*c} = critical shear stress (N/m^2)

s_g = specific gravity of bedload particle (unitless)

g = acceleration due to gravity (9.81 m/s^2)

d = particle diameter (m)

r_b = function of the exchange layer thickness (unitless)

The exchange layer function, r_b, was added to the function derived by Chien, 1956 to incorporate a ratio of the sediment layer thickness and bedload layer thickness:

$$\boldsymbol{r_b} = \begin{Bmatrix} \mathbf{1} & \boldsymbol{E_{sd}} > \boldsymbol{E_{be}} \\ \boldsymbol{E_{sd}}/\boldsymbol{E_{be}} & \boldsymbol{E_{sd}} \leq \boldsymbol{E_{be}} \end{Bmatrix} \tag{C.2}$$

where,

E_{sd} = sediment layer thickness on fixed bed (m)

E_{be} = equilibrium bedload layer thickness (m)

Further definition of these terms may be found in the Nays2DH solver manual (Shimizu et al., 2015).

Ashida and Michiue Bedload Transport Formula

The Ashida and Michiue formula was developed to analyze mixed size sediment, but may also be easily modified for uniform sediment transport analysis:

$$\boldsymbol{q_{bk} = 17 p_{mk} \tau_{*ek}^{1.5} \left(1 - K_c \frac{\tau_{*ck}}{\tau_{*k}}\right)\left(1 - \sqrt{K_c \frac{\tau_{*ck}}{\tau_{*k}}}\right)\sqrt{s_g g d_k^3}\, r_b} \tag{C.3}$$

where,

p_{mk} = fraction of sediment size class in bedload layer (unitless)

τ_{*ek} = effective shields number in layer *k* (unitless)

K_c = is the modification function for bed slope effect on sediment transport (unitless)

τ_{*ck} = critical Shields number for grain of the size in layer *k* (unitless)

τ_{*k} = Shields number on grain of the size in layer *k* (unitless)

The total bedload may be calculated by summing the q_{bk} values for all k. A corresponding form of this equation was also formulated in Kovacs and Parker, 1994. Some limitations to the Ashida and Michiue formula have been identified. The approach is shown to be very sensitive to the transverse (cross-channel) slope of the stream. Additionally, in the derivation of the equation, an assumption was made that the dynamic Coulomb friction factor, μ_c, is equivalent to the static Coulomb friction factor, μ_s. This assumption is similar to equating the static and dynamic/kinematic friction coefficient in a common dynamics problem. Ideally, μ_c would approach μ_s as shear stress decreased (Kovacs and Parker, 1994). Despite these limitations, equations of this form have been shown to simulate actual channel erosion rates reasonably well (Kovacs and Parker, 1994).

Appendix D: SEMI-VARIOGRAM MODEL SELECTION

The data was first checked for anisotropy prior to development of a semi-variance model. Linear trends were examined in a polar data set of difference in D_{84} and angle. An angle of zero degrees was assigned to the easting at the site, which was an arbitrary datum approximately pointed cross-stream towards the right bank (Figure 58). Angles are counter-clockwise from the easting. Because the stream was relatively straight, most of the angles correspond to points downstream or upstream of each other. Thus, cross-stream anisotropy was not well represented due to the location of measurement points. In Figure 58, the p-value is the probability that the slope of the polar data set is not zero for that angle. The linear trend analysis indicates that there is mild anisotropy, but its significance is at best 0.02 in the approximate downstream direction, and this statistical significance (p-value < 0.05) is not consistent for all downstream angles. Additionally, there was no onsite indication of a fining or coarsening grain size in the downstream direction and bias is introduced into the data set because there was a lack of data in the cross-stream direction. Thus, anisotropy is neglected in the subsequent analysis.

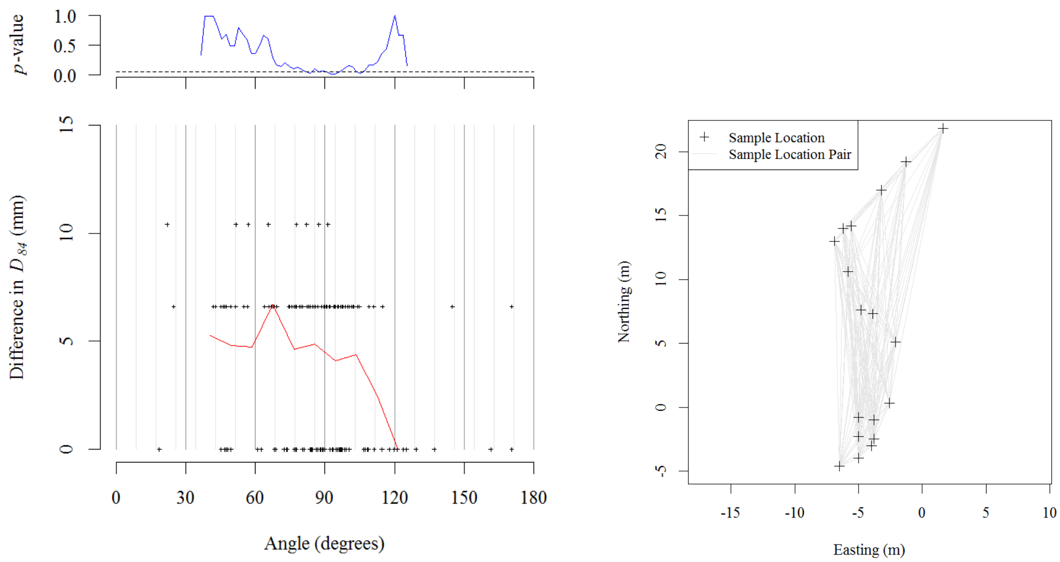

Figure 58. Linear trend analysis of polar data (left) and areal display of point pairings (right)

After the anisotropy analysis, semi-variogram models were fit to the data, and the goodness of each model's fit was determined. Models initially explored and results of their fitting parameters are shown below (Table 23). The following diagnostic measurements were used to select between semi-variogram models:

- Leave-one-out cross-validation (LOOCV): the semi-variogram model is fit to the data set with one point removed. The ability of the semi-variogram model to estimate the known point is evaluated by examining the mean and standard deviation of the estimates.
- Sum of squared error: sum of squared differences between semi-variogram model and semi-variogram cloud.

- <u>Loglikelihood:</u> sum of natural logarithm of absolute difference between semi-variogram model and empirical semi-variogram.
- <u>Akaike's Information Criterion (AIC):</u> value that accounts for the number of parameters and the loglikelihood: AIC = 2(<*number of parameters*>) – 2(<*loglikelihood*>)

The exponential, exponential class, matern, matern M. Stein's parameterization, and spline semi-variograms were selected for further examination (Figure 59). The exponential semi-variogram is not visible in Figure 59 because it is overlain by the exponential class semi-variogram. The spherical semi-variogram is identical to the matern semi-variogram. The exponential model was selected because it performed well in all of the diagnostic criterion and was contained by the empirical semi-variogram (Figure 59). The exponential class model would have performed identically to the exponential model. A description of the subsequent kriging of streambed surfaces and Monte Carlo realization of the kriged surfaces may be found in sections 2.3 and 2.4 of the literature review.

Table 23. Semi-variogram models and results of fitting

Model Name	Nugget	Partial Sill	Range	LOOCV, Mean	LOOCV, Standard Deviation	Sum of Squared Error	Loglikelihood	AIC
Exp (exponential)	1.32	369.46	32.68	1.00	1.32	152011	53.40	-64.80
Sph (spherical)	2.85	213.04	32.61	0.97	1.28	138252	44.84	-47.67
Gau (gaussian)	23.92	406.08	26.89	1.07	1.41	311557	56.13	-70.25
Exclass (Exponential class)	0.00	133.67	34.69	0.96	1.64	21411	48.03	-54.06
Mat (Matern)	1.32	367.68	32.51	1.00	1.32	151376	52.94	-63.88
Mat (Matern, M. Stein's parameterization)	1.11	276.99	33.73	1.00	1.32	114958	49.92	-57.84
Cir (circular)	3.05	224.87	30.17	0.97	1.28	154188	47.54	-53.09
Lin (linear)	3.34	255.66	28.94	0.97	1.30	191130	47.80	-53.60
Bes (bessel)	9.69	406.08	12.97	0.93	1.20	432976	56.56	-71.12
Pen (pentaspherical)	2.48	188.25	34.69	0.97	1.28	109181	43.54	-45.09
Per (periodic)	37.29	10.41	7.94	1.37	2.48	29036	51.25	-60.50
Wav (wave)	23.16	406.08	31.06	1.07	1.40	627521	52.82	-63.64
Hol (hole)	23.16	406.08	9.89	1.07	1.40	627805	56.47	-70.94
Log (logarithmic)	0.00	22.07	0.73	1.29	1.87	21788	76.50	-111.01
Pow (power)	0.00	16.49	0.48	1.12	1.85	459	76.50	-111.01
Spl (spline)	0.84	49.60	0.01	1.22	2.27	30605	46.96	-51.93
Leg (Legendre)	0.28	16.40	34.69	1.22	2.27	30605	68.83	-95.66

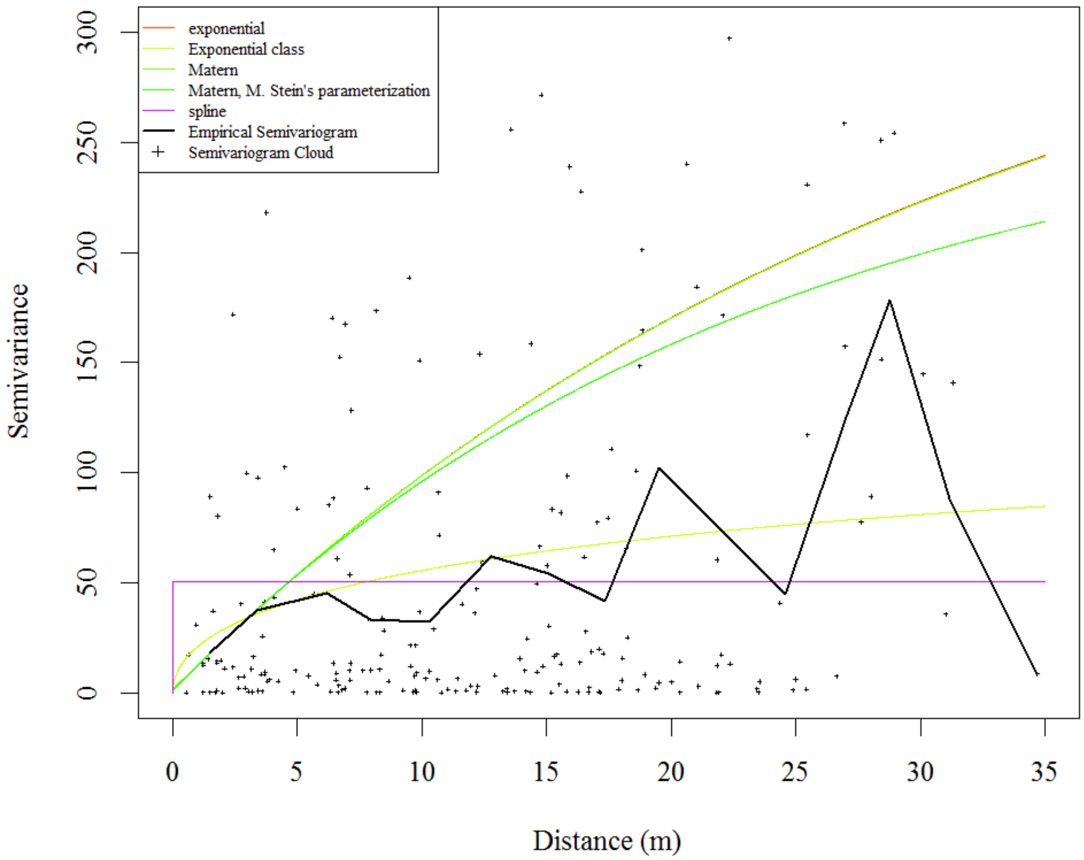

Figure 59. Selected semi-variogram models. Lines for exponential and exponential class models overlap

Appendix E: PHOTOGRAPHS OF SITE SURVEYING

Figure 60. Clearcut hillslope along left (facing downstream) valley hillslope. Photo taken at selected reach. Trees in foreground establish a buffer strip around stream.

Figure 61. Typical composition of gravel deposit. Quarter is 25.4 mm shown for scale

Figure 62. Field deployment of sampling frame

Figure 63. Bathymetric survey of site with total station

Figure 64. Undercutting of banks. Banks are held in place by vegetation and

Figure 65. Debris jam at upstream end of selected reach

Figure 66. In-stream island shaded by red alders along left bank

Appendix F: R PROGRAMMING CODES

This code was written using RStudio Graphical User Interface (GUI). Certain functionally of the code is specific to RStudio. For example, there are sections used in the code formatted by comments (e.g., “### Section 1 #######################”, “### ___a) Section 1.a ############”).

F.1. Thiessen Polygon Surface Generation

```
### Theissen Polygons #########
require("rgdal")
setwd("D:/NARA_D/Reports/GSD Project/Data")

#Taken from:
#http://stackoverflow.com/questions/9403660/how-to-create-thiessen-polygons-from-points-using-r-packages
# Carson's Voronoi polygons function
voronoipolygons <- function(x) {
  require(deldir)
  require(sp)
  if (.hasSlot(x, 'coords')) {
    crds <- x@coords
  } else crds <- x
  z <- deldir(crds[,1], crds[,2])
  w <- tile.list(z)
  polys <- vector(mode='list', length=length(w))
  for (i in seq(along=polys)) {
    pcrds <- cbind(w[[i]]$x, w[[i]]$y)
    pcrds <- rbind(pcrds, pcrds[1,])
    polys[[i]] <- Polygons(list(Polygon(pcrds)), ID=as.character(i))
  }
  SP <- SpatialPolygons(polys)
  voronoi <- SpatialPolygonsDataFrame(SP, data=data.frame(x=crds[,1],
                                       y=crds[,2], row.names=sapply(slot(SP, 'polygons'),
                                                      function(x) slot(x, 'ID'))))
}

## Function Test 1 #########
#As seen on website

dsn <- system.file("vectors", package = "rgdal")[1]
cities <- readOGR(dsn=dsn, layer="cities")

v <- voronoipolygons(cities)

par(mar=c(1,1,1,1))
plot(v)

## Function Test 2 #########
coords <- data.frame(x=rnorm(100,5,2), y=rnorm(100,15,5) )



b <- voronoipolygons(coords)

plot(b)
points(b$x, b$y, pch=3, cex=0.4)
str(b)
```

```
plot(b$x, b$y)

#Extracting list of polygons
b.polys <- b@polygons

b.polys1 <- b.polys[[1]]@Polygons
str(b.polys1)
class(b.polys1)

coords.b1 <- b.polys[[1]]@Polygons[[1]]@coords

plot(coords.b1)
lines(coords.b1)


### Thiessen Polygonization of CSC ##################
#Reading in coordinates #######
setwd("D:/NARA_D/Reports/GSD Project/Data")
require(gdata)
csc.raw.coords <- read.xls("Bed_Material_Raw_Master_Data.xlsx",
                       sheet = "Sample Locations - Frame Coords")
bed.diam <- read.xls("Particle_Diameters.xls")
bed.sum  <- read.xls("Particle_Diameters.xls")

#Rearranging coordinates to new frame labels
csc.raw.coords <- csc.raw.coords[order(csc.raw.coords$New.Frame.Label),]

#Extracting only easting and northing of coordinate data
csc.coords <- data.frame(east=csc.raw.coords$Easting_m,
                     north=csc.raw.coords$Northing._m)

#Adding additional points for clay material at reach boundary
csc.coords[19,] <- c(-8,-8)
csc.coords[20,] <- c(1, 25.5)
#Sand bank sample
csc.coords[21,] <- c(-8, 14)

#Performing test
csc.thiess <- voronoipolygons(csc.coords)

###__Plotting ###################
plot(csc.thiess)
points(csc.thiess$x, csc.thiess$y, pch=3, cex=0.5)

#Extracting polygons
csc.polys <- csc.thiess@polygons

#First, finding the maximum number of points in polygon
max.pts <- 0
for(i in 1:nrow(csc.coords)){
  if(nrow(csc.polys[[i]]@Polygons[[1]]@coords) > max.pts){
  max.pts <- nrow(csc.polys[[i]]@Polygons[[1]]@coords)}
}

#Creating data frames for x and y coordinates
x <- matrix(NA, nrow=max.pts, ncol=nrow(csc.coords))
y<-x

#Extracting Coordinates
for(i in 1:nrow(csc.coords)){
  n.pts <- nrow(csc.polys[[i]]@Polygons[[1]]@coords)
  x[1:n.pts,i] <- csc.polys[[i]]@Polygons[[1]]@coords[,1]
  y[1:n.pts,i] <- csc.polys[[i]]@Polygons[[1]]@coords[,2]

}
```

F.2. Kriging-Monte Carlo Surface Generation

This code assumes that x, y, and z values are already loaded (see section below for loading of x, y, and z values
See "***SemiVariogram Model Development***" portion of cross-validation code

```
#Loading data from cross-validation
setwd(results.directory)

summary.variog <- read.xls("Summary_Variogram_Cross_Validation.xls")
summary.variog

selected.model <- 9
#Using the exponent model (row = 9)
fit.vgm <- vgm(psill = summary.variog$psill[selected.model],
          model = as.character(summary.variog$model.short[selected.model]),
          range = summary.variog$range[selected.model],
          nugget = summary.variog$nugget[selected.model]
  )

fit.exp <-   fit.variogram(object = variog.d84,
                 fit.ranges = F,
                 fit.sills = F,
                 model = fit.vgm)

#Setting grid resolution and kriging points
grid.res <- 0.25
east.pts <- seq(-13,6, by=grid.res)
north.pts <- seq(-8,27, by=grid.res)

#establishing a grid of points to krig
krige.xy <- data.frame(x = rep(east.pts, times = length(north.pts)),
               y = rep(north.pts, each = length(east.pts)),
               z=NA)
coordinates(krige.xy) <- ~x+y

krige.gstat <- krige(z~x+y, data.raw,
         newdata = krige.xy,
         model=fit.exp)
###___Sampling from Distribution ######################
#surf.samp* is a realization of the random surface

#Extracting easting and northing coorinates
map.x <- east.pts #(should be same as map.x and east.pts)
map.y <- north.pts

#Extracting mean and standard deviation estimates
map.mean <- matrix(krige.gstat$var1.pred,
          nrow=length(east.pts),
          ncol=length(north.pts))
krige.gstat$var1.var[is.na(sqrt(krige.gstat$var1.var))] <-
  sqrt(mean(krige.gstat$var1.var, na.rm=T))
map.se   <- matrix(sqrt(krige.gstat$var1.var),
          nrow=length(east.pts),
          ncol=length(north.pts))

#### SETTING NUMBER OF REALIZATION ############
#Creating sample surfaces and tracking with an array
n.realizations <- 15

surf.samp <- array(data = NA, dim = c(length(map.x),   #rows
                    length(map.y),   #columns
                    n.realizations)) #matrix

#Sampling from the mean and standard deviation surfaces
for(k in 1:n.realizations){
```

```
 for(i in 1:length(map.x)){  #row
   for(j in 1:length(map.y)){ #column
     #print(paste(i,j,k))
     surf.samp[i,j,k] <- rnorm(n = 1,mean = map.mean[i,j],
                       sd = map.se[i,j])

   }
 }
}
```

F.3. Leave-one-out Cross-Validation of Semivariogram Models

```
####### Cross-validation of Semivariogram models ###################
#This code will take parameter data, incuding horizontal location (x,y) and
#  parameter value (z), and find the best fitting ORDINARY, ISOTROPIC
#  semivariogram model.  The code is written generically, so future data
#  sets may be validated without need to extensively adapt the code
#  for the purposes of ORDINARY, ISOTROPIC kriging.
#_______________________________________________________________________
#TO ADAPT THE CODE, simply change section 1 (Creating x,y,z, Dataset)
#  so that the x,y, and z values are assinged the desired data set values

#### FURTHER WORK ###############################################
#The semivariogram models that do not apply (e.g., nugget model,
#  and measurement error) should be excluded from the list
#  in semiv.models before further analysis is done, as they tend to
#  confound results.

### Overview: Semivariogram Model Development ###################
#Development of the semivariogram models is as follows.
#Format is [package::function]

#   1) Create dataset with x, y, and z values of parameter
#   2) Create empirical semivariogram of data set
#   3) Fit parameters to the semivariogram model

### Overview: Cross-Validation Procedure ###########
#This code will cross-validate semivariogram models
#  to determine the best fitting one of a multiple models.
#The cross-validation procedure is as follows (Minasny et al., 1987):
#   1)  Generate the semivarigram model using the observed data
#     points, but exclude one point from analysis.
#   2)  Using the selected semivariogram model, create a kriged estimate
#     of the parameter at the location of the excluded point.
#   3)  Find the squared difference of the kriged point estimate
#     and the observed value and divide by the kriged variance estimate.
#   4)  Repeat this procedure for each point location, and for each
#     semivariogram model.
#   5)  Choose the model that produces the mean of difference data to
#     be closest to zero and the standard deviation closest to one.

###__Additional Things of Interest #######################
#The following calculations can be performed with the
#  krige function, and should be kept in mind (example from ?krige):

# # the following has NOTHING to do with kriging, but --
# # return the median of the nearest 11 observations:
# x = krige(zinc~1, meuse, meuse.grid, set = list(method = "med"), nmax = 11)
# # get 25%- and 75%-percentiles of nearest 11 obs, as prediction and variance:
# x = krige(zinc~1, meuse, meuse.grid, nmax = 11,
#          set = list(method = "med", quantile = 0.25))
# # get diversity (# of different values) and mode from 11 nearest observations:
# x = krige(zinc~1, meuse, meuse.grid, nmax = 11, set = list(method = "div"))


###Loading necessary R packages ###################
```

```
#kriging and plotting packages
require(fields); require(gstat); require(geoR)
#packages for reading & writing .xls files
require(gdata); require(WriteXLS)

### Defining Directories ###############
#These are the directories where data is loaded from
#  or saved to (uncomment/comment as necessary)
###___DELL #############
bed.material.data.directory <-
  "C:/Users/cee-user/Dropbox/NARA Project/Data - Bed Material Measurements/"
results.directory <-
  "C:/Users/cee-user/Dropbox/NARA Project/Analysis - Kriging Roughness Surface"
plot.save.directory <-
  "C:/Users/cee-user/Dropbox/NARA Project/Analysis - Kriging Roughness Surface"


### Semivariogram Model Development ##############################

### ___1) Creating x,y,z Dataset #######################
setwd(bed.material.data.directory)

#Function to calculate representative grain size (d_x) for
#  a given GSD distribution data set (sample.ds)
d_x.fun <- function(d_x, sample.ds){
  #d_x is the fraction finer than value (not percent)
  #sample.ds is a vector of grain size diameters
  #  (can contain NA)

  sample.trim <- sample.ds[!is.na(sample.ds)] #removing NA
  n.meas <- length(sample.trim)  # number of measurements

  return(sample.trim[as.integer(n.meas*d_x)])
}


#particle diameter data for each sample frame
diam <- read.xls("Particle_Diameters.xls")
#locations corresponding to each sample
diam.pts <- read.xls("Bed_Material_Raw_Master_Data.xlsx",
                sheet="Sample Locations - Frame Coords")
#Refining diam.pts to only easting and northing
diam.pts <- diam.pts[,3:4]
diam.pts$Northing._m <- as.numeric(as.character(diam.pts$Northing._m))


###______a) Creating d84 values ######################

#Applying the d_x.fun function to the particle diameter data
#  and generating a summary variable 'd84'
d84 <- apply(X = diam[,2:19], MARGIN = 2, FUN = d_x.fun, d_x = 0.84)


###______b) Adding sand and clay points ########
#Adding additional points for clay material at reach boundary
diam.pts[19,] <- c(-8,-8)
diam.pts[20,] <- c(1, 25.5)

#Sand bank sample
diam.pts[21,] <- c(-8, 14)

#Adding the diameters of sand and clay measurements to the d84 variable
d84[19:21] <- c(0.1, 0.1, 1)

###______c) Alternative d84 values (distribution-derived) ############
#Loading lognormal distribution fit parameters (mean and sd)
```

```
#  from distribution test results
log.dist.fit <- read.xls("Results - Discrete Tests for Lognormal Distribution.xls")

#Demo of what log.dist.fit is:
#Empirical cdf of second frame GSD
# plot(ecdf(diam$Frame.2))
# #Lognormal distribution fit to GSD (optimal fit)
# lines(seq(0,50,by=0.1),
#       plnorm(q = seq(0,50,by=0.1), meanlog = log.dist.fit$mean.log.opt[2],
#            sdlog = log.dist.fit$sd.log.opt[2]))

#Cycling through each distribution and calculating the
#  d84, as derived from the lognormal distribution parameters
d84.mod <- d84
for(i in 1:18){
  #Finding quantile at which 84% of data is lower
  d84.mod[i] <- qlnorm(p = 0.84,lower.tail = T,
                  meanlog = log.dist.fit$mean.log.opt[i],
                  sdlog = log.dist.fit$sd.log.opt[i])
}



###______d) Defining x,y,z ########################################
x <- diam.pts$Easting_m
y <- diam.pts$Northing._m
z <- d84
z.mod <- d84.mod

###___2) Empirical Semivariogram ###################################
#Creating geodata from point measurements and d84 of each measurement

data.raw <- data.frame(x,y,z)
coordinates(data.raw) <- ~x+y


#gstat
variog.d84 <- variogram(z~x+y, data=data.raw, cutoff=35)
variog.d84.cloud <- variogram(z~x+y, data=data.raw, cloud = T, cutoff=35)

###Initial Plots for coding
#gstat empirical variogram
plot(variog.d84$dist, variog.d84$gamma, col="blue", type="l")
#semivariogram cloud
points(variog.d84.cloud$dist, variog.d84.cloud$gamma, cex=0.1, pch=3)



###___3) Fit parameters to the semivariogram models #################

###______a) Semivariogram model selection ###########################
# Available choices for model are:
vgm()
#Excluded models [element id in vgm()]:
#  nugget[1]; periodic [12]; wave[13]; spline [17];
# legendre [18]; measurement error [19];  intercept[20]
semiv.models <- vgm()[-c(1, 12, 13, 17, 18, 19, 20),]
rownames(semiv.models) <- 1:length(semiv.models[,1])
semiv.models

#Creating a list to contain the semivariogram
#  model fits derived using the gstat package
variog.list <- list()

#Also findig Sum of square error and loglikelihood for each model fit
SSErr <- vector(mode = "numeric", length=length(semiv.models$short))
```

```
Log.like <- SSErr
# #Root mean square error: sqrt(squared error at point estimate)
# RMSE  <- vector(mode = "numeric", length=length(semiv.models$short))
# #Mean square deviation ratio: RMSE/variance of point estimate
# MSDR  <- vector(mode = "numeric", length=length(semiv.models$short))

#Initial nugget estimate is 0.01
nugget.est <- 0.01

for(i in 1:length(semiv.models$short)){ #For all semivariogram models

 #Print out of loop status
 writeLines(paste(i," of ", length(semiv.models$short), " models"))
 writeLines(paste("Fitting ", semiv.models$long[i], " model\n"))

 #Some models have limitations on their ranges, so these
 #  if statements address that and fit a variogram using appropriate ranges
 if(semiv.models$short[i] == "Nug" | semiv.models$short[i] == "Err" |
     semiv.models$short[i] == "Int"){

  #Nugget, Measurement Error, and Intercept models require a range of 0
  range.est <- 0

  variog.fit <- fit.variogram(object = variog.d84,
                     fit.sills = T,
                     model = vgm(psill = var(d84),
                             model = semiv.models$short[i],
                             range = range.est,
                             nugget = nugget.est))

 }else if(semiv.models$short[i] == "Pow"){
 #Power models cannot handle large ranges,
 #  so the range is reduced here, then optimized
  range.est <- 0.01

  semiv.models[i,]

  variog.fit <- fit.variogram(object = variog.d84,
                    fit.ranges = T,
                    fit.sills = T,
                    fit.method=7,
                    model = vgm(psill = var(d84),
                            model = semiv.models$short[i],
                            range = range.est,
                            nugget = nugget.est))

 }else{

  if(semiv.models$short[i] == "Spl"){ #Spline model cannot handle large range
   range.est <- 0.01
  }else if(semiv.models$short[i] == "Gau"){
   nugget.est <- 1  #Gaussian models are picky about their initial nugget estimate (apparently)
   range.est <- max(diff(data.raw@coords))
  }else{  #Using range of data for range of model
   range.est <- max(diff(data.raw@coords))
  }
  fit.range.var <- T

  #Defining an initial variogram model (best guess)
  vgm.model <- vgm(psill  = var(d84),
              model  = semiv.models$short[i],
              range  = range.est,
              nugget = nugget.est)


  #Deriving optimal parameters for semivarigram
```

```
    variog.fit.gls <- fit.variogram.gls(formula = z~x+y, #data formua
                                 data = data.raw, #data
                                 ignoreInitial=F, #Logic for whether or not to
                                 # ignore initial estimates
                                 maxiter = 50,    #Maximum iterations
                                 model = vgm.model)

    #Using fitted parameters to define semivariogram
    variog.fit <- fit.variogram(object = variog.d84,
                          fit.ranges = F,
                          fit.sills = F,
                          model = vgm(psill = variog.fit.gls$psill[2],
                                model = semiv.models$short[i],
                                range = variog.fit.gls$range[2],
                                nugget = variog.fit.gls$psill[1]))

  }

  writeLines("")  #Adding a space to the print out

  ###___a) Error Calculations
#      #Creating a krige estimate at observed points
#      krige.est <- krige(formula=z~x+y, locations=data.raw,
#                   newdata=data.raw, model=variog.fit)
#
#      #Calculating root mean square error:
#      RMSE[i] <- sqrt(sum((krige.est$var1.pred - z)^2))
#
#      #Calculating mean square deviation ratio:
#      MSDR[i] <- sum((krige.est$var1.pred - z)^2/krige.est$var1.var)
#
     #Calculating Sum of square error:
     SSErr[i] <- attr(variog.fit, "SSErr")

  #Calculating likelihood
  Log.like[i] <- 0
  for(k in 1:length(variog.d84$dist)){
    Log.like[i] <- Log.like[i] +
     log(abs(variog.d84$gamma[k] -
       variogramLine(object = vgm.model,
              maxdist = variog.d84$dist[k], n=2)[2,2]) )
  }


  #Adding fitted variogram to a list
  variog.list[[i]] <- list(variog.fit)

}   #End i loop:  for all semivariogram models


#Interpretation of warnings:
#1)  Maximum algorith iterations reached:
# In fit.variogram.gls(formula = z ~ x + y, data = data.raw, ignoreInitial = F,  :
#                  range parameter at search space boundary
#   - Fixed by increasing the maxiter value in the fit.variogram.gls function

#2)  Ideal parameter fit for range parameter is outside of observed distance range
# In fit.variogram.gls(formula = z ~ x + y, data = data.raw, ignoreInitial = F,  :
#                  range parameter at search space boundary
#   - the optimal range of the fitted semivariogram is outside of the
#     maximum observed range in the data


### Cross-Validation of Semivariogram Models #####################
#Creating a complementary list ot the list of variogram models
#  to track model performance
```

```
#Example from ?krige.cv:
# library(sp)
# data(meuse)
# coordinates(meuse) <- ~x+y
# m <- vgm(.59, "Sph", 874, .04)
# # five-fold cross validation:
# x <- krige.cv(log(zinc)~1, meuse, m, nmax = 40, nfold=5)
# bubble(x, "residual", main = "log(zinc): 5-fold CV residuals") #displays residuals results

###___Cross-validation Implementation ###############################
#This code extracts the previously fitted model parameter information from the
#  list variog.list, then uses it to perform the LOOCV using the
#  function krige.cv.  Performance of each model (i.e., the point estimate,
#  and error variance, and additional data about the point prediction)

variog.perform <- list()

for(i in 1:length(variog.list)){

  #Extracting required information from list
  model.pars <- as.data.frame(variog.list[[i]])

  #Assigning extracted parameters to individual, singular
  #  vectors so they can be input to the vgm function
  psill.vgm <- model.pars$psill[2]
  model.vgm <- as.character(model.pars$model)[2]
  range.vgm <- model.pars$range[2]
  nugget.vgm <- model.pars$psill[1]
  kappa.vgm <- model.pars$kappa[2]

  vgm.model <- vgm(psill = psill.vgm,
                model = model.vgm,
                range = range.vgm,
                nugget = nugget.vgm,
                kappa = kappa.vgm)

  #k-fold Cross-validation of semivariogram
  print(model.vgm)
  variog.perform[[i]] <-
    list(krige.cv(z~x+y, data.raw,
               model = vgm.model,
               nmax = 20, nmin=5,
               nfold=nrow(data.raw) #k-fold for leave-one-out cross-validation
               ))
}


###___Compiling Results ##########################################
#The data from the cross-validation is contained in variog.perform,
#  which is a list containing a dataframes for each result.  To compile
#  the results, functions are applied to the data frames.

#Summary dataframe to be saved to file once computed
summary.variog <- data.frame(
  model = semiv.models,
  nugget = NA, psill = NA,   range = NA,   #range
  LOOCV.mean = NA,  #Leave-one-out cross-validation
  LOOCV.sd = NA, #(already calculated these in section 3)
#                         RMSE = RMSE,    #root mean square error
#                         MSDR = MSDR,    #mean square deviation ratio
  SSErr = SSErr,   #sum of squared error
  Log.like = Log.like, #loglikelihood
  AIC = NA,      #Akaike's Information Criterion
  AIC.prob = NA, #AIC probability
```

```
  BIC =NA,       #Bayesian Information Criterion
  BIC.prob = NA,

  #Rank of each model wrt diagnostic criterion
  LOOCV.mean.rank = NA, LOOCV.sd.rank = NA, #leave-one-out cross-validation parameters
  SSErr.rank = NA, #sum of square error
  Log.like.rank=NA, #loglikelihood
  AIC.rank=NA, BIC.rank=NA, #Akaike's and Bayesian Criterion
  sum.criterion=NA  #sum of evaluation criterion
)

for(i in 1:nrow(summary.variog)){  #For all variogram models

  try.result <- try(as.data.frame(variog.perform[[i]]))

  #First, need to check that index value i
  #  (i.e., model i) was actually calculated
  if(class(try.result) != "try-error" & !is.null(variog.perform[[i]])){

    #Extracting data frame derived from krige.cv,
    #  contained in variog.perform
    cv.data <- as.data.frame(variog.perform[[i]])

    #Extracting required information from list
    model.pars <- as.data.frame(variog.list[[i]])

    summary.variog$nugget[i] <- model.pars$psill[1]
    summary.variog$psill[i]  <- model.pars$psill[2]
    summary.variog$range[i]  <- model.pars$range[2]

    summary.variog$LOOCV.mean[i] <- mean(cv.data$residual^2/abs(cv.data$var1.var))
    summary.variog$LOOCV.sd[i]   <- sd(cv.data$residual^2/abs(cv.data$var1.var))


    #AIC is -2*log-likelihood + k * npar
    #   npar  = number of parameters
    #   k     = 2
    k.aic <- 2
    #For BIC, eqn is same, but
    #   k     = ln(n)
    #   n     = number of observation
    k.bic <- log(length(data.raw))

    summary.variog$AIC[i] <- -2*summary.variog$Log.like[i] + k.aic*length(data.raw)
    summary.variog$BIC[i] <- -2*summary.variog$Log.like[i] + k.bic*length(data.raw)

    summary.variog$LOOCV.mean.rank <- rank(summary.variog$LOOCV.mean)
    summary.variog$LOOCV.sd.rank <- rank(summary.variog$LOOCV.sd)
    summary.variog$SSErr.rank <- rank(summary.variog$SSErr)
    summary.variog$Log.like.rank <- rank(summary.variog$Log.like)
    summary.variog$AIC.rank <-  rank(summary.variog$AIC)
    summary.variog$BIC.rank <-  rank(summary.variog$BIC)

    summary.variog$sum.criterion <- apply(summary.variog[,14:17],
                                   MARGIN = 1,FUN = sum, na.rm=T)

  }

}

#Computing relative probabilities:
# AIC.prob = exp((min(AIC) - AIC_i)/2)  #(same for BIC.prob)
#"can be interpreted as the relative probability
# that the ith model minimizes the (estimated) information loss"
summary.variog$AIC.prob <- exp((min(summary.variog$AIC, na.rm=T) - summary.variog$AIC)/2)
summary.variog$BIC.prob <- exp((min(summary.variog$BIC, na.rm=T) - summary.variog$BIC)/2)
```

```
#Results of leave-one-out cross-validation of semivariogram models:
summary.variog <- summary.variog[order(summary.variog$sum.criterion),]
row.names(summary.variog) <- 1:nrow(summary.variog)
summary.variog


###___Saving Results ############################################
setwd(dir = results.directory)

WriteXLS(x = "summary.variog",
      ExcelFileName = "Summary_Variogram_Cross_Validation.xls")
```